

# PHILIPS TECHNICAL REVIEW

WDM in optical-fibre communication I

Beam manipulation in laser welding

Submicron technology centre

Dual-energy X-ray diagnostics



**PHILIPS**

Philips Technical Review (ISSN 0031-7926) is published by Philips Research Laboratories, Eindhoven, the Netherlands, and deals with the investigations, processes and products of the laboratories and plants that form part of or cooperate with enterprises of the Philips group of companies. In the articles the associated technical problems are treated along with their physical or chemical background. The Review covers a wide range of subjects, each article being intended not only for the specialist in the subject but also for the non-specialist reader with a general technical or scientific training.

The Review appears in English and Dutch editions; both are identical in contents. There are twelve numbers per volume, each of about 32 pages. An index is included with each volume and indexes covering ten volumes are published (the latest one was included in Volume 40, 1982).

Editors:	Dr J. W. Broer Dipl.-Phys. R. Dockhorn, Editor-in-chief Dr E. Fischmann Dr J. L. Sommerdijk Ir N. A. M. Verhoeckx Ir F. Zuurveen
Editorial assistants:	Ing. P. Post T. M. B. Schoenmakers
English edition:	D. A. E. Roberts, B.Sc., M. Inst. P., A.I.L.

© N.V. Philips' Gloeilampenfabrieken, Eindhoven, the Netherlands, 1986.  
Articles may be reproduced in whole or in part provided that the source 'Philips Technical Review' is mentioned in full; photographs and drawings for this purpose are available on request. The editors would appreciate a complimentary copy.

## Contents

- An optical communication system with wavelength-division multiplexing and minimized insertion losses** 245

A. J. A. Nicia

*Optical waveguides for telecommunication show interesting physical aspects when system efficiency and transmission capacity are both maximized*

- Beam manipulation with optical fibres in laser welding** 262

C. J. Nonhof and G. J. A. M. Notenboom

*Replacing a stiff arrangement of mirrors by flexible optical fibres gives a versatile laser spot-welder*

- 50 years ago** 265

- The new centre for submicron IC technology** 266

W. G. Gelling and F. Valster

*The design and fabrication of integrated circuits that contain millions of extremely small transistors requires very large buildings*

- Dual-energy X-ray diagnostics** 274

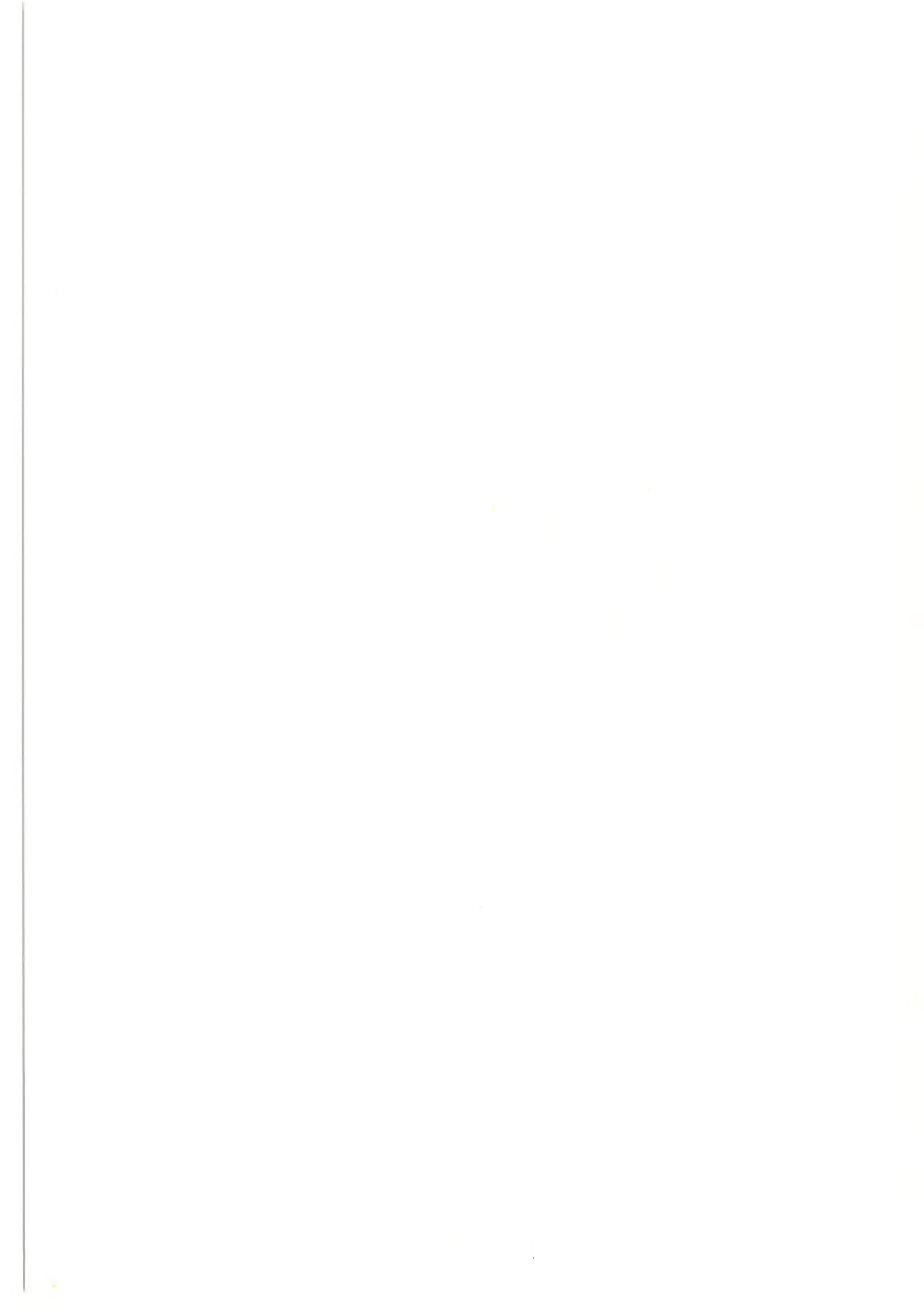
J. J. H. Coumans

*The radiologist can alter the contrast between tissues in an X-ray image with a simulated energy control*

- Optical transmission in the 1.55- $\mu\text{m}$  window** 286

- Scientific publications** 287

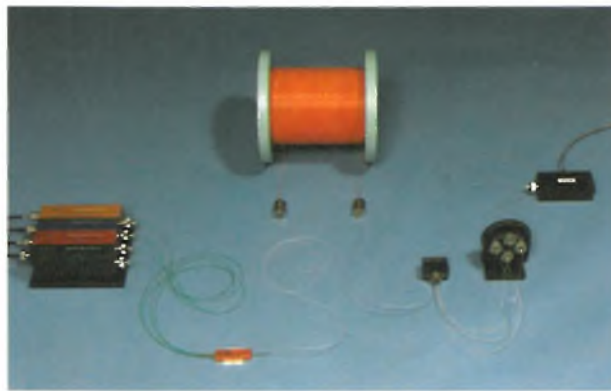




## An optical communication system with wavelength-division multiplexing and minimized insertion losses

### I. System and coupling efficiency

A. J. A. Nicia



Somewhere in the north-east of the United States there lies a rather strange 'vessel' for land-based training. It is a simulation of a cable-laying ship bearing the appropriate name 'Fantastic'. Before the year 1990 the 'Fantastic', sailing at eight knots, will have the task of laying the first optical-fibre cable to cross the Atlantic Ocean. This information can be found in Jeremy Bernstein's book 'Three degrees above zero — Bell Labs in the Information Age' (Charles Scribner's Sons, New York 1984). A voyage as unusual as this will undoubtedly attract much more attention than the 'journeys' of the flashes of light themselves inside the cores of the glass fibres ever could, even though they will travel beneath the Atlantic at a rate of 400 million knots, not eight knots. The present detailed study, to be published in two parts<sup>[\*]</sup>, of an optical communication system using wavelength-division (or colour) multiplexing demonstrates yet again how fascinating the physical background of guided light transmission for communications becomes when the main consideration is to minimize optical losses in transmission. Part II deals with the components developed for wavelength-division multiplexing and demultiplexing. These will eventually be used to increase the capacity of existing optical links in a relatively simple way.

#### Breakthrough

If the information society of the future is to function properly optical digital communication will almost certainly be required, and it looks as if the installation of a single optical fibre for each subscriber is a practical goal. Cable television and telephone can

then become part of an integrated system, with various other services in the broad field of information and communication. Possibilities already envisaged include video lending libraries, video telephony, and pay-TV (where viewers select television programmes

Dr Ir A. J. A. Nicia is with Philips Research Laboratories, Eindhoven.

[\*] Part II, 'Wavelength-division multiplexing', will appear in our next volume.



themselves, with payment per channel), local television broadcasts, newspapers by cable, and so on<sup>[1]</sup>.

This projected integration of information streams is the factor that could eventually make a subscriber network of this kind, built up from optical-fibre cables, economically feasible and profitable in a country such as the Netherlands. Since as many as 90% of all dwellings have a telephone and more than 70% already have cable television — with virtually separate distribution centres and links at present — the cable costs per connection in such an integrated subscriber network could remain comparable with those of the present telephone network.

Very large amounts of information can already be transmitted by optical-fibre cables more economically than by the conventional coaxial cable, and furthermore the price advantage is steadily shifting towards smaller transmission capacities. Optical-fibre cables therefore certainly qualify for use in situations such as the interconnection of new telephone exchanges.

In a cooperative venture between the Netherlands PTT (Postal and Telecommunications Service), the Delft and Eindhoven Universities of Technology and N.V. Philips it was decided to set up a small experimental local optical-fibre network at Philips Research Laboratories, Geldrop. The experimental system, known as DIVAC (an acronym for the Dutch words for digital connection between subscriber and exchange), has since been used to test the actual integration of different information and communication services<sup>[2]</sup>. The German PTT is also investigating such experimental networks, with about 30 to 50 connections, in some six cities.

It has been clear for some years that the technical aspects of this integration will have to be mainly concentrated in the transmission parts of the projected system, i.e. in the optical-fibre links<sup>[3]</sup>. An important argument for combining signals in a single fibre is the saving in cable costs thus obtained. This applies particularly to long-distance links, where plans to provide as many fibres as there are optical channels can hardly be considered realistic because of the excessive costs. For the local-area networks (LANs), the enormous expansion of communication facilities makes this combining of signals absolutely necessary. The installation of these LANs could pioneer the way for 'consumer optics' as an extension of consumer electronics. The aim is for all information streams to be combined in digital form and transmitted simultaneously along links of this type; at the receiving end they then have to be separated as required. The possibility of simultaneous signal transfers is also essential for two-way links via the same optical fibre, as for example in video telephony.

Colour multiplexing and demultiplexing, a main topic of this article, is a method that allows a number of optical signals to be combined at the input end of a

fibre and separated at the output end. In the method described here the separate signals are identified by the colour, or, to be more exact, the carrier wavelength: the method is therefore more generally known as 'wavelength-division multiplexing'. A good example of an element that can produce wavelength-division multiplexing is the familiar colour-dispersing prism. When the path of rays through such a prism is *reversed* a group of separate beams of light of different colour (red, green, blue, *fig. 1*) is seen to be combined by the prism to form a single beam of white light (the multiplexing operation). When the combined signals arrive at their destination, a second prism can be used to separate the original beams of different colour from the white beam (the demultiplexing operation).

In all optical-fibre cables so far installed for trunk (inter-city) links each fibre still needs its own light source and detector. This means that the combination and separation of the many types of information envisaged would really only be possible by electronic methods. Cost studies have meanwhile shown that these electronic combination and separation processes would be at a disadvantage, in view of the cost of new hardware, compared with the purely optical method of wavelength-division multiplexing and demultiplexing. Combined systems, partly electronic and partly optical, are also being considered<sup>[2]</sup>. In the rather

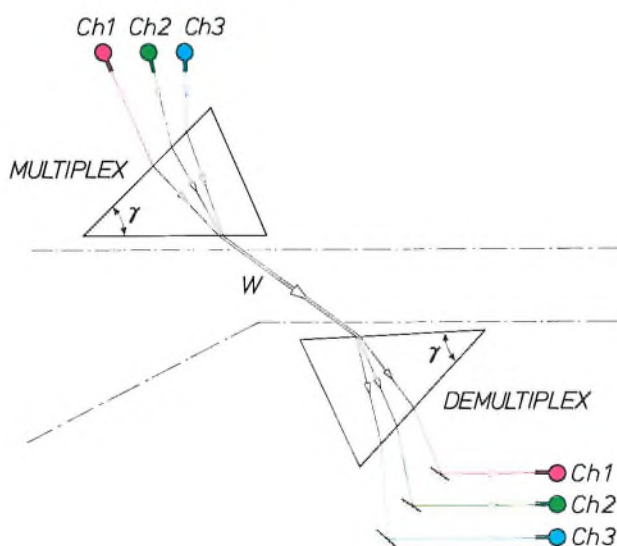
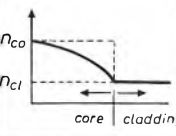
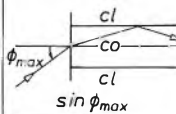


Fig. 1. An elementary example of a three-channel optical communication system in which signals are combined by wavelength-division multiplexing. Two prisms with a refracting angle  $\gamma$  are required. In the first (*MULTIPLEX*) the three signals are combined for long-distance transmission (*W*). At the receiving end is the second prism (*DEMULTIPLEX*), which restores the separate signals. Each signal is characterized by its own wavelength (or colour). This figure illustrates the principle of the WDM (Wavelength-Division Multiplexing) system dealt with in this article (see title photograph and fig. 3a). *Ch1,2,3* input and output of the three communication channels.

longer term it will be better if most or all of these processes are carried out optically. The various optical 'communication channels' would then have to be accommodated in a single optical fibre: these channels would have to be 'invisible' to one another; i.e. there would be no crosstalk between the separate channels.

fibres the bandwidth is not a practical limitation for optical communication, since there is no 'intermodal dispersion' by definition. The optical carrier wave has such a high frequency (about  $2 \times 10^{14}$  Hz) that the digital signal rates required by the PTT, such as 140 Mbit, or even 560 Mbit per second, are easily attainable. A

**Table I.** Numerical data characteristic of three generations of optical fibre cables. The attenuation, measured at three commonly used wavelengths, and the product of bandwidth and corresponding cable length, also determined experimentally, are the principal performance figures (grey background), 'Length' here is the maximum distance along the cable to the next repeater. The figures given are unlikely to be much improved in the near future. Theoretically, however, there is still room for improvement, since it can be shown that the 'absolutely best' profile of the refractive index for the multimode fibres of the second-generation cable would raise the maximum of  $2000 \text{ MHz} \times \text{km}$  by a factor of five to seven (see the chapter on 'Transmission system design' in the book by S. E. Miller and A. G. Chynoweth (eds)<sup>[9]</sup>). A  $\text{MHz} \times \text{km}$  product of 2000 corresponds to a broadening of the pulse signals of about 0.5 ns per km. Such pulses can be detected with good resolution after transmission over a distance of 1 km, provided that the repetition rate is less than 2000 MHz. The first four columns give the principal structural data of the fibres. The waveguide effect is based on total internal reflection, as indicated above the column for the numerical aperture of an optical fibre. The small radial decrease in the refractive index  $n_{co} - n_{cl}$  is the physical reason for the confinement of the radiation within the fibre cores; in the axial direction the refractive index does not normally vary at all. *co* core. *cl* cladding. *n.a.* not applicable.

cable generation	refractive index 	radius ( $\mu\text{m}$ )		fibre volume ( $\text{cm}^3/\text{km}$ )	numerical aperture 	attenuation ( $\text{dB}/\text{km}$ )			bandwidth $\times$ length ( $\text{MHz} \times \text{km}$ )
		core	core + cladding			$\lambda = 1300 \text{ nm}$	$\lambda = 1550 \text{ nm}$	$\lambda = 930 \text{ nm}$	
3 single-mode fibres	step-index $n_{co} - n_{cl} \approx 0.0034$	4.5	62.5	12.3	0.1	0.40	0.25	n.a.	> 100 000
2 multimode fibres	parabolic $n_{co} - n_{cl} \approx 0.014$	25	62.5	12.3	0.2	0.60	n.a.	2.1	1000 to 2000
1 multimode fibres	step-index $n_{co} - n_{cl} \approx 0.030$	50	70	15.4	0.3	n.a.	n.a.	2.1	50

The breakthrough of transmission by optical fibre has now reached the point where designers are already familiar with the idea of being able to base their plans for new systems on optical-fibre cables of the second or even third generation (Table I). Since 1976, when an issue of this journal was entirely devoted to optical communication<sup>[4]</sup>, the development of the various types of fibre has certainly not stood still. The most significant advance is probably the reduction of the optical attenuation per km, achieved through the production of extremely pure glass (fig. 2). This high purity is now attainable on an industrial scale<sup>[5]</sup>; single-mode fibres (for third-generation cables) are now being produced in which the optical attenuation is less than 0.5 dB/km, which means that a telephone conversation can be transmitted by such a fibre over a distance of about 40 km without significant loss of quality and without any regeneration. In single-mode

single-mode fibre, with a core diameter of  $9 \mu\text{m}$  (about one tenth that of a human hair), can therefore carry thousands of telephone conversations simultaneously, with no crosstalk.

In the multimode fibres for second-generation cables the situation is different. As the maximum repeater spacing is increased, the permissible bandwidth for telecommunication decreases correspondingly. With these fibres, therefore, the maximum repeater spacing

[1] This subject is under consideration by the European Community in its 'RACE Initiative'. RACE (Research for Advanced Communications technologies for Europe) is a telecommunications programme now in the definition phase.

[2] J. van der Heijden, DIVAC — an experimental optical-fibre communications network, Philips Tech. Rev. 41, 253-259, 1983/84.

[3] W. J. Tomlinson, Wavelength multiplexing in multimode optical fibers, Appl. Opt. 16, 2180-2194, 1977.

[4] Philips Tech. Rev. 36, 177-216, 1976.

[5] In November 1983 Philips opened a new optical-fibre factory in Eindhoven; both multimode and single-mode fibres are manufactured here on a commercial scale.

has a clear correlation with the bandwidth, and is far less limited by attenuation.

It will be clear that any work, including research, on components for wavelength-division multiplexing and demultiplexing is most effective within the context of a complete system study. A complete communication system contains both the transmitting and receiving ends as well as the central section for the new method of optical signal transmission.

Part I of the article, following this introduction, will therefore deal in general terms with the system that has been designed, a WDM ('Wavelength-Division Multiplexing') system giving maximum coupling efficiency. The propagation of the (infrared) 'light' will be described with the aid of a block diagram, and subjects that will be dealt with are the various optical interfaces, the boundary conditions and ways and means of manipulating the radiation, with the primary object of minimizing the insertion losses in the system.

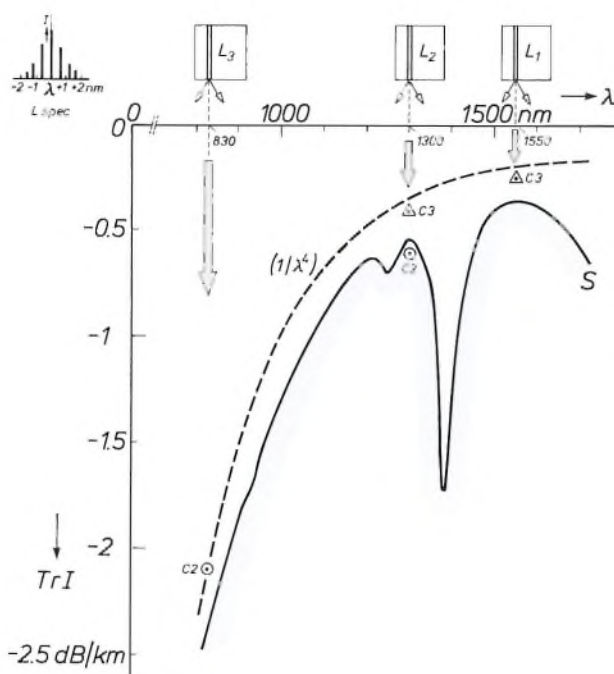


Fig. 2. Example of a transmission spectrum ( $S$ ) measured on an optical fibre more than 2 km long, of the type mounted in the second-generation cables (Table I). This type is now in regular production [5]. Vertical:  $TrI$ , the transmission of radiation, in decibels per kilometre. Horizontal: the wavelength  $\lambda$  of the infrared test radiation, in nm. The wavelengths of three lasers ( $L_1$ ,  $L_2$ ,  $L_3$ ) that can be used in optical communication systems are displayed on the horizontal axis. Near the origin of the coordinate system the extremely narrow emission spectrum ( $L_{spec}$ ) of one of the many types of diode laser is shown. The nature of the material of the fibre core and its impurities determine the material dispersion; this unwanted effect decreases as the spectrum of the light guided through the core becomes narrower. In practice the effect is not large enough to be troublesome. The dashed curve ( $1/\lambda^4$ ) shows the calculated transmission spectrum when Rayleigh scattering is the only source of attenuation.  $C_2$  and  $C_3$  irradiances derived from the maximum performance figures in Table I, found in cables of the second and third generations. The sharp dip in  $S$  at about 1380 nm is caused by resonances (valence vibrations) of free OH groups, which are present as traces in the core material.

Part II of the article will chiefly be concerned with the multiplexing and demultiplexing components of our WDM system. Considerable emphasis will be placed on the choice of design and construction. The operation of these components will be briefly explained, and some theoretical principles and background will be discussed.

### Principles of system design

The general block diagram of a WDM system is shown in *fig. 3*. As in any communication system, the diagram can be divided into three main parts: (I) the transmitter section, where in this case three independent electrical signals are converted into infrared signals with the wavelengths  $\lambda_1$ ,  $\lambda_2$ , and  $\lambda_3$ ; (II) the transmission section proper with — in our case — a second-generation optical cable, which therefore contains one multimode fibre ( $F$ ) with a parabolic refractive-index profile (see Table I); (III) the receiver section for the composite optical signal, where finally the three original signals, each in their own channel, reappear at the outputs as digital electrical signals. Although compatible with current ideas, our choice of *digital* signals is not essential, and indeed the system is 'transparent' in this respect, since the laser injection currents could equally well be modulated by *analog* signals.

As we shall see in part II, the number of parallel optical channels used in  $F$  will be limited to three or four. (The title photograph shows our experimental system with *four* input channels.) Given the known designs for multiplexing and demultiplexing units, the use of more channels would soon introduce considerable practical difficulties. The demultiplexing unit seems to give fewer problems here, and indeed a demultiplexing unit for *six* parallel channels has now been developed [6].

The main principle behind the design of our WDM system is the achievement of maximum efficiency, i.e. minimizing the insertion losses. In the design of such a system certain more or less fixed conditions have to be observed, but a number of variables can be freely chosen so as to comply with the main principle. The main conditions are set by the characteristics of the multimode fibre ( $F$  in *fig. 3*) in the second-generation cables, as shown in Table I. Major factors in the design are the core radius and the numerical aperture, the first two of the fixed parameters.

[6] H. G. Finke, A. J. A. Nicia and D. Rittich, Diffraction efficiency limited grating demultiplexer suitable for up to six channels with arbitrary central wavelengths, Proc. 4th Int. Conf. on Integrated optics and optical fibre communication (IOOC), Tokyo 1983, pp. 376-377.



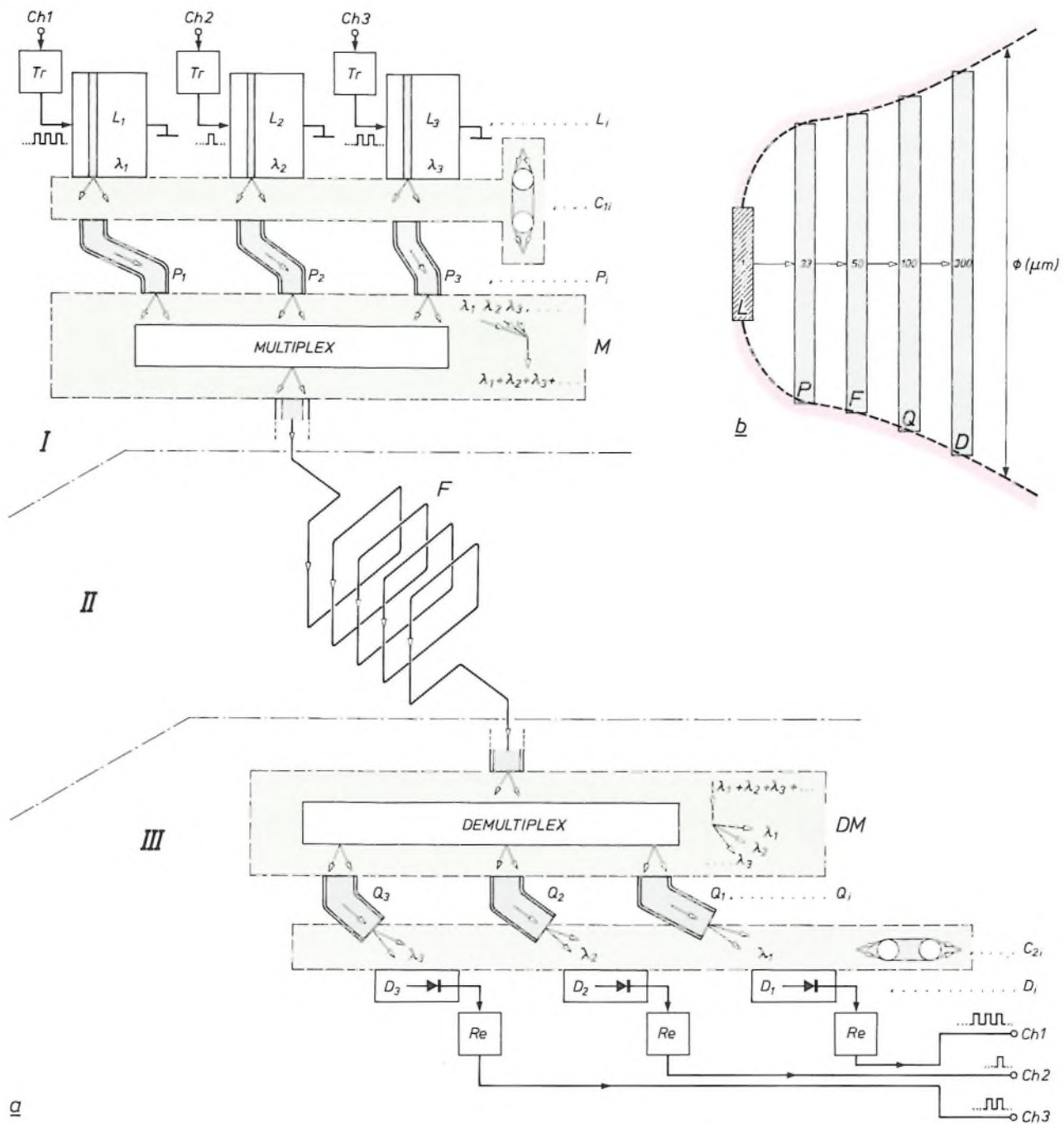
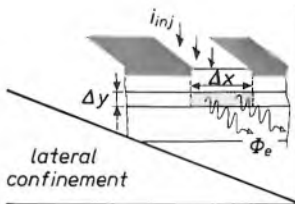


Fig. 3. a) A wavelength-division multiplexing system for optical communication. The multiplex component (*M*) is in the transmitter section (*I*), the demultiplex component (*DM*) in the receiver section (*III*). As an example, three separate communication channels are shown, indicated by *Ch1*, *Ch2* and *Ch3* at the input and output terminals. (As can be seen in the title photograph, four parallel channels are also a practical proposition.) The three combined signals propagate through one optical fibre (*F*) of the multimode type in second-generation cables, in the region (*II*) for long-distance transmission. *Tr* transmitter, which modulates the injection current of the diode laser connected to it ( $L_1$  ( $\text{In}_{\mu}\text{Ga}_{1-\mu}\text{As}_v\text{P}_{1-v}$ ),  $L_2$  ( $\text{In}_{\mu'}\text{Ga}_{1-\mu'}\text{As}_v\text{P}_{1-v}$ ) and  $L_3$  ( $\text{Al}_x\text{Ga}_{1-x}\text{As}$ ), see also fig. 4) in accordance with the required digital input signal. *Re* receiver, which restores the appropriate digital input signal from the photocurrent of the detector ( $D_1$ ,  $D_2$ ,  $D_3$ ) and feeds it to the output terminals.  $P_1$ ,  $P_2$ ,  $P_3$  pigtailed with a parabolic refractive-index profile for the core.  $Q_1$ ,  $Q_2$ ,  $Q_3$  pigtailed with step-index core material (multimode). Green blocks: interface zones: containing optical coupling elements, often very simple ( $C_{1i}$ ,  $C_{2i}$ ,  $i = 1, 2, 3$ ; symbolically represented by a pair of ball collimator lenses). b) The 'trumpet geometry' chosen for the system (the red dashed-line contour). *L* laser. *P* pigtail for input signal. *F* long-distance fibre. *Q* pigtail for output signal. *D* detector.  $\phi$  characteristic diameter, available for signal guidance. Because of the increase in  $\phi$  in the direction of propagation of the guided signal the various couplings between the components *L*, *P*, *F*, *Q*, *D* are easy to arrange mechanically. The value quoted for *L* (1 μm) is only an order of magnitude; there is also no rotational symmetry.

The numerical aperture ( $NA$ ) is a measure of the ability of the fibre core to capture radiation and guide it, by repeated total internal reflection. For the radiation originating from a point source outside the fibre core on the optical axis, it can be shown that  $NA$  is equal to  $(n_{co}^2 - n_{cl}^2)^{1/2}$ , the maximum possible value of the numerical aperture for the fibre core.

The third standardized parameter, the thickness of the cladding, is not so important. Another major con-

dition is the detector ( $D_i$  in fig. 3). The type of photodiode chosen has a radiation-sensitive surface of about 300  $\mu\text{m}$  diameter. This dimension, which determines the capacity of the photodiodes, sets a limit of about 500 MHz to the rate of response. Signals in which significantly higher frequencies occur would require photodiodes of smaller diameter. This, however, would require tighter tolerances for the



		laser material			
lateral confinement		$Al_{0.10}Ga_{0.90}As$	$Al_{0.02}Ga_{0.98}As$	$In_{0.76}Ga_{0.24}As_{0.54}P_{0.46}$	$In_{0.60}Ga_{0.40}As_{0.83}P_{0.17}$
		$\Delta x = 5 \quad \Delta y = 0.2$			
gain-induced guiding	$\lambda = 0.83$ $\Phi_e = 5$ $M_e = 2$	$\Psi_{axis}'' = 25$ $\Psi_{axis}' = 65$ $\epsilon = 2.5$ $\Delta \approx 20$	$0.87$ $5$ $2$	$25$ $65$ $\approx 20$	no
		$PP^-$	$PP^-$	$\approx 20$	no
index guiding	$\Delta n = 0.01$ ('weak')	$0.83$ $5$ $2$	$0.87$ $5$ $2$	$1.30$ $5$ $2$	$1.55$ $5$ $2$
		$PP$	$PP$	$p^+$	$p^+$
		$\Delta x = 1.5 \quad \Delta y = 0.2$			
index guiding	$\Delta n = 0.10$ ('strong')	$0.83$ $5$ $7$	$0.87$ $5$ $7$	$1.30$ $5$ $7$	$\lambda = 1.55$ $\Phi_e = 5$ $M_e = 7$
		$p$	$p$	$p$	$\Psi_{axis}'' = 40$ $\Psi_{axis}' = 65$ $\epsilon = 1.5$ $\Delta \approx 0$

Fig. 4. Ten types of diode laser arranged in a matrix of characteristics with the choices of active material and lateral confinement mechanism as inputs<sup>[7]</sup>. The active 'stripe' has the lateral dimension  $\Delta x$  in its principal plane of symmetry, and perpendicular to it the dimension  $\Delta y$ , both in  $\mu\text{m}$ . In the  $y$ -direction the confinement of the radiation in all ten cases is the consequence of an abrupt step in the refractive index at the position of the two 'horizontal' boundary planes of the active stripe.  $\lambda$ , in  $\mu\text{m}$ , wavelength of the laser radiation.  $\Phi_e$ , in mW, the radiant power.  $M_e$ , in  $\text{mW}/(\mu\text{m})^2$ , the radiant exitance.  $\Psi_{axis}''$ ,  $\Psi_{axis}'$ , in degrees, the far-field beam divergence angle, in the principal plane of symmetry and in the plane of symmetry perpendicular to it.  $\epsilon$  the ellipticity, the ratio of the smallest beam diameter (or 'waist') in the laser in the principal plane of symmetry, to the waist in the longitudinal plane of symmetry perpendicular to it.  $\Delta$  the astigmatism, in  $\mu\text{m}$ : the distance between the two waists within the laser (one waist is situated exactly at a reflective end face of the laser, see fig. 5). *no* type of no practical use. *PP* very common type. *P* common type. *p* uncommon type. - use on the decline, + use on the increase.  $i_{inj}$  injection current, which effects the population inversion required for laser action. The development of new types of diode laser certainly does not seem to have run its course yet<sup>[8]</sup>. 'Distributed feedback', introduced by making a longitudinal periodic discontinuity in the refractive index, will not only help to make the emission spectrum narrower but will also make it easier for the system designer to choose the appropriate wavelengths, which will of course facilitate the introduction of wave-length-division multiplexing.

dition is the choice of the laser light source ( $L_i$  in fig. 3). The different types of diode laser that seem at present to be most suitable for optical communications (fig. 4) produce a light spot about one  $\mu\text{m}$  square at their output with a radiation pattern like an elliptical cone. The

dimensions and alignment of the optical coupling ( $C_{2i}$  in fig. 3).

The more or less free variables here are the short pieces of fibre,  $P_i$  and  $Q_i$  in fig. 3, referred to as 'pig-tails', and the multiplexing and demultiplexing units

( $M$  and  $DM$  in fig. 3). In the pigtailed, whose core material has a parabolic or stepped refractive-index profile (the  $Q_i$ 's only), the variables are the numerical aperture and the core radius. The values chosen for the  $P_i$ 's must be large enough to ensure that the radiation pattern from the laser matches them properly and for the coupling elements  $C_{1i}$  to be kept simple. The insertion loss due to the interfaces should be kept as small as possible. The interfaces between the end of the  $P_i$ 's and the  $M$  unit are less critical in this respect. The explanation lies in the 'trumpet' geometry used for the system (fig. 3b): the signals are guided inside a 'characteristic diameter' that either increases along the axis of propagation or remains constant (and therefore never decreases). For the pigtailed at the output of the optical parts, the  $Q_i$ 's, the situation as a whole is thus easier. It is fortunate that there is considerable scope for variation in the  $DM$  unit and also in the  $M$  unit, especially because the range of possible variations is based on a choice between different operating principles here (see Table III, in part II of this article [\*]).

In the rest of the discussion of the block diagram we shall follow the 'natural' sequence step by step, as the radiation propagates through the system, although there is one exception right at the start. We begin in fact with the four green blocks in fig. 3a, the optical interface zones. This is because an accurate analysis of the interface components and their possible radiation leaks becomes relatively more important for maximizing the *total* system efficiency as the performance of the main components such as lasers and fibres improves. First we shall look at the interface zone immediately following the lasers; analysis of this zone was the one that presented most of the difficulties, which were mathematical. The treatment of the second and third interface zones, which was much simpler, will be given in part II of this article, since their characteristics are closely connected with the structure of the  $M$  or  $DM$  units that they contain. The fourth interface zone, between pigtailed and photodiodes, will however be treated in this part. In view of the strongly pronounced trumpet geometry of the system, it should not be too difficult to estimate the efficiency of the fourth zone once the efficiency of the first zone has been properly calculated.

### The interface zones

In the first interface zone ( $C_{1i}$  in fig. 3a) a laser and a pigtail for an input signal are coupled together. The efficiency of this coupling interface is in the region of 50 to 80 per cent, as will appear later. The radiation leaves the laser directly through a partly transmitting 'mirror', one of the two end faces perpendicular to

the active stripe of the laser [8]. The radiation next passes through the actual coupling element to reach the front face of the appropriate pigtail ( $P_i$ ) and is then guided through the fibre core. A small single ball lens has proved satisfactory as a coupling element, in the form of a glass bead with a radius of 0.1 mm. The bead is provided with an antireflection coating.

The ball lens corrects the divergence of the beam. The cross-section of the beam at this front face is therefore given dimensions that correspond reasonably well with the diameter of the central region in the core, the region where the energy of the fundamental mode of a guided electromagnetic wave pattern in the core is concentrated. As will be seen below from the approximate description given here the fundamental mode, compared with higher-order modes also excited, is mathematically the simplest wave pattern — and it also remains the most strongly concentrated one — to ensure that the energy of the beam is transferred through the full length of the fibre [9].

The efficiency of the first interface zone does not only depend on the ball lens, of course. It is also strongly dependent on the properties of the wave pattern that can be excited inside the next element ( $P_i$ ), starting at its front face. In our examination of the interface zones we shall therefore first take a closer look at the propagation modes inside a fibre core.

### Modes

Inside a fibre core types of resonant electromagnetic wave patterns can be excited, called modes. They are important because a general solution for the guided-radiation field inside the fibre core can always be obtained as a sum of a complete set of modes (the superposition principle), which can be calculated relatively easily. The radiation is propagated longitudinally, in the  $z$ -direction. A mode is characterized by a well-defined phase velocity and an energy velocity (or group velocity), a state of polarization, and its transverse distribution functions, which are expressed

[7] The editors are indebted to Prof. Dr G. A. Acket of Philips Research Laboratories, and a Visiting Professor of Delft University of Technology, for his detailed help in drawing up this matrix.

[8] G. A. Acket, J. J. Daniele, W. Nijman, R. P. Tjiburg and P. J. de Waard, Semiconductor lasers for optical communication, Philips Tech. Rev. 36, 190-200, 1976. See also G. D. Khoe and L. J. Meuleman, Light modulation and injection in optical-fibre transmission systems with semiconductor lasers, Philips Tech. Rev. 36, 201-204, 1976. Various other developments are described in L. J. van Ruyven, Double heterojunction lasers and quantum well lasers, J. Lumin. 29, 123-161, 1984.

[9] M. J. Adams, An introduction to optical waveguides, Wiley, Chichester 1981; D. Marcuse, Light transmission optics, Van Nostrand Reinhold, New York 1972; S. E. Miller and A. G. Chynoweth (eds), Optical fiber telecommunications, Academic Press, New York 1979.

in terms of the coordinates  $(x, y)$ . Since the refractive-index profile in the core is independent of  $z$ , the transverse distribution functions are independent of the value of  $z$ . This means that the components of the field vectors  $\mathbf{E}$  and  $\mathbf{H}$  of a given mode all have the same fixed, functional dependence on both  $x$  and  $y$ . However, depending on the appropriate boundary conditions, there can be differences in amplitude and phase between the various components of the field vectors. The two coordinates are *separated* variables here; this rather unusual feature is due to the choice of the refractive-index profile.

The modes are of two kinds: 'bound' or guided modes and 'leaky' modes. In the first kind the value of the transverse distribution functions decreases rapidly to zero as the distance from the  $z$ -axis increases, so that outside the core the field energy is practically zero. If the energy were predominantly transported by leaky modes, the fibre would be not so much a waveguide as an antenna emitting radiation.

In describing radiation fields it is customary to assign the well-known time-dependence  $\exp(j\omega t)$  of the harmonic oscillator to the bound modes, while the  $z$ -dependence, because of the longitudinal propagation, appears only in the phase factor  $\exp(-j\beta z)$ . The modes can then be expressed as a function of the four variables  $(x, y, z, t)$  by

$$M(x, y, z, t) = X(x)Y(y) \exp\{j(\omega t - \beta z)\}. \quad (1)$$

Their wavefronts are planar; they will travel a distance  $\lambda_0/n_{co}$  in the  $z$ -direction inside the fibre core in the time  $(2\pi/\omega)$  for one oscillation. The propagation constant  $\beta$ , which has the dimension of a wave number, is approximately equal to  $2\pi n_{co}/\lambda_0$ . In this approximation the difference  $\omega t - \beta z$  therefore remains *constant* during the propagation of the radiation; in this case the guidance of the radiation is said to be 'ideal'. A hypothetical observer of the constancy of the difference will therefore move with the light waves at the 'phase velocity'.

The dielectric constant does not vary at all in the  $z$ -direction inside the fibre core. We can assume that its variation in the lateral direction is slow enough for its gradient to be negligible. This has the advantage that Maxwell's equations — which in principle will give a complete solution for the modes for given boundary conditions — then reduce to a Helmholtz equation, which is much more manageable. It is also known as the reduced scalar wave equation for the modes:

$$\frac{\partial^2 M}{\partial x^2} + \frac{\partial^2 M}{\partial y^2} + \{n^2(x, y)k_0^2 - \beta^2\}M = 0. \quad (2)$$

This equation applies to all the components of the electric and magnetic field-strengths. The function  $n(x, y)$  is the refractive index of the core material;  $k_0$  is a constant (the wave number in free space,  $2\pi/\lambda_0$ ). In the parabolic material preferred here, also referred to as a square-law guiding medium, the following relation applies:

$$\begin{aligned} n(x, y) &= n_{co}\{1 - g^2(x^2 + y^2)\}^{1/2} \\ &\approx n_{co}\{1 - \frac{1}{2}g^2(x^2 + y^2)\}, \end{aligned} \quad (3)$$

provided, of course, that  $(x^2 + y^2)^{1/2}$  remains smaller than the core

radius;  $g$  is a focusing constant. It can be seen in equation (3) that the coordinates  $x$  and  $y$  occur as separated variables.

As noted, certain boundary conditions have to be observed when finding the modes. It is fairly evident, for example, that both  $X(x)$  and  $Y(y)$  in eq. (1) must tend to zero when  $x$  and  $y$  tend to infinity. The rate at which they do so must also be fast enough to ensure that there is no divergence of the integral of the field energy. It is also assumed that  $\frac{1}{2}g^2(x^2 + y^2) \ll 1$ , at least within the core — because of this inequality said to be 'weakly guiding' — and that the change in the refractive index in distances of a wavelength or less is negligibly small. The latter condition is always met in practice.

Equation (2) can now be solved after some mathematical manipulation to transform it into two ordinary differential equations, one for  $X(x)$  and the other for  $Y(y)$ . Both differential equations are of the type used in quantum mechanics for describing the bound states of the one-dimensional harmonic oscillator mentioned above. The known solutions, which contain the function of the Gaussian distribution and a Hermite polynomial, are therefore applicable to the present case.

On the basis of the formal equivalence between a general radiation field and a number of harmonic oscillators (here both in the  $x$ -direction and in the  $y$ -direction, the two transverse directions within the fibre core) the following mathematical expressions can be found for the propagation modes in a core of the type with a parabolic refractive-index profile (Table I) as a function of the four coordinates  $(x, y, z, t)$ :

$$\begin{aligned} M(x, y, z, t) &= (\pi 2^{m+n-1} m! n! w_0^2)^{-1/2} H_m\left(2^{1/2} \frac{x}{w_0}\right) \times \\ &\quad \times H_n\left(2^{1/2} \frac{y}{w_0}\right) \exp\{-(x^2 + y^2)/w_0^2\} \times \\ &\quad \times \exp\{j(\omega t - \beta_m z)\}, \end{aligned} \quad (4)$$

where  $m$  and  $n$ , independently of each other, may assume all values in the sequence 0, 1, 2, 3, 4, ... . The  $z$ -coordinate used here is calculated along the optical axis of the core. The functions  $H_m$  and  $H_n$  are Hermite polynomials<sup>[10]</sup> of order  $m$  and  $n$ ; together with  $\exp\{-(x^2 + y^2)/w_0^2\}$ , a (two-dimensional) Gaussian distribution function, they determine the transverse dependence of the various modes — which are therefore often referred to as Hermite-Gauss field distributions. In eq. (4) the propagation constant  $\beta$  is also 'labelled' by the mode numbers,  $m$  and  $n$ , to indicate that it cannot represent a continuum of values, just as in quantum mechanics the energy of a harmonic oscillator can only assume discrete values. The constant  $w_0$ , a parameter of the core, will be dealt with separately later.

The modes can be divided into 'groups'. Within each group the *sum* of the mode numbers  $m$  and  $n$  is the same for all modes — which, as we shall see, implies that the propagation constant has the same value for all modes in the group, and thus characterizes a particular group (see eq. (6) below).



The expressions (4) may be used as modes for the formation of all components of both the electric and the magnetic field. In the case of a fundamental mode we use the expression for which  $m = n = 0$ ; the relevant polynomials are then equal to 1 and the transverse dependence is completely determined by the Gaussian distribution function. The field distribution associated with the fundamental mode in the core is very important for the coupling, since more than 99% of the laser radiation itself is present in the field distribution corresponding to the *laser* fundamental mode, which is also purely Gaussian (or normal). The coupling is of course improved by this correspondence.

A fibre core with zero loss of radiation energy is an unattainable ideal. In an actual material bound modes have losses that increase with their mode numbers ( $m$  and  $n$ ). Because of these losses, any given mode pattern in the core tends to degenerate into the fundamental mode as  $z$  increases. Since it is more concentrated about the axis, this mode will continue to exist longest and therefore propagate farthest. Also, a coupling between a fundamental mode and a higher-order mode always gives higher losses than a coupling between one fundamental mode and another [11].

#### Maximum matching

The art of coupling consists mainly in producing the best match between the near-field pattern of the laser radiation and the fundamental mode of the radiation field that can be excited in the fibre core — which may be considered as a dielectric waveguide inside a sheath or cladding, both with local cylindrical symmetry. The interface zone and the core of the fibre that follows it must also be ‘matched’ to ensure a continuous concentration of the optical energy along the axis — this is of course an essential contribution to the optical efficiency of the complete system.

Unfortunately, two of the characteristics of the available lasers are not very helpful here: their astigmatism and their ellipticity. Two of the AlGaAs types have both (fig. 4), with the result that more than 60% of the laser radiation will excite groups of higher-order modes inside the core. The excitation of higher orders will in any case cause an extra loss of concentration, compared with the fundamental mode. The first ten of these groups, with the bound modes, do make some contribution to the guidance of the electromagnetic energy; but with the leaky modes serious losses occur in guidance over distances of more than say 1000 wavelengths.

Two constants in eq. (4), the ‘characteristic spot parameter’ ( $w_0$ ) and the propagation constant ( $\beta_{m,n}$ ) mentioned earlier, should be treated separately here since they help to determine the concentration of the energy at the axis.

#### Characteristic spot parameter and propagation constant

In the derivation of eq. (4) dimensionless spatial coordinates are necessary. The unit of length adopted here is the characteristic spot parameter,  $w_0$ . This is defined by:

$$\frac{1}{2} NA \times \frac{w_0^2}{a} = \frac{\lambda}{2\pi}, \quad (5)$$

where  $NA$  is the (maximum) numerical aperture of the core and  $a$  its radius.

We can see from eq. (5) that the quantities  $a$  and  $NA$ , which are of importance for the system design, therefore determine the characteristic spot parameter of the core at a given wavelength. Thinking mainly of guidance in the fundamental mode, we see from eq. (4) that at the distance  $w_0$  away from the optical axis (this distance is about 7  $\mu\text{m}$  for the pigtailed  $P_i$ ) the amplitude of the field will have fallen to about  $1/e$  of the maximum value. The irradiance there will therefore be as much as  $e^2$  times smaller than on the axis. The length  $w_0$  consequently functions as the radius of a circle (the ‘spot’). As the characteristic spot parameter decreases, the electromagnetic energy becomes more concentrated around the axis of the core; this effect is strongest for the fundamental mode.

The propagation constant  $\beta_{m,n}$  in eq. (4) derives its importance from the fact that it determines the magnitude of the velocity of energy transfer — or, more directly: of the velocity of power transfer — for the various groups of modes. The interesting thing is that it is only in core material with a parabolic refractive-index profile that these velocities are to a good approximation equal for the various groups. In practice this has the consequence that the intermodal dispersion — which broadens the signal pulses along the axis in proportion to the propagation time, and which can cause unacceptable intersymbol interference — remains two orders of magnitude smaller in this core material than in fibres where the refractive index has a stepped profile. This improves the transmission capacity of the parabolic material correspondingly.

Like the characteristic spot parameter of the core, the propagation constant also appears as the square in the mathematical manipulations used for the derivation of (4):

$$\beta_{m,n}^2 = \frac{1}{c^2} n_{co}^2 \omega^2 \left\{ 1 - 2(m+n+1) \frac{cNA}{\omega n_{co}^2 a} \right\}, \quad (6)$$

[10] L. Pauling and E. B. Wilson Jr., Introduction to quantum mechanics, McGraw-Hill, New York 1935.

[11] H. Kogelnik, Coupling and conversion coefficients for optical modes, in: J. Fox (ed.), Proc. Symp. on Quasi-optics (New York 1964), Polytechnic Press, Brooklyn, NY, 1964, pp. 333-347.

where again  $m, n = 0, 1, 2, 3, 4, \dots$ ;  $c$  is the velocity of light and  $\omega$  the angular frequency. From eq. (6), after taking the square root and expanding as a series:

$$\beta_{m,n} \approx \frac{1}{c} n_{co} \omega - (m+n+1) \frac{NA}{n_{co} a}. \quad (7)$$

From this result it can be seen that the energy-transfer velocity, which is equal to the group velocity ( $= 1/(d\beta_{m,n}/d\omega)$ ), does not to a first approximation depend on the mode numbers  $m$  and  $n$ . If an exact calculation is made, a dependence on the mode numbers does emerge, with the restriction that they always appear as a sum  $(m+n)$  — typical of the various *groups* of modes.

The approximate values for  $\beta_{m,n}$  found in eq. (7) are valid only when the modes are of such low order that  $2(m+n+1)cNA/(\omega n_{co}^2 a)$  is sufficiently small, in relation to 1, for the series to be terminated after two terms. An even greater restriction on the useful modes arises from the fact that the parabolic material does not of course fill the entire space; it extends only a distance  $a$  from the axis of the fibre. The higher the mode numbers, the further the mode pattern extends from the axis (this reflects the behaviour of the Hermite polynomials). Beyond a certain mode number the power contained in the modes will tend to lie in the zone of the cylindrical interface. In this situation such modes will rapidly lose power and, as leaky modes, will then contribute little if anything to the *guidance*.

The theory shows that the wave equation for the modes gives an oscillatory behaviour — in the lateral direction, corresponding to 'leakage' — at positions where  $n^2(x,y)k_0^2$  exceeds  $\beta_{m,n}^2$ , and an exponentially decaying behaviour (i.e. 'guidance') at positions where  $n^2(x,y)k_0^2$  is smaller than  $\beta_{m,n}^2$ . With D. Marcuse<sup>[12]</sup> we may therefore locate the 'cut-off' for the guidance in our core at the largest value  $L$  of the sum  $m+n+1$ , for which the propagation constant is still dominant:

$$n^2(a)k_0^2 < \beta_{m,n}^2, \quad (8)$$

where  $a = (x^2 + y^2)^{1/2}$  and  $m+n+1 = L$ . From equations (6) and (8) it can be shown that  $L$  is the largest integer that satisfies

$$L < \frac{1}{2} \frac{\omega}{c} a NA. \quad (9)$$

On substituting the appropriate data from Table I in eq. (9), we find confirmation that the first ten groups in the multimode fibres of second-generation cables do indeed include these bound modes. Modes of still higher order do not, as we have seen, make any significant contribution to the efficiency of the first interface zone, or may even reduce it. Fortunately, however, they are only weakly excited.

### Free space and Gaussian beams

Before a pigtail can be reached, the laser beam must first travel two short distances in 'free space' (air in fact) in the interface zone, in front of the ball lens and

after it; the ball lens is the coupling element in this zone, as mentioned earlier. Since it was necessary to match the two fundamental modes as well as possible, we first established how exactly the excited laser fundamental mode would propagate as a radiation field directly linked to the end face of the laser.

The mathematical treatment again contains considerable simplification because the two spatial variables ( $x, y$ ) occur separately. In such a region of free space the irradiance on the  $z$ -axis always has the maximum value, as would be expected in view of the existing symmetries in the laser. The calculations showed that at right-angles to the optical axis the irradiance decreases in a pure Gaussian curve as a function of  $x$ , the coordinate in the major plane of symmetry — assumed to be horizontal — of the active 'stripe' in the laser<sup>[13]</sup>. As a function of  $y$ , i.e. in the vertical plane of symmetry, the decrease is also purely Gaussian, although at a different rate.

The two two-dimensional beams, whose field distributions give the total fundamental-mode field after multiplication, differ only in their 'effective' widths — which of course must always be compared at the *same* value of  $z$ . The cause of these differences lies in the different mechanisms for the 'confinement' (or guidance) of the radiation inside the laser in the related horizontal and vertical directions. The 'effective' widths of the two beams are established by means of the  $1/e$  contour points, in other words the values of  $x$  and  $y$  at which the irradiance has fallen to  $(1/e)^2$  of the value on the axis, taken at the same  $z$ .

The two beams, which are called 'Gaussian beams' to indicate their type, each originate from an initial constriction or 'waist', where their wavefront can be represented by a straight line. The initial waist of the beam is real in the vertical symmetry plane and located exactly at one of the end faces of the laser; the initial waist of the other beam is virtual and located towards the front, inside the laser. The distance between them varies from about 1  $\mu\text{m}$  or less (denoted in fig. 4 by ' $\Delta \approx 0$ ') to 15  $\mu\text{m}$  or even more ( $\Delta \approx 20$ ' in fig. 4). The longitudinal dimension of the two waists has a maximum value of a few  $\mu\text{m}$ ; the exact values depend on the type of laser used, of course. Since the waists do not coincide, the exit beam from the laser has the undesirable feature, mentioned earlier, that it is strongly astigmatic. When the radiation propagates in free space the two (planar) Gaussian beams will start to fan out (fig. 5). As the initial waist decreases the

<sup>[12]</sup> D. Marcuse, The impulse response of an optical fiber with parabolic index profile, Bell Syst. Tech. J. 52, 1169-1174, 1973.

<sup>[13]</sup> The calculations for the whole of the first interface zone are most simply performed when the coordinates  $x$  and  $y$  for equation (4), treated earlier, are the same as the coordinates here, chosen to suit the structure of the laser (fig. 4).

angle in free space in which rays of the beams can be encountered becomes larger. The emergent wavefront approximates to an arc of a circle.

In the paraxial approximation the radius of curvature of such a circular wavefront is equal to:

$$R(z) = z \left\{ 1 + \left( \frac{\pi w_{in}^2}{\lambda_0 z} \right)^2 \right\}, \tag{10}$$

where  $w_{in}$  is a measure equal to half the appropriate initial waist. The coordinate  $z$  is measured from the initial waist. It can be seen from eq. (10) that the wavefront can be approximated by a straight line for both small and large values of  $z$  (the curvature,  $1/R(z)$ , is then zero). The wavefront has its greatest curvature at the value  $z_m$  of  $z$ , given by:

$$\frac{1}{2} \frac{1}{z_m} \times w_{in}^2 = \frac{\lambda_0}{2\pi}. \tag{11}$$

The corresponding minimum radius of curvature,  $R_{min}$ , is given by:

$$\frac{1}{R_{min}} \times w_{in}^2 = \frac{\lambda_0}{2\pi}. \tag{12}$$

From equations (11) and (12) it also follows that  $R_{min}$  is equal to  $2z_m$ .

To characterize the Gaussian beams completely we need in addition to their radii of curvature their effective widths, of course. In the paraxial approximation these are given by:

$$w(z) = w_{in} \left\{ 1 + \left( \frac{\lambda_0 z}{\pi w_{in}^2} \right)^2 \right\}^{1/2}, \tag{13}$$

where  $w(z)$  is a dimension equal to half the effective width at the position  $z$  (again measured from the initial waist). The effective width is chosen so that along the  $z$ -axis it corresponds to four times the standard deviation of the local distribution of the irradiance. In mathematical terms, this local distribution is simply a normal probability distribution. It may be seen from eq. (13) that as they spread out in free space the Gaussian beams follow hyperbolic branches as boundary contours. The asymptotes intersect exactly at the centre of the initial waist, and their angle of inclination  $\frac{1}{2} \psi_{axis}$  to the optical axis — a kind of far-field value of half the beam divergence — satisfies the equation:

$$\frac{1}{2} w_{in} \times \tan \left( \frac{1}{2} \psi_{axis} \right) = \frac{\lambda_0}{2\pi}. \tag{14a}$$

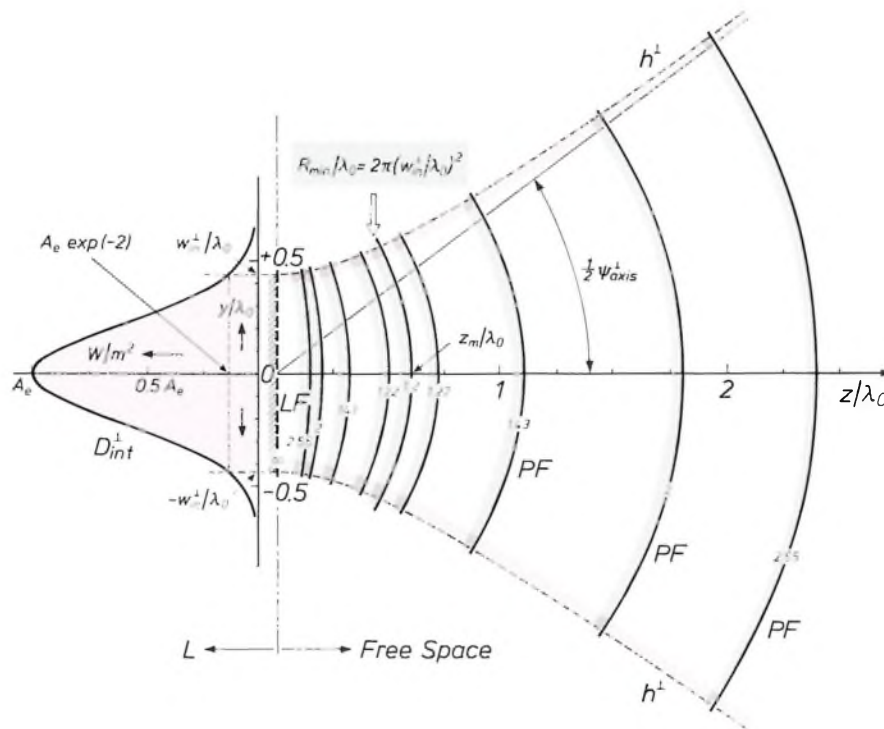


Fig. 5. Calculated example of a Gaussian beam emerging from a laser (L) and fanning out in free space. This situation exists just in front of the ball lens of a coupling element  $C_{1i}$  (fig. 3a). The circular arcs, considered to be in the vertical plane (some are marked PF) represent eight wavefronts. The radius of curvature is indicated on each wavefront in terms of  $\lambda_0$ , the laser wavelength: two wavefronts are shown for each curvature. The ninth wavefront, at the dimensionless coordinate  $z_m/\lambda_0 = 0.6$ , has the smallest possible radius of curvature ( $R_{min}$ ), determined by  $\lambda_0$  and  $w_{in}$ , half the width of the initial waist of the beam taken as an example, in the  $(y, z)$ -plane. The waist is located in LF, the partly transmitting end face of L; its radius of curvature is of course  $\infty$ . The corresponding normal distribution function  $D_{int}^1$  for the irradiance in LF is plotted against  $y/\lambda_0$ , the dimensionless vertical coordinate. The maximum value ( $A_e$ ) of  $D_{int}^1$  is found exactly at the origin (0) of the  $z$ -axis, the optical axis of the laser.  $h^1$  hyperbolic branches; at each point the intensity is equal to the local maximum (i.e. the maximum on the optical axis for the same  $z$ ) multiplied by  $\exp(-2)$ . These hyperbolic branches are widely used in practice for mathematically defining the boundaries of Gaussian beams — about 95% of the energy is contained within these boundaries. The laser parameters taken for this example are:  $\lambda_0 = 1.3 \mu\text{m}$  and  $w_{in}^1 = 0.568 \mu\text{m}$  (see also fig. 6).

Substituting eq. (11) in eq. (14a) we find:

$$\tan\left(\frac{1}{2}\psi_{\text{axis}}\right) = \frac{w_{\text{in}}}{z_m} \quad (14b)$$

If the astigmatism of the laser were negligible, the hyperbolic branches in fig. 5 could be considered as a longitudinal cross-section, in free space, of a complete hyperboloid with rotational symmetry.

The possible spread in the angle of inclination of the light rays, given by the angle  $\psi_{\text{axis}}$  in eq. (14a), and the possible spread in the spatial coordinate of the light rays, given by  $w_{\text{in}}$ , are related to one another in a way that makes eq. (14a) the analogue of a Heisenberg uncertainty relation. The wavelength  $\lambda_0$  then represents the analogue of Planck's constant.

$w_{\text{in}}^{\perp}$  in the vertical plane (red contour) and secondly for the beam from  $w_{\text{in}}^{\parallel}$  in the horizontal plane (blue contour, partly virtual). In minimizing the insertion losses the greatest difficulty here is not so much that  $w_{\text{in}}^{\perp}$  and  $w_{\text{in}}^{\parallel}$  are about an order of magnitude smaller than the characteristic spot parameter ( $w_0$ ) of the given fibre, but rather the reality that the laser beams are often strongly astigmatic ( $\Delta$ , in this case put at  $15 \mu\text{m}$ ). A lens that functioned theoretically in the best possible way would at least get rid of the astigmatism and could consequently have no rotational symmetry. To avoid fabrication difficulties (and ex-

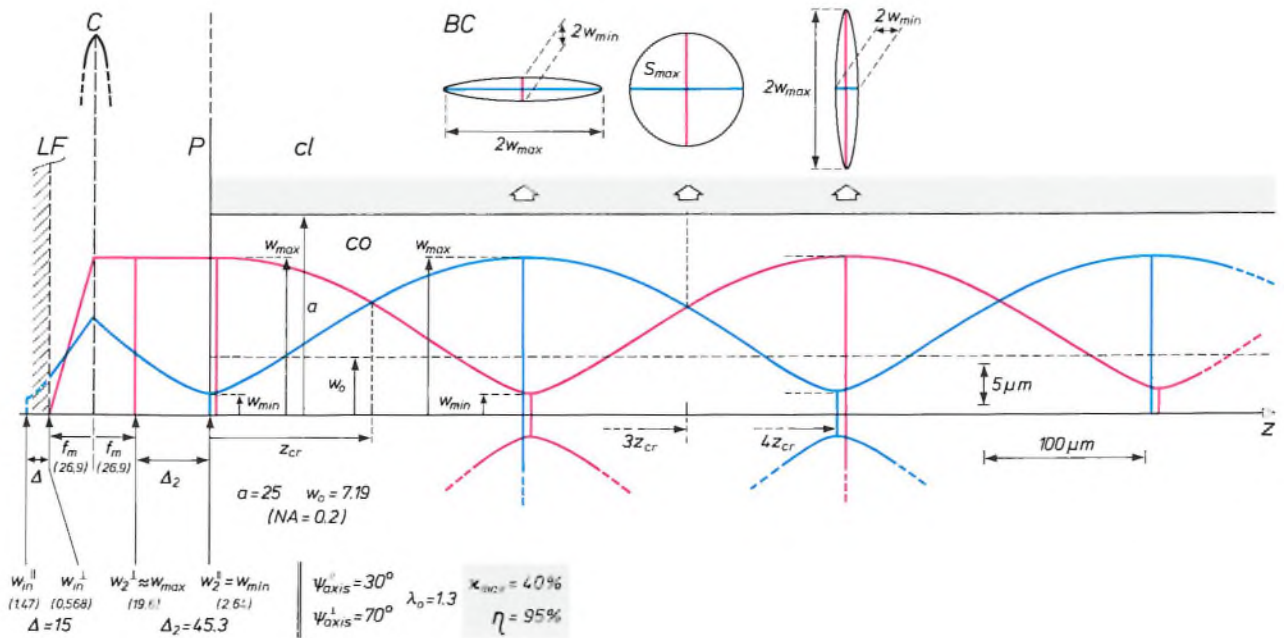


Fig. 6. Calculated example of an optimized optical interface with matching beam guidance along an optical axis ( $z$ ), obtained by the collimator action of a single lens ( $C$ ) and repetitive focusing in a fibre core ( $co$ ) of a pigtail ( $P$ ). The actual rays are *not* shown, but two bounding contours are shown in part (red: in the vertical plane, blue: in the horizontal plane). The rays are assumed to start from a real waist ( $w_{\text{in}}^{\perp}$ ) at the partly transmitting end face ( $LF$ ) of a laser, or a virtual waist ( $w_{\text{in}}^{\parallel}$ ) inside the laser. The wavelength ( $\lambda_0$ ) of the laser and its two beam divergence angles ( $\psi_{\text{axis}}^{\perp}$  and  $\psi_{\text{axis}}^{\parallel}$ ) are given; the two input waists can be calculated from equation (14a). The laser has an astigmatism ( $\Delta$ ) which is also shown.  $f_m$  focal length of  $C$ ,  $NA$ ,  $w_0$  characteristic parameters of the core. All quantities are expressed in  $\mu\text{m}$  (except  $NA$ , which is dimensionless). Particulars of the image waists ( $w_2^{\perp}$  and  $w_2^{\parallel}$ ), the astigmatism  $\Delta_2$ , the coordinate of position  $z_{\text{cr}}$  and the extremes ( $w_{\text{min}}$  and  $w_{\text{max}}$ ) will be found in the text. Three typical beam cross-sections in the fibre core (see also fig. 7).  $\eta$  maximum coupling efficiency, calculated ratio of the power of the guided beam, at the start inside  $co$ , to the power of the input beam on leaving the laser, as a percentage.  $\kappa_{\text{max}}$  calculated fraction of the power of the input beam that receives the fundamental mode in the core of the fibre as transfer medium, also as a percentage.  $cl$  cladding of the pigtail.

*The ball lens: strength and position of the coupling element*

The left-hand side of fig. 6 illustrates how an 'ideal', i.e. aberration-free, single lens ( $C$ ) in our communication system pinches a Gaussian beam fanning out from a waist (see fig. 5) to form a converging Gaussian beam. This correcting action of  $C$  has been calculated and depicted twice, first for the beam from the waist

(pense) we have confined ourselves to simple lenses, which do have such symmetry [14]. As already mentioned, beads of high-grade optical glass are satisfactory for this purpose; they need to have a diameter of only a fraction of a millimetre.

In the pinching of the Gaussian beams in the 'free space' beyond  $C$  the waists  $w_2^{\perp}$  and  $w_2^{\parallel}$  are formed; they can be considered to be the images of  $w_{\text{in}}^{\perp}$  and



$w_{in}^{\parallel}$ . These two images can be said to be 'ideal', since the field distributions on either side of  $C$  match one another perfectly, the reflection and absorption losses caused by  $C$  are negligible, and, as assumed, there are no aberrations. Of course, the astigmatism is still there, and consequently  $w_2^{\perp}$  and  $w_2^{\parallel}$  are spaced by  $\Delta_2$  instead of being coincident. After passing  $C$  the beam formed there brings all the rays contained in it, via the consecutive waists  $w_2^{\perp}$  and  $w_2^{\parallel}$ , into the fibre core ( $co$ ) 'matched as well as possible'. This matching requirement implies that the largest lateral cross-section of the radiation field within  $co$  should be minimized; this is done by making a suitable choice for the strength of  $C$  and its position. Particular attention is paid to finding the optimum position for the entrance plane of  $P$ , which should of course theoretically lie somewhere on the section of path ( $\Delta_2$ ) defined by the two waists  $w_2^{\perp}$  and  $w_2^{\parallel}$ .

At the centre of fig. 6 it can be seen how a continuous concentration of the optical energy along the axis ( $z$ ) is ensured by the alternate 'expansion and contraction' of the field in  $co$ . The photograph (fig. 7) shows a three-dimensional model of such a field, made in plastic on a numerically controlled lathe.

A guided field of this type — the resultant of all the modes excited in  $co$  — can always be based in a mathematical sense on the *spatially oscillating* contours (red and blue in fig. 6) of two planar Gaussian beams at right angles to one another. This is illustrated in fig. 6 by the beam cross-sections ( $BC$ ). The two elliptical cross-sections have the same area,  $\pi w_{max} \times w_{min}$ . This value is equal to the area of the characteristic spot,  $\pi w_0^2$ , a property which is connected with the self-focusing character of the parabolic medium [15]. The circular cross-section ( $S_{max}$ ), which occurs at the location of the points of intersection of the two contours, is the largest lateral section of the entire radiation field inside  $co$ . Calculations show that it is given by:

$$S_{max} = \frac{1}{2} \pi w_0^2 \left( \frac{w_{max}}{w_{min}} + \frac{w_{min}}{w_{max}} \right), \quad (15)$$

where  $w_{max}$  is half the maximum width of the two oscillating contours, and  $w_{min}$  is half the minimum width, again of the two contours.

The half-width,  $w^{\parallel}(z)$ , of the blue contour satisfies the equation [16]:

$$(w^{\parallel}(z))^2 = w_{min}^2 \cos^2 \left( \frac{\lambda_0 z}{\pi w_0^2} \right) + w_{max}^2 \sin^2 \left( \frac{\lambda_0 z}{\pi w_0^2} \right). \quad (16a)$$

The half-width,  $w^{\perp}(z)$ , of the red contour satisfies the equation:

$$(w^{\perp}(z))^2 = w_{max}^2 \cos^2 \left( \frac{\lambda_0 z}{\pi w_0^2} \right) + w_{min}^2 \sin^2 \left( \frac{\lambda_0 z}{\pi w_0^2} \right). \quad (16b)$$

In both equations the  $z$ -coordinate should be taken from the first extreme value inside the core. In the case of the blue contour that extreme value is the minimum 'exactly' at the front plane of  $co$ ; in the case of the red contour, on the other hand, it is the maximum that occurs at a finite distance, although negligible in practice (less than  $5 \mu\text{m}$ ), from that same front plane. Half-way between the first minimum and the first maximum of the blue contour is the first point of intersection of the two contours; its  $z$ -coordinate ( $z_{cr}$ ) is found to be equal to  $\frac{1}{4} \pi a / NA$ . The period of spatial oscillation for both contours, as can be seen from fig. 6, is equal to four times the distance  $z_{cr}$ .

The different rays that can exist, in terms of geometrical optics, within such oscillatory envelopes include 'straight' rays that follow the optical axis, and 'curved' rays that start at acute angles to the optical axis and then continually return to the axis to intersect the straight rays repeatedly, forming a row of regularly distributed image points along this axis ('repetitive focusing', characteristic of the guidance of rays by a parabolic refractive-index profile). In view of the formation of such a row of axial image points, the mean pro-



Fig. 7. Model of a stationary field distribution for a guided beam of rays inside a fibre core. The bounding surface of the field distribution is so defined that about 95% of the radiant energy is contained within it. In the direction of the optical axis it can be seen that the bounding surface has a row of maxima in both the vertical plane and the horizontal plane, and also on both sides (the maxima are the zones where the surface is furthest from the axis). Alternating with the maxima are minima — hence the guiding effect. The minima are barely visible in the photograph. The distance of the minima from the axis can however be estimated from the vertical ellipse at the front of the model. Half the minor axis of the ellipse is approximately equal to this minimum distance ( $w_{min}$  in fig. 6). Half the major axis of the ellipse is of course equal to the maximum distance ( $w_{max}$  in fig. 6). In this model the ratio  $w_{max}/w_{min}$  is about half the value of that used in fig. 6. Although there is this difference, the two ellipses in the group of three beam cross-sections shown in fig. 6 ( $BC$ ) can easily be traced in this photograph.

[14] A. J. A. Nicia, Loss analysis of laser-fiber coupling and fiber combiner, and its application to wavelength division multiplexing, *Appl. Opt.* 21, 4280-4289, 1982. See also: errata, *Appl. Opt.* 22, 1801, 1983.

[15] J. A. Arnaud, *Beam and fiber optics*, Academic Press, New York 1976.

pagation velocity along the axis must be the same for rays of both kinds. The equality of these two mean velocities is indeed made possible by the two principal properties of the core material: the rotational symmetry and the parabolic decrease of the refractive index in the radial direction (eq. 3). The curved rays, which are not shown in fig. 6, have a spatial variation that resembles the corresponding oscillatory envelope, with the restriction that the oscillation period of an envelope is exactly half that of an enclosed individual curved ray<sup>[15]</sup>.

Clearly, when the wavefronts pass through the ball lens ( $C$ ) their curvature changes more or less abruptly. The further development of these modified wavefronts determines the 'image waists' ( $w_2^\perp$  and  $w_2^\parallel$ ), as mentioned earlier, and in their turn these determine the  $w_{\max}$  and  $w_{\min}$  occurring inside the core ( $co$ ). One more parameter that plays a role, and is in principle variable, is the position of the front plane of  $co$ .

Calculations of this 'waist-on-waist' image formation have shown that the lens strength we are looking for has an upper limit,  $D_m$ <sup>[16]</sup>:

$$D_m = \frac{\lambda_0}{\pi} \text{minimum} \left( \frac{1}{w_{in}^\perp w_2^\perp}, \frac{1}{w_{in}^\parallel w_2^\parallel} \right). \quad (17)$$

With a stronger lens the image waists could no longer be correctly dimensioned, which would impair the coupling efficiency unnecessarily. The focal length of the ball lens must therefore be no smaller than  $f_m$  ( $\equiv 1/D_m$ ). The marginal value for the focal length,  $1/D_m$ , is a choice that is only just possible. The case illustrated in fig. 6 was in fact based on that choice.

There are three practical reasons for adopting this marginal coupling geometry. The marginal (i.e. minimum) value of the focal length goes with the smallest possible value for the spherical aberration of the ball lens, which is the first advantage<sup>[17]</sup>. Reducing the focal length obviously implies reducing the dimensions of the coupling element: the second advantage. The third advantage is that the alignment of the lens with respect to the laser is greatly simplified. The partly transmitting end face ( $LF$ ) of the laser should coincide with a focus; the lens is therefore displaced axially in such a way that the divergence of the beam in the vertical plane reaches a minimum well past the lens, as can easily be ascertained, at least before the pigtail ( $P$ ) has been mounted. A coupling geometry as shown in fig. 6, with an 'object waist' ( $LF$ ) at the focal point of the lens, might be called a 'collimator geometry' or, to be somewhat more exact (because of the astigmatism  $\Delta$  on the object side) a *semi-collimator geometry*. At this stage of the treatment, however,  $D_m$  cannot be derived from eq. (17) since the image waists ( $w_2^\perp$  and  $w_2^\parallel$ ) are as yet unknown.

It can be seen from eq. (15) that optimizing the coupling element certainly implies making  $S_{\max}$

smaller, because the field distribution will then become more concentrated around the axis. On referring to fig. 7 and eq. (15) it can be seen that to achieve maximum coupling efficiency — which corresponds to optimum matching — the largest beamwidth within the core ( $2w_{\max}$  in fig. 6) must have the same value in both the horizontal and vertical planes; this value must also be minimized. In other words, the circumscribed circle of the field distribution perpendicular to the  $z$ -axis must be as small as possible. For this double minimization two independent variables are required: the ones chosen are the strength of the ball lens  $C$  and the ratio of the line sections into which the transformed astigmatism  $\Delta_2$  is divided by the front plane of the pigtail ( $P$ ). (In fig. 6 this ratio has the marginal value 0, which is connected with the choice of the *marginal* variable,  $D_m$ , for the lens strength.)

The first result of the mathematical determination of the double minimization is that the best match with a coupling element with a semi-collimator geometry, as in fig. 6, will be obtained when the strength of the ball lens ( $C$ ) is equal to:

$$D_m = \left( \frac{\varepsilon}{\Delta} \frac{NA}{a} \right)^{1/2}, \quad (18)$$

where  $\varepsilon$  is the ellipticity ( $= w_{in}^\parallel/w_{in}^\perp$ , see fig. 4) of the laser.

The lens strength required is therefore, from equation (18), the geometric mean of two quantities, the first ( $\varepsilon/\Delta$ ) originating from the laser, the second ( $NA/a$ ) originating from the pigtail. The second result of the double minimization is the location of the front plane of  $P$  on  $\Delta_2$ .

The calculations show that the best distance ( $\delta s$ ) to the image waist  $w_2^\parallel$  is equal to:

$$\delta s = \left( \frac{\pi}{\lambda_0} \frac{w_{in}^\parallel w_{in}^\perp}{\Delta} \right)^2 \left\{ 1 - \left( \frac{\pi}{\lambda_0} \right)^2 \frac{(w_{in}^\parallel)^4}{\Delta^2} \right\} \Delta_2, \quad (19)$$

where  $\Delta_2$ , the astigmatism in the image space, is equal to:

$$\Delta_2 = \frac{a}{NA} \frac{w_{in}^\perp}{w_{in}^\parallel} \left\{ 1 - \frac{1}{2} \left( \frac{\pi}{\lambda_0} \right)^2 \frac{(w_{in}^\parallel)^4}{\Delta^2} \right\}. \quad (20)$$

The condition for the validity of equations (19) and (20) is that  $\pi^2 (w_{in}^\parallel)^4 / (\lambda_0 \Delta)^2 \ll 1$ . The relatively large value for the astigmatism  $\Delta$  in the laser explains why  $\delta s/\Delta_2$  remains negligibly small — about 0.016 in the example given in fig. 6.

The two image waists,  $w_2^\perp$  and  $w_2^\parallel$ , in the case of the semi-collimator geometry, are given by:

$$w_2^\perp \approx \frac{\lambda_0}{\pi} \left( \frac{a}{NA} \frac{\Delta}{w_{in}^\perp w_{in}^\parallel} \right)^{1/2}, \quad (21)$$

and

$$w_2^\parallel \approx \left( \frac{a}{NA} \frac{w_{in}^\perp w_{in}^\parallel}{\Delta} \right)^{1/2}. \quad (22)$$

Using eq. (5) we easily find from this pair of equations that:

$$w_2^\perp w_2^\parallel = w_0^2, \quad (23)$$

which is a further illustration of the attainment of (or better: good approximation to) the best possible match using the arrangement described for the interface zone between laser and pigtail.

In the case of the semi-collimator geometry it is found to be a good approximation to let the position of the front plane of the connecting pigtail coincide with the end of the transformed astigmatism in the image space of the lens — i.e. at  $w_2^\parallel$ . The magnitude of  $\Delta_2$  itself is immaterial since, of course, with the semi-collimator geometry  $w_{in}^\perp$  will be magnified much more than  $w_{in}^\parallel$ . (In the example of fig. 6 the magnifications are  $34\times$  and  $1.8\times$  respectively.) The beam divergence in the vertical plane is therefore almost zero (the red contour between C and P, fig. 6).

### Coupling efficiency

Further calculations on the double-minimization conditions mentioned in the previous section, at the coupling interface with the semi-collimator geometry (fig. 6), have enabled us to find the maximum possible efficiency ( $\kappa_{\max}$ ) for energy transfer via the fundamental mode. The expression found is <sup>[14][17]</sup>:

$$\kappa_{\max} = \frac{2}{1 + \frac{1}{2} \left\{ \left( \varepsilon + \frac{1}{\varepsilon} \right)^2 + b^2 \right\}^{1/2}}, \quad (24)$$

where  $\kappa_{\max}$  is the maximum ratio of the power in the guided beam that acquires the fundamental mode in the core as transfer field to the total power in the input beam (i.e. the total power emitted as a laser signal);  $\varepsilon$  is the ellipticity  $w_{in}^\parallel/w_{in}^\perp$ , as stated, of the laser. The astigmatism of the laser is accounted for here by the parameter  $b$ , with the astigmatism  $\Delta$  taken equal to  $(\pi/\lambda_0)w_{in}^\parallel w_{in}^\perp \times b$ . When the ellipticity has its smallest value (1) and if also the laser is 'ideal', with absolutely no astigmatism, the efficiency  $\kappa_{\max}$  will be exactly equal to 1 (or 100%), the maximum possible value for the coupling of one fundamental mode (that of the laser) to another. We note here that eq. (24) can also be used for estimating the maximum attainable efficiency for the coupling between a laser and a *single-mode* fibre.

To establish the *total* efficiency ( $\eta$  in fig. 6), characterizing the coupling interface, it is of course necessary to include in the calculation the amounts of power that are *not* transferred by the fundamental mode in the core but by the groups of bound modes of higher order. The desired expression for the best total coupling efficiency is:

$$\eta = \kappa_{\max} \{ 1 + (1 - \kappa_{\max}) + (1 - \kappa_{\max})^2 + \dots + (1 - \kappa_{\max})^{II-1} + (1 - \kappa_{\max})^{II} \}, \quad (25)$$

where  $\eta$  is the maximum possible ratio of the total power of the guided beam — at the start inside the core — to the total power of the input beam calculated as the beam leaves the laser. The quantity  $II$ , the highest exponent of the geometric progression in eq. (25), is the *number* of groups of bound modes. Taking into account the cut-off point for guided modes (eq. 9) and the fact that only the groups of modes for which the sum  $m + n + 1$  is *even* can be excited, we find for  $II$  as an integer the value (rounded downwards) of the expression  $\frac{1}{2} \{ (\pi/\lambda_0) a NA - 1 \}$ . From eq. (25) it is also easily shown that  $\eta$  will, at least theoretically, approach the maximum 1 (or 100%) when  $\kappa_{\max}$  itself approaches the value of 100% or when  $II$  is very large.

Modes for which  $m + n + 1$  is odd cannot be excited, essentially because of the occurrence of the Hermite polynomials. These polynomials are even or odd functions of the appropriate transverse coordinate, depending on whether the mode number is even or odd. The expression for a coupling coefficient <sup>[11]</sup> contains a product of two Hermite polynomials. For our system one polynomial cannot be other than  $H_0$ , i.e. equal to 1, since the laser emits its radiation only in the fundamental mode. Integration over the transverse coordinate from  $-\infty$  to  $+\infty$ , stemming from the requirement to match the two field distributions on either side of the 'coupling plane', gives zero for the coupling coefficient, unless the two polynomials in the product have the same parity. In the present case of the coupling to the laser the parity is thus *even*.

The equations (24) and (25) therefore make it possible for the designer to calculate the maximized coupling efficiency of such an optical interface, using the characteristic data of the laser and the pigtail as more or less free parameters.

The value of 95% calculated for  $\eta$  by way of example from eq. (25) as shown in fig. 6 is typical of the efficiency that the coupling elements  $C_{1i}$  (fig. 3a) should theoretically be able to attain if reflection and absorption are neglected. The values that can be obtained with coupling elements corresponding to our system are somewhat lower; as mentioned earlier, the practical values were found to be between 50 and 80%.

The efficiencies of the coupling elements  $C_{2i}$ , between the pigtails at the output of the optical section and the photodiodes, will certainly be no lower, because of the strongly pronounced local 'trumpet geometry' mentioned earlier (the 'characteristic diameter'

<sup>[16]</sup> See for example the book by D. Marcuse mentioned in [9] or H. Kogelnik and T. Li, Appl. Opt. 5, 1550-1567, 1966.

<sup>[17]</sup> A. J. A. Nijcia, Micro-optical devices for fiber communication, Thesis, Eindhoven 1983.

increases from 100  $\mu\text{m}$  to 300  $\mu\text{m}$ ; see fig. 3b). The value for  $\eta$  should really be 100%, apart from minor reflection losses, and a short piece of 'light-pipe' is an adequate coupling element. For the last of the four green blocks in fig. 3a no 'real' coupling lens is therefore necessary.

To obtain an estimate for the total coupling efficiency for the four interface zones in fig. 3a it is also necessary to take into account the two green blocks containing the multiplexing and demultiplexing units. Anticipating results in part II of the article, we should think here in terms of an efficiency of 50% for the multiplexing and demultiplexing units together. A reasonable estimate of the total coupling efficiency for the four interface zones in our system would therefore seem to be 25%, which corresponds to a loss of 6 dB.

Finally, we should note that the parameters of the pigtail in the calculation of  $\eta$  are expressed directly in the exponent  $\Pi$  alone. This once more emphasizes that the higher-order bound modes in the core can also make a very important contribution to the coupling efficiency.

The efficiency equations (24) and (25) have a wider validity than might perhaps be supposed from the marginal coupling geometry on which fig. 6 is based. As long as the lens strength remains below the upper limit indicated in eq. (17), the double minimization described always gives the same pair of expressions for  $\kappa_{\text{max}}$  and  $\eta$  as equations (24) and (25); the lens strength does not therefore appear as an explicit parameter in these equations. The reason for this is the assumption that the lens, as an 'ideal' coupling element, introduces no optical losses, i.e. no reflection or absorption losses. The required 'matching' of the electromagnetic field from the laser to the field that

can exist inside the fibre core — and the associated enlargement on imaging the initial waists — is apparently so simple an optical transformation that it does *not* uniquely determine the strength of the lens (which it does, however, once the interface zone has to meet geometrical requirements as well, as in the example in fig. 6).

The curves plotted in fig. 8 for constant  $\kappa_{\text{max}}$  values show how very much the astigmatism of the laser

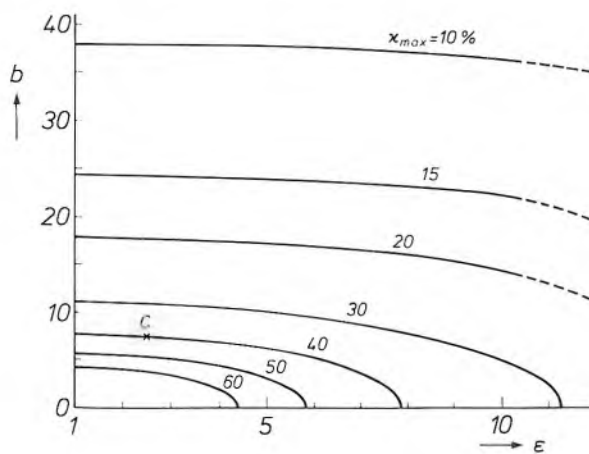


Fig. 8. Family of curves for  $\kappa_{\text{max}}$  values, in percentages, calculated from equation (24), with the ellipticity  $\epsilon$  and the astigmatism parameter  $b$  of the laser as dimensionless input variables. C the example from fig. 6 (the laser-fibre coupling with semi-collimator geometry).

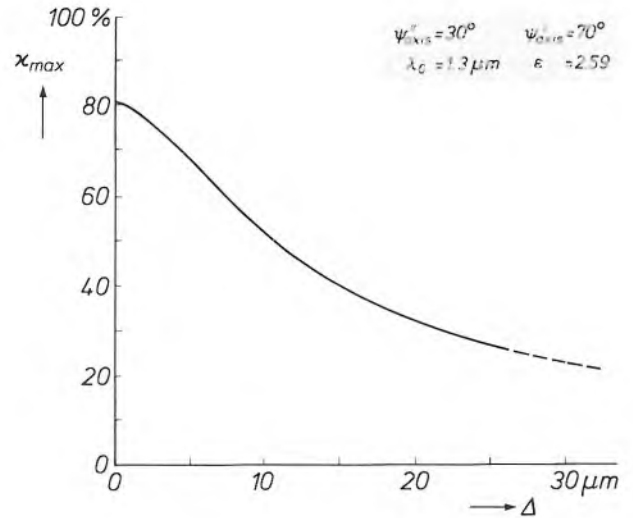


Fig. 9. The maximum coupling efficiency  $\kappa_{\text{max}}$  for power transfer to the fundamental mode in the fibre core, from equation (24). The independent variable  $\Delta$  is the astigmatism (in  $\mu\text{m}$ ) in the laser. The other laser parameters ( $\lambda_0$ ,  $\epsilon$ ,  $\psi_{\text{axis}}^{\parallel}$ ,  $\psi_{\text{axis}}^{\perp}$ ) are made equal to those of the laser used in the example in fig. 6.

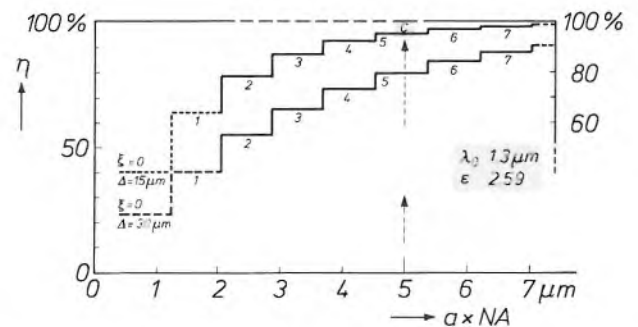


Fig. 10. Two calculated curves for the best total coupling efficiency  $\eta$ , in percentages, at optical interfaces via a coupling lens, from a laser to a pigtail, as given by equation (25). The independent variable is  $a \times NA$ , in  $\mu\text{m}$ , the product of the core radius and the maximum numerical aperture of the pigtail.  $\lambda_0$ ,  $\epsilon$ ,  $\Delta$  are the wavelength, ellipticity and astigmatism of the laser.  $\zeta$  positive integer, which identifies a group of higher-order modes (see text). The total coupling efficiency, as indicated by the stepped shape, is the sum of the contributions of the separate groups of guided modes. For the dashed part of the curves the theory used does not seem entirely adequate [14][17]. C the example from fig. 6 ( $a = 25 \mu\text{m}$ ,  $NA = 0.2$ ). If the contribution to  $\eta$  from a group of modes vanishes on reduction of the independent variable, the term cut-off is used, although that group is — and continues to be — excited.



weakens the coupling to the fundamental mode of the fibre core. The effect of the ellipticity seems relatively small, as appears from the rather horizontal nature of the curves. Mathematically, this behaviour is understandable, since the quantity  $\varepsilon + 1/\varepsilon$  in eq. (24) varies more slowly than  $b$ , the variable that represents the astigmatism.

Fig. 9 shows  $\kappa_{\max}$  as a function of the astigmatism for lasers that correspond in all other characteristics ( $\lambda_0$ ,  $\varepsilon$ ,  $\psi_{\text{axis}}^{\parallel}$ ,  $\psi_{\text{axis}}^{\perp}$ ) to the laser in fig. 6. An astigmatism of even only a few  $\mu\text{m}$  — which can also occur in some index-guiding lasers (fig. 4) — has a distinctly reducing effect on  $\kappa_{\max}$ .

Fig. 10, finally, illustrates the multimode nature of the guidance of the radiation. The independent variable plotted horizontally is the product of the radius of the core and its numerical aperture. The efficiency, as given by eq. (25), follows a rising 'staircase' curve. Whenever the product  $a \times NA$  exceeds a value of  $(\lambda_0/\pi)(2\xi + 1)$  when the curve is followed — where  $\xi$  is a positive integer — a group of modes of higher order 'join in', and consequently this accounts for a contribution of  $\kappa_{\max}(1 - \kappa_{\max})^{\xi}$  to the efficiency. If the astigmatism ( $\Delta$ ) of the laser were zero, then the

variation of  $a \times NA$  would have hardly any effect, since  $\eta$  would have been about 100% right from the start and the groups of higher-order modes would make no significant contribution to the total coupling efficiency.

**Summary.** A study of an optical communication system for digital or analog signals is described. Wavelength-division multiplexing is used with minimized insertion losses. The design provides for three to four channels in parallel operation in a multimode optical fibre (with a square-law core, radius 25  $\mu\text{m}$ , numerical aperture 0.2,  $\text{MHz} \times \text{km}$  product about 2000) in a second-generation cable for optical telecommunication. The light sources are diode lasers operating at wavelengths of 0.83  $\mu\text{m}$ , 0.87  $\mu\text{m}$ , 1.30  $\mu\text{m}$  and 1.55  $\mu\text{m}$ . The detectors are photodiodes of about 300  $\mu\text{m}$  diameter and a maximum rate of response of 500 MHz. The multiplexing and demultiplexing components are the main subject of part II of the article. Part I deals with the maximization of the total system efficiency. There are four interface zones, accounting for a total insertion loss of about 6 dB. The first interface (laser to fibre via a ball lens) is analysed using Hermitian-Gaussian modal field distributions. The astigmatism and ellipticity of the lasers, and the cut-off of the higher-order modes (because of the finite radius of the fibre core) are accounted for in the optimized efficiency equations. An astigmatism of only a few  $\mu\text{m}$  reduces the efficiency noticeably. The optimum strength and the location of the ball lens (between laser and fibre) are derived for the case of the semi-collimator geometry. The behaviour of two-dimensional Gaussian beams in free space and inside the core is also calculated.

## Beam manipulation with optical fibres in laser welding

At the Centre for Manufacturing Technology (CFT) in Eindhoven a method for beam manipulation in laser welding has been developed in which the laser beam is conducted from the laser to the workpiece by optical fibres. Before we look more closely at this new method, we shall first compare resistance spot-welding with laser spot-welding, and then we shall say something about the conventional method for beam manipulation.

For welding light metal components together in large numbers, considerable use is made of resistance spot-welding<sup>[1]</sup>. In this method the components are pressed together by two pointed electrodes, and then the material is heated by passing a current. Because of the higher contact resistance the heating effect is greatest at the places where the parts to be welded touch: the metal melts, and a strong weld results after cooling. A disadvantage of spot-welding is that the fairly large compression forces can cause distortion of the components. This can lead to complications, particularly in light components that have to be welded together very accurately. This is the case for example in assembling the electron guns for television picture tubes or the heads for tape-recording equipment.

A welding method that does not have this disadvantage is laser spot-welding. In this method the heating of the material is produced by a focused laser beam (we shall return to this later).

Laser welding has a number of advantages over resistance spot-welding:

- The components to be welded are not pressed together during the welding and therefore do not become distorted because of this.
- There is no need for welding electrodes, which wear very easily, so that far less maintenance is usually necessary, and the machine is out of action for much less time. (Welding electrodes can be used for about 5000 welds before they have to be replaced; a laser spot-welder can make about  $10^6$  welds without maintenance.)
- The quality of the weld is better than in resistance welding.
- The laser beam can reach places that welding electrodes cannot reach.
- The materials to be welded do not have to be electrically conducting. Laser welding does however have some disadvantages: the capital investment required is high, and the components have to be positioned accurately in relation to one another and to the laser beam.

For laser spot-welding an Nd:YAG laser is frequently used; this has a wavelength of  $1.06 \mu\text{m}$ . The emitted beam consists of light pulses whose energy content, pulse duration and repetition rate can be controlled. The pulses used generally have a duration from 3 to 10 ms and a repetition rate of up to 100 Hz. Their energy content is in the range 2 to 15 J.

For efficient mass production the way in which the laser beam is directed to the weld location is of great importance. The simplest solution is shown in *fig. 1a*. Here the laser beam is focused directly on to the workpiece by a lens. A small displacement of the focus (the weld point) can be obtained by moving the lens perpendicularly with respect to the beam; this possibility is indicated in *fig. 1a* by the dotted line. If more than one weld per workpiece is required, there are various possibilities. The workpiece can be displaced after each weld in such a way that the next weld can be made. This can however give a complicated arrangement — since there are six degrees of freedom for the movement. Moreover, the continual displacement of

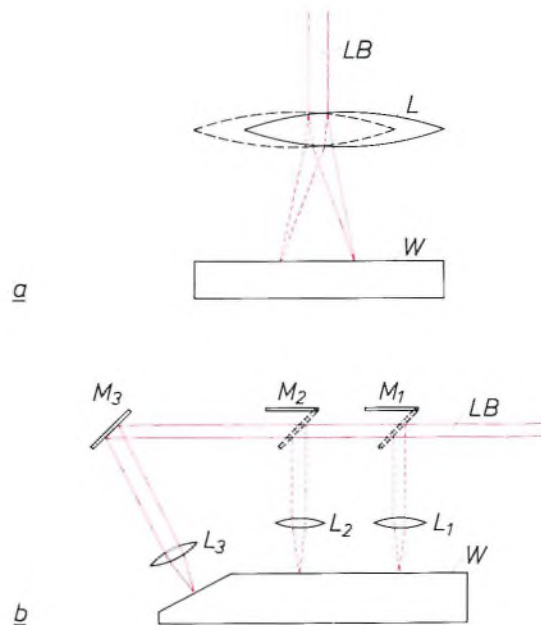


**Fig. 1.** Focusing the laser beam on to the workpiece. *a*) The simplest case. *LB* laser beam. *L* lens. *W* workpiece. A small displacement of the focus can be obtained by displacing the lens (dashed line). *b*) Making more than one weld on the workpiece. *M*<sub>1-3</sub> mirrors, which may be pivoted. The other symbols are as in *a*). This arrangement is not easily modified to suit another product, however.

<sup>[1]</sup> See for example pages 333-335 of R. L. Little, *Metalworking technology*, McGraw-Hill, New York 1977.

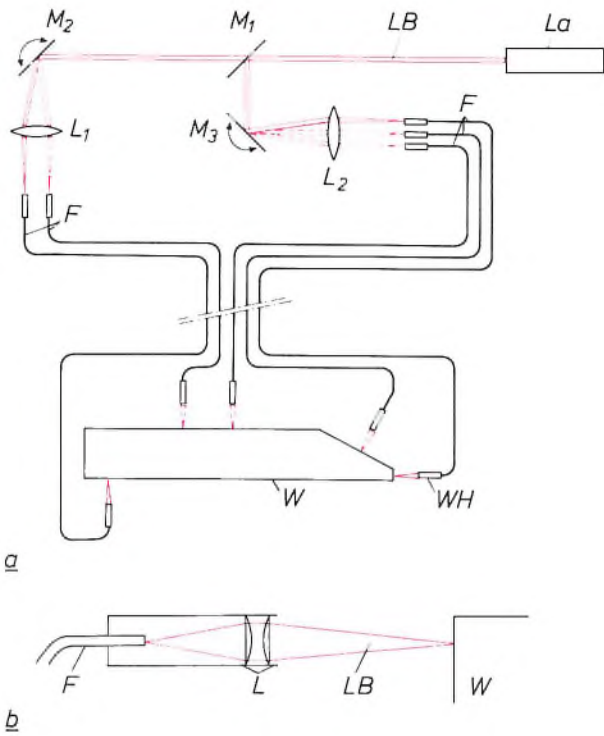


Fig. 2. a) Diagram of beam manipulation with optical fibres. *La* Nd:YAG laser. *M<sub>1</sub>* half-silvered mirror. *M<sub>2</sub>*, *M<sub>3</sub>* numerically controlled mirrors; in the case shown *M<sub>2</sub>* has 2 different positions and *M<sub>3</sub>* has 3. *L<sub>1</sub>*, *L<sub>2</sub>* lenses that focus the split laser beam on to the optical fibres *F*. *WH* welding heads attached to the optical fibres, to focus the laser beam on to the workpiece *W*. Because the fibres are flexible it is easy to reach the workpiece from all sides. b) Diagram of the welding head. The laser beam *LB* emitted from the fibre *F* is collimated by the pair of lenses *L* and focused on to the workpiece *W*.

the workpiece is rather time-consuming. Another solution is the installation of as many lasers as the number of welds that have to be made on each work-piece. This requires a very high capital investment, however. Another disadvantage of these two possible solutions is that the arrangement cannot be altered quickly for another product.

Another solution is to manipulate the laser beam in such a way that various weld locations on the work-piece can be reached with a single laser beam. It would for example be possible to use various combinations of pivoted or half-silvered mirrors (see fig. 1b). However, these arrangements are also not easy to alter to suit a new product.

At CFT work is now in progress on a better solution in which optical fibres are used. With the aid of numerically controlled mirrors and several lenses the laser beam is divided and focused on to a number of optical fibres; see fig. 2a. These optical fibres consist of a core of quartz glass (with a diameter of 600 μm) surrounded by cladding with a lower refractive index and a plastic protective coating. The laser beam can propagate along the core by total internal reflection at the cladding. In these optical fibres the laser beam can be transmitted over considerable distances (up to 100 m) with no significant losses. At the far end of each optical fibre there is a 'welding head' with a lens that focuses the beam emitted from the fibre on to the workpiece; see fig. 2b. The total optical losses amount

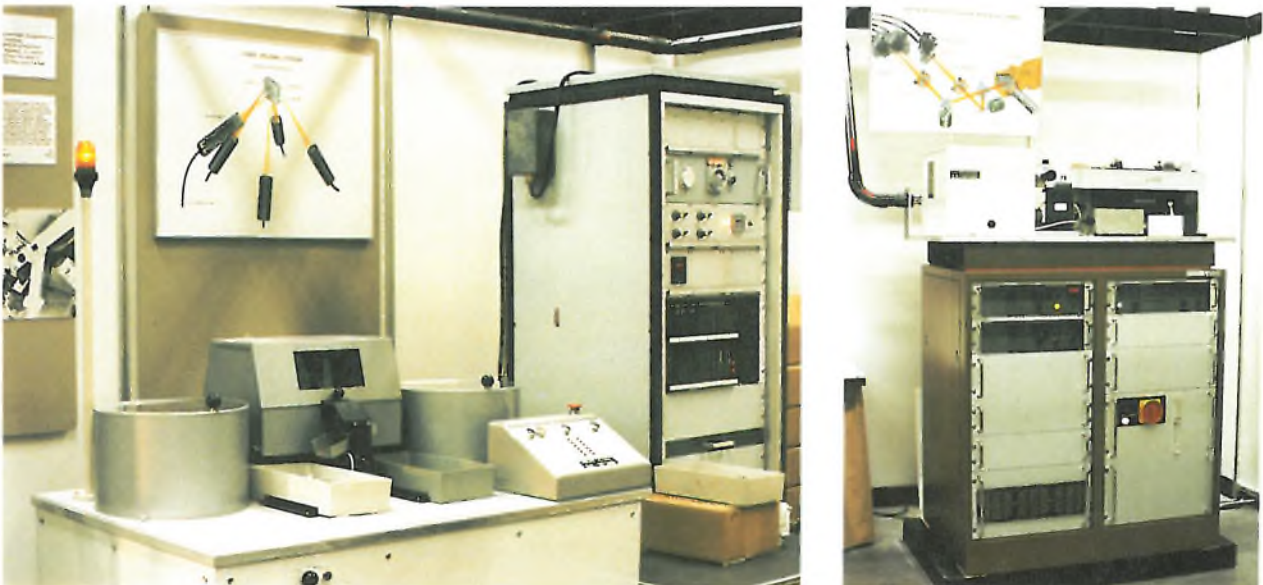


Fig. 3. Industrial version of a laser spot-welder. In the right-hand photograph there is a large cabinet for supply and cooling of the laser, which is on top of the cabinet. To the left of the laser there is a large white 'box' in which the beam is split and focused on to the optical fibres, which continue through the black tube on the left in the photograph. In the left-hand photograph the cabinet on the right contains the control electronics for the system. The welding takes place inside the approximately rectangular light-tight shield at the centre of the table. The cylinders on either side of the shield contain the feed mechanism and the working stock of components to be welded.



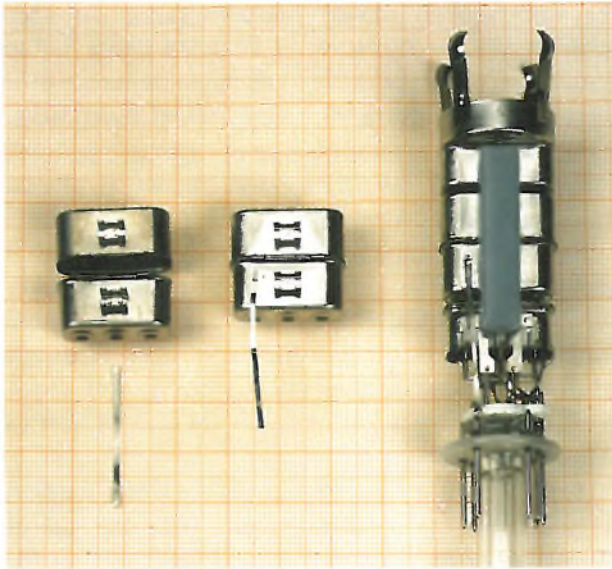


Fig. 4. A product made with the laser spot-welder. Left: two grids ('grids 3a and 3b') and a contact strip for a gun for a colour television picture tube. Centre: the two grids and the contact strip welded together by 5 spot-welds. Right: the complete gun, which contains about 80 spot-welds.

to about 15%; of this, 8% is accounted for by the input and output losses of the optical fibre (two glass/air interfaces). The remaining 7% of losses can be attributed to undesired reflections and absorption at the other optical components. Since the welding head is small (about 150 mm long, with a diameter of about 25 mm) and the optical fibres are long and flexible, the arrangement is very versatile and can easily be altered to suit new products.

Fig. 3 shows an industrial version of the welder, which is now set up in the Philips establishment at Sittard. In the right-hand photograph there is a large white 'box', in which the laser beam is split and distributed among the optical fibres, which continue through the black tube on the left in the photograph. The actual laser spot-welding takes place inside the approximately rectangular shield that can be seen at the centre of the table in the left-hand photograph.

An example of a product that has been made with the welder can be seen in fig. 4. On the left in the photograph are two grids (grids '3a' and '3b') and a contact strip for a gun for a colour television picture tube, which are welded together with the laser spot-welder (centre). On the right is the complete gun, which is assembled with about 80 spot-welds.

Laser spot-welding is a technology of increasing importance at Philips: at the moment there are more than 200 laser spot-welders in use and the number is still growing. More than ten of these machines employ the method described above for beam manipulation by means of optical fibres.

C. J. Nonhof  
G. J. A. M. Notenboom

*Dr C. J. Nonhof and Ing. G. J. A. M. Notenboom are with the Philips Centre for Manufacturing Technology (CFT), Eindhoven.*



# Philips Technical Review 50 years ago

## OPTICAL MODEL EXPERIMENTS FOR STUDYING THE ACOUSTICS OF THEATRES

FEBRUARY 1936

By R. VERMEULEN and J. DE BOER.

**Summary.** In the auditoriums of theatres where one of the primary considerations is the perfect audibility and intelligibility of the spoken word, a short period of reverberation is essential; this, however, should not cause too great a reduction in the "useful sound intensity". The distribution of loudness is examined in this paper with the aid of optical model experiments, in which the source of sound is replaced by a small lamp and the walls of the theatre simulated in a three-dimensional model by walls with a suitable coefficient of reflection. This method was applied on the occasion of the rebuilding of the assembly hall in Philips "Ontspanningsgebouw" (Philips Theatre).



Fig. 1. Models for examining the "useful" intensity of sound in a hall. The source of sound is represented by a small lamp, shown at the bottom of the photograph. The walls of the model are made of aluminium which reflects about 50 per cent of the light-rays falling on it, so that, in accordance with the definition of the "useful" intensity, a ray after only a few reflections can just contribute to the illumination of the opal glass representing the audience. (In the pictures this glass has been removed in order to show the interior; in the upper half of fig. 1b, however, the opal glass representing the seating on the balcony is visible. Sound-absorbing surfaces in the hall are blackened in the model, e.g. the right-hand wall in fig. 1b. The brightness of the opal glass (see figs. 4, 8 and 11) represents the distribution of the useful intensity of sound.

a) Model of hall of Philips "Ontspanningsgebouw" (Theatre) before reconstruction.  
b) Model of the same hall after reconstruction on the plans of Prof. Witzmann, Vienna.

## PRACTICAL APPLICATIONS OF X-RAYS FOR THE EXAMINATION OF MATERIALS

By W. G. BURGERS.

### 3. Quality Tests on Soapstone before Firing

Soapstone is a soft material which can be worked to exact dimensions. After suitable shaping it can be converted by firing (heating to about 1200 deg. C, during which about 6 per cent of water is given off) into a compact, hard and heat-resisting stone. During firing it frequently happens that certain places swell and as a result cracks appear which make the product useless. It is desirable to be able to detect and reject these pieces before firing, and as it appeared probable that the cracking was associated in some way with certain structural characteristics, examination by means of X-rays was indicated as offering a possible solution.

Fig. 1a shows a radiograph of that part of the raw material which did not swell on subsequent firing, while fig. 1b is a similar exposure of another part where swelling actually took place later.

An examination of these exposures reveals the same system of interference rings in both. But there is a fundamental difference in that the intensity distribution is uniform round the periphery of the rings in exposure 1a, but varying in 1b, where

certain intensity maxima appear round the circumference. This enables us to conclude that while there is no essential difference in composition at swelling and non-swelling places (identical systems of rings are obtained) there is yet a difference in texture: the places swelling on subsequent firing reveal that the crystallites favour a pronounced directional configuration (fibro-crystalline structure). Thus without entering into an analysis why this difference in structure causes a swelling during firing, we have evolved a method for testing the quality of soapstone before the firing process.

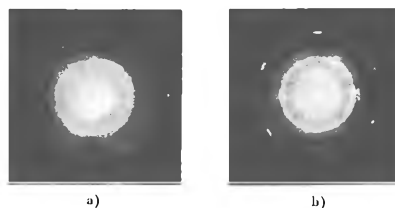


Fig. 1. Radiographs of steatite before firing: a) of a place which did not swell on subsequent firing, and b) of a place which later swelled on firing.



Fig. 4. Photograph of the opal glass in the model of the old hall (fig. 1a). The stage is on the right-hand side. The rapid diminution in illumination intensity towards the left may be noted; at the rear of the hall the useful sound intensity was far too small. The bright trapezoidal spot near the stage is due to reflection at the forepart of the ceiling which was not screened by the transverse roof trusses.



Fig. 8. Photograph of the opal glass in the model of the new hall (fig. 1b). The stage is again on the right-hand side. The distribution of illumination (useful sound intensity) is much more uniform than in fig. 4. The rear part of the hall under the balcony is still fairly dark (see fig. 11).



Fig. 11. Photograph of the opal glass in the model, as in fig. 8, but now with the rear wall under the balcony sloping slightly forward. The space under the balcony now also receives a satisfactory intensity of sound.

## SHORT NOTICE

### Brightness greater than on the sun

Brightnesses greater than those on the sun were recently produced in the Philips Laboratory by further increasing the wattage of the water-cooled super-high-pressure mercury vapour lamp described by Bol (De Ingenieur 50, E 91, 1935). Theoretical considerations of Elenbaas indicated that by reducing the diameter the brightness would be increased, and a lamp was therefore constructed with an internal diameter of 1 mm and an external diameter of 3 1/2 mm, which with electrodes 10 mm apart and an 805-volt alternating current took a load of 1400 watts. The luminous intensity with this load was 11,000 candle-power and the pressure about 200 atmos. Along the axis of the discharge the brightness was 1,160,000 candle-power per sq. in.; this was measured by passing a photo-electric cell with a small slit parallel to the axis of the discharge tube across an enlarged image of the lamp.

Seen from the earth, the brightness at the surface of the sun is only 1,065,000 candle-power per sq. in. (according to the International Critical Tables).

# The new centre for submicron IC technology

W. G. Gelling and F. Valster

---

*Taking part in the race to produce integrated circuits with diminishing details and expanding areas calls for enormous investment in people and buildings, not to mention computers and production equipment. People are necessary for their knowledge of processes such as plasma etching, chemical vapour deposition, implantation, oxidation and diffusion, and for combining these processes to produce patterns that form useful electronic circuits on a silicon slice. The equipment is necessary for projecting these patterns in minute detail on to the slice and creating the right conditions for the processes. Computers are needed for calculating and simulating the integrated circuits and for evaluating test data. Buildings are necessary to accommodate the people and hardware. In the new centre for submicron IC technology, now virtually completed at the Philips Research Laboratories site in Eindhoven, these buildings include areas where vibration and the dust content of the air are held to extremely low levels.*

---

## Introduction

In the sixties Philips brought out a hearing aid, for behind-the-ear wear, which contained an integrated circuit <sup>[1]</sup>. This IC consisted of an amplifier with three transistors. The 1-Mbit static RAM (RAM = random-access memory), which will go into pilot production in a few years in the new centre for IC submicron technology, will contain nearly ten million transistors. The hearing aid circuit was produced on a silicon chip with an area of about 0.6 mm<sup>2</sup>, the static RAM will be produced on an area of about 90 mm<sup>2</sup>. The old circuit was used for processing analog information, the new one will be used for storing immense amounts of digital information. These two examples typify the developments in electronics: integrated circuits are growing and contain more and more functions, the area required for each function continues to decrease, and digital technology is becoming firmly established.

If we look at the developments in the IC industry over a number of years, we see that the manufacturing cost per electronic function has decreased by a factor of ten in every five or six years. And this trend appears to be continuing. So it is more than likely that the number of applications of electronics in our daily life will continue to increase. We have digital electronics

very much in mind here. The digitization of audio and video equipment, for example, is already under way, and the computer in all its manifestations will occupy an increasingly important place.

Keeping up with all of these developments requires much effort from a company such as ours. To meet this challenge, Philips decided to build a new centre for IC technology at the Research Laboratories site in Eindhoven. In this centre staff from the research laboratories will cooperate closely with development engineers from the Elcoma division, who are the producers of integrated circuits in the Philips group.

The new IC centre will mainly be housed in two buildings; see *fig. 1* and *2*. In one building there will be research and development on submicron technology — the technology that will give us integrated circuits with details smaller than 1 μm. This building will also contain the pilot production of advanced ICs before the Elcoma division take over the technology and start to manufacture the circuits. The design of this building is very largely determined by the requirements for dust-free production and insensitivity to vibration — vital conditions for the manufacture of high-technology integrated circuits. In the other building, now completed, the electronic circuits are designed. The layout of this building is mainly determined by the

---

*Drs W. G. Gelling is a Deputy Director and Ir F. Valster a Director of Philips Research Laboratories, Eindhoven.*



**Fig. 1.** The building for submicron-technology research and development at the new IC centre. This is where advanced ICs will go into pilot production.

large computers and the test equipment it will have to accommodate: advanced ICs can only be designed and simulated with the help of computers (CAD, or Computer-Aided Design). For example, the computers in use at the moment require about ten hours to calculate how a large IC will respond to a signal at the input; the computers to be installed in the new building will perform calculations of this type in less than an hour.

The mastery of modern IC technology can be assessed by the ability to produce large memory circuits with a high yield. The largest integrated circuits now being made are RAMs. Since 1971, when the first IC memory with a capacity of 1 kbit ( $2^{10} = 1024 \approx 10^3$  bit) was introduced, the capacity per IC has increased roughly sixfold every five years. Philips, for example, are well on the way with the design of a static RAM with a capacity of 256 kbit; see *fig. 3*. Philips plan to start pilot production of this memory, on 6-inch silicon slices, at the new centre in about a year. Samples

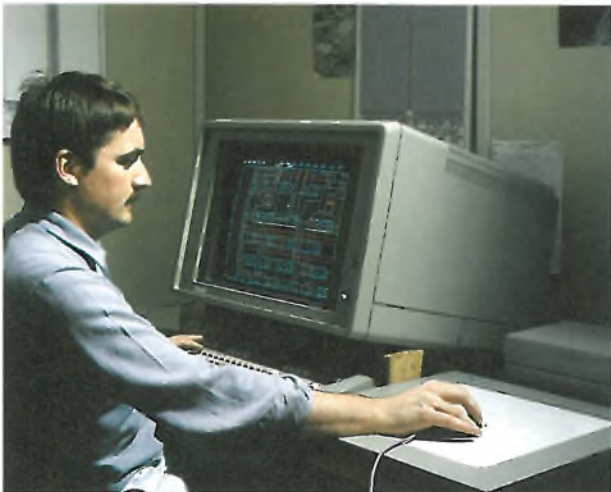


**Fig. 3.** CAD of the static-RAM semiconductor memory with a capacity of 256 kbit, which Philips will put into pilot production in about a year's time.



**Fig. 2.** The building where the circuits will be designed with the help of computers (CAD, Computer-Aided Design).

of a 1-Mbit static RAM will be available in 1988. (1 Mbit =  $2^{20} = 1\,048\,576 \approx 10^6$  bits.)

The 1-Mbit memory will be made in CMOS technology, and the individual transistors will have a channel length of  $0.7\ \mu\text{m}$ . The extremely detailed patterns required for these circuits will be projected on the silicon slice by photolithography. For this work a new high-resolution wafer stepper (or repeater projector) will be developed as a successor to the well-known Silicon Repeater [2]. The submicron technology required for manufacturing the static 1-Mbit memory will be used later for a wide variety of other types of integrated circuit. The advanced memory will thus act as the 'locomotive' that will provide the motive power for other Philips IC technology in the coming years.

In the following pages we shall explain why CMOS technology, photolithography and a static RAM have been chosen for the new centre. We shall also look at some of the technical aspects of the new buildings.

## IC technology

### CMOS

Large digital ICs are now more and more likely to be made in MOS technology (MOS: metal-oxide semiconductor). Bipolar technology is mainly used in analog circuits and in high-speed digital circuits. Bipolar ICs are built up from npn transistors and in many cases pnp transistors. Bipolar transistors derive their name from the fact that both electrons and holes contribute to the conduction. In MOS transistors, on the other hand, the conduction is due to the transport

[1] B. de Boer, Behind-the-ear hearing aids, Philips Tech. Rev. 27, 258-263, 1966.

[2] A. G. Bouwer, G. Bouwhuis, H. F. van Heek and S. Wittekoek, The Silicon Repeater, Philips Tech. Rev. 37, 330-333, 1977;  
S. Wittekoek, Optical aspects of the Silicon Repeater, Philips Tech. Rev. 41, 268-278, 1983/84.

of holes or electrons: there is only one type of charge carrier.

The operation of a MOS transistor is based on the capacitive coupling of a conductor (the 'gate') to a p-doped or n-doped semiconducting material via a thin insulating oxide layer. A silicon NMOS transistor (on the left in *fig. 4*) contains two islands of heavily doped n-type silicon in a p-type silicon substrate. The two islands are called the source and drain respectively. The transistor operation is based on the conduction of electrons in the p-type silicon. These electrons are drawn from the source by a positive voltage on the gate to a thin layer of the p-type silicon (the 'channel') immediately below the insulating oxide. The gate may consist of metal or of heavily doped polycrystalline silicon. In a PMOS transistor (on the right in *fig. 4*) the source and drain take the form of islands of heavily doped p-type silicon in a larger island of n-type silicon. In this type of transistor a negative voltage on the gate produces hole conduction at the surface of the n-type silicon. The operation briefly described above applies to PMOS and NMOS transistors of the enhancement type. Transistors of the depletion type, on the other hand, conduct when there is no voltage applied to the gate.

In CMOS technology (CMOS: complementary metal-oxide semiconductor) PMOS and NMOS transistors are combined. As an example a diagram of a logic inverter made in CMOS technology is shown in *fig. 4*. With a positive supply voltage the output voltage  $V_o$  is 0 when there is a positive input voltage  $V_i$ . If on the other hand  $V_i$  is 0, then  $V_o$  is equal to the supply voltage. As we shall presently see, similar transistor combinations are also found in static RAMs.

Compared with bipolar transistors, MOS transistors have a simple structure and make ideal switches. Another advantage is that simpler techniques are ade-

quate for insulating MOS transistors from each other. The 'packing density' of MOS ICs is therefore about four times that of bipolar ICs. This high packing density and their operation as switches make MOS transistors particularly suitable for large digital integrated circuits. The first MOS circuits were produced in PMOS technology. It was the introduction of ion implantation in IC manufacture that made circuits in NMOS technology a possibility. ICs in NMOS technology are faster than those in PMOS technology, because electrons have a higher mobility than holes.

Raising the packing density in integrated circuits has increased the problem of heat removal. It is therefore a considerable advantage that the heat dissipation of ICs in CMOS technology is low. This is because the elements of logic circuits and memories in CMOS technology only conduct when there is a change in the information content of a switching element. The only currents flowing in the circuit in *fig. 4*, for example, in the steady state are the leakage current of the non-conducting transistor and the leakage currents in the reverse-biased p-n junctions. A disadvantage of CMOS technology is that the packing density is lower than in PMOS or NMOS technology, since n-type silicon islands are required. The problem of the lower packing density can be compensated to a considerable extent by ingenious design.

The level of 'sophistication' of the technology used to produce an integrated circuit can be characterized by the channel length ( $l$  in *fig. 4*). In recent years this parameter has been dramatically reduced, and in the static 256-kbit memory we mentioned it is 1.2  $\mu\text{m}$ . The transistors to be made in the new centre for IC submicron technology will have a channel length of 0.7  $\mu\text{m}$ . This sharp reduction in scale will create new problems, of course, and we shall look at some of them here.

To produce a smaller MOS transistor with a useful characteristic it is necessary to satisfy certain rules for scaling. A smaller channel area, the product of the length and width of the channel, implies that the thickness of the channel oxide must also be proportionately smaller. At the same time, the implantation dose of boron or arsenic must be larger to achieve the required threshold voltage. The diffusion depth must also be proportionately smaller if the lateral source and drain diffusion is to be limited during the diffusion of boron or arsenic at high temperature. Shallow diffusion, however, increases the resistances in the transistor, and this can reduce its speed of response.

The dimensions can also be scaled down by means of 'three-dimensional' cell structures. Research in the new centre will therefore include work on techniques such as the 'stacking' of elements and the fabrication

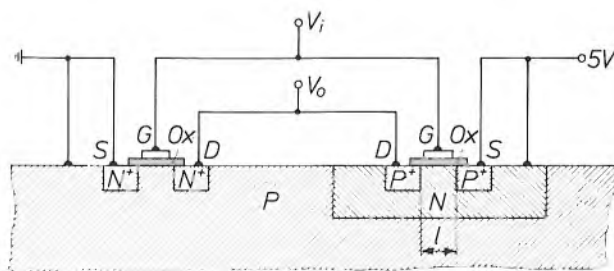


**Fig. 4.** Principle of a logic inverter in CMOS technology. An NMOS transistor is shown on the left, a PMOS transistor on the right. The supply voltage is 5 V.  $V_i$  input voltage.  $V_o$  output voltage. S source. D drain. G gate. Ox insulating layer of  $\text{SiO}_2$  (channel oxide). P silicon with a surplus of free holes. P<sup>+</sup> silicon with an extra surplus of free holes. N silicon with a surplus of free electrons. N<sup>+</sup> silicon with an extra surplus of free electrons.  $l$  channel length.



of 'vertical' structures in a groove in the slice. This introduces the additional difficulty of restoring the surface flatness of the slices during the production.

With smaller details it is obvious that the alignment should be more accurate and the resolution better when the mask patterns are projected on the slice. The accuracy of the application and partial removal of the various layers must also be improved. These are problems of lithography, and we shall now consider them more closely.

### Lithography

It might seem obvious that X-ray lithography or electron lithography would be used in the new IC centre. It has been decided, however, to use photolithography, although this does not exclude the possibility of other techniques in the future, and there is research on new lithographic techniques in Philips laboratories [3][4].

X-ray and electron lithography have the advantage of a higher resolution because the radiation has a shorter wavelength (0.5 to 3 nm for X-rays, 0.05 nm for electron lithography and about 400 nm for photolithography). The disadvantage of X-ray lithography is that the masks are as yet very difficult to produce and it is necessary to use synchrotron radiation [4]. At present the large and expensive storage ring that is required as an X-ray source is not suitable for use in an IC factory. The disadvantage of electron lithography is that it takes a long time to write a pattern — about an hour for a complete 6-inch silicon slice. Although a more ingenious method of scanning the pattern saves time, the method would still not be economic even if the scanning duration were reduced by a factor of ten (if such a reduction were possible). Electron-optical pattern generators are however used for producing accurate masks for photolithography.

The wafer stepper that was developed at Philips Research Laboratories (the Silicon Repeater [2]) has a highly refined alignment system, with a sensitivity of 0.02  $\mu\text{m}$ , which makes it suitable in principle for sub-

micron technology. It is necessary, however, to improve the resolution of the projection optics, and a new optical system is therefore now being developed in cooperation with a specialist manufacturer.

The etching operations following exposure in the repeater projector in the new IC centre will in general be 'dry'. With conventional wet-etching techniques the highly detailed patterns cannot be transferred with the required accuracy and not all materials can be etched. The dry-etching techniques of plasma etching and (reactive) ion etching are less subject to these difficulties [5].

### Memory circuits

As noted earlier, semiconductor memories may be regarded as the 'locomotive' of submicron IC technology, since the most advanced techniques are required in order to accommodate as many memory cells as possible in unit area. With good test procedures faults can be traced and localized very accurately in many cases. Minute examination of the faults then provides the vital clues that enable the technology to be improved. Logic circuits are not very suitable for our 'locomotive' function here, since it is much more difficult to localize the faults in a logic circuit. Memories are thus an important link in the learning process for an optimum mastery of IC technology, whether in research and development or in actual production. In turn, mastering the technology of standardized memories generates the skills required for the economic manufacture of other types of custom-made integrated circuit.

Semiconductor memories fall into various categories. Research on the applications of analog and digital CCD memories (CCD: charge-coupled device) has long been in progress at Philips [6]. Memories of this type work serially, on the shift-register principle, and the individual memory cells do not have addresses. The cells in ROM and RAM memories (ROM: read-only memory, RAM: random-access memory) do have addresses. A ROM can only be read. The contents are fixed and have already been entered into it during manufacture. A RAM can be 'read from' and 'written to', so that its contents can be changed.

RAMs are 'volatile' memories: the information is lost if the supply voltage fails. RAMs can be subdivided into dynamic and static types. A cell of a dynamic RAM consists in principle of a capacitor and a transistor; see *fig. 5a*. The gate of the transistor is connected to the 'word line' (for addressing the rows of the memory matrix) and the source is connected to the 'bit line' (for addressing the columns). The capacitor of a memory cell is charged by applying a relatively high voltage to the word line and bit line correspon-

[3] J. P. Beasley and D. G. Squire, Electron-beam pattern generator, Philips Tech. Rev. 37, 334-346, 1977;

J. P. Scott, Electron-image projector, Philips Tech. Rev. 37, 347-356, 1977.

[4] H. Lüthje, X-ray lithography for VLSI, Philips Tech. Rev. 41, 150-163, 1983/84.

[5] H. Dimigen and H. Lüthje, An investigation of ion etching, Philips Tech. Rev. 35, 199-208, 1975;

H. Kalter and E. P. G. T. van de Ven, Plasma etching in IC technology, Philips Tech. Rev. 38, 200-210, 1978/79.

[6] H. Heyns, H. L. Peek and J. G. van Santen, Image sensor with resistive electrodes, Philips Tech. Rev. 37, 303-311, 1977;

H. Dollekamp, L. J. M. Esser and H. de Jong, P<sup>2</sup>CCD in 60 MHz oscilloscope with digital image storage, Philips Tech. Rev. 40, 55-68, 1982;

H. J. M. Veendrick *et al.*, A 40 MHz 308 Kb CCD video memory, Proc. ISSCC 84, San Francisco 1984, pp. 206-207.

A forthcoming article in this journal will deal with a new CCD image sensor.



ding to the address of the cell. The charge of the capacitor slowly leaks away to earth. The contents of the cell must therefore be 'refreshed' periodically, (e.g. every 2 ms), by supplying sufficient charge to restore the voltage to its original value. A disadvantage of a dynamic RAM is therefore that it requires extra elec-

tors are required to connect the cell to the two bit lines in this case; see fig. 5*b*. The word line is connected to the gates of these coupling transistors, and each bit line is connected to a source. The contents of a cell are changed by applying the higher voltage to a bit line and the word line, and the lower voltage to the other

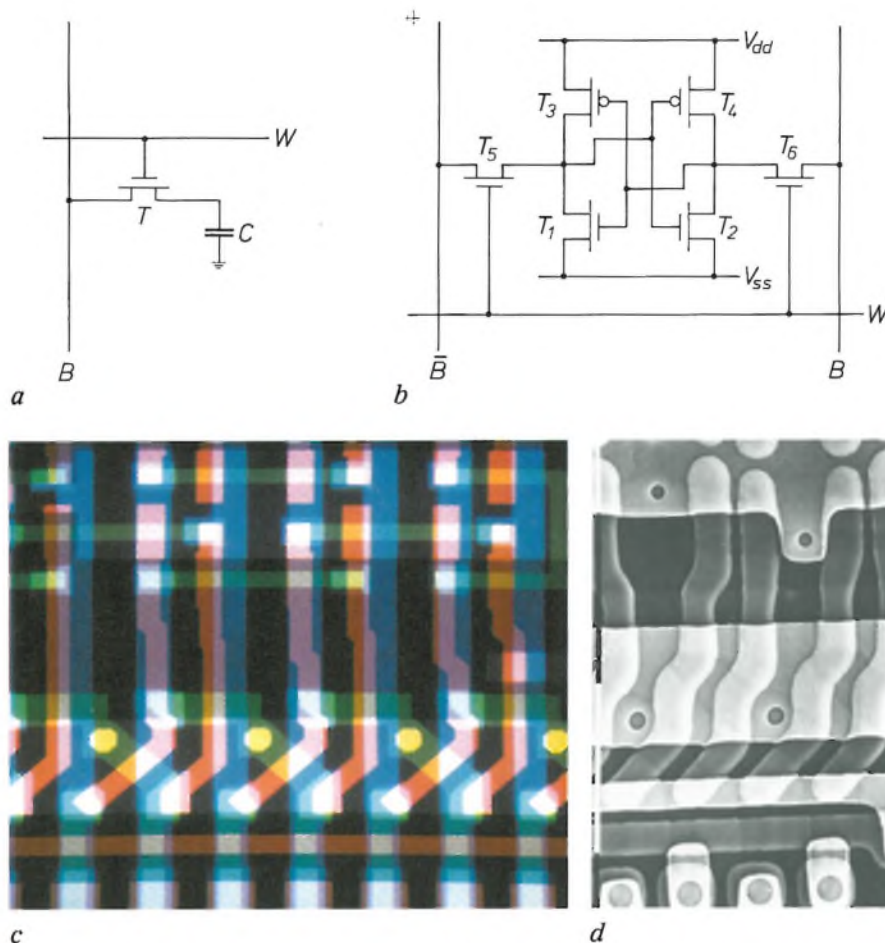


**Fig. 5.** *a*) Diagram of a cell in a dynamic RAM. *T* MOS transistor. *W* word line. *B* bit line. *C* capacitor. *b*) Diagram of a cell in a static RAM. *T*<sub>1-4</sub> MOS transistors that form a flip-flop. (The upper two transistors are PMOS transistors, the lower two are NMOS transistors.) *T*<sub>5,6</sub> coupling transistors.  $\bar{B}$  inverse bit line. *V*<sub>dd</sub> voltage on drain electrodes. *V*<sub>ss</sub> voltage on source electrodes. *c*) Photograph of some memory cells on the graphic display during CAD of the 256-kbit SRAM; see also fig. 3. The various coloured areas represent masks used in the fabrication process. For clarity not all of the masks have been shown. The vertical blue stripes are bit lines (*B* and  $\bar{B}$  in *b*); the horizontal red stripe is a word line (*W* in *b*). *d*) Scanning electron micrograph of a few cells from a very similar memory at an intermediate stage of the fabrication process: the first metal conductor lines have been applied, but not the bit lines. One 'dash' on the scale on the left corresponds to 10  $\mu\text{m}$  on the slice. The minimum pitch of the lines is 2.6  $\mu\text{m}$ . The linewidth is 1.2  $\mu\text{m}$ . The actual lines are obscured by layers above them, so that the lines seem to be wider. The circular patterns at the bottom of the picture correspond to the squares that can be seen at the bottom of the screen in (*c*). These patterns are the bit-line contacts on the extreme left and right in (*b*).

tronics for the refresh operation and that the contents of the memory are not available during this operation. An advantage is that a dynamic-RAM cell takes up extremely little space.

A memory cell of a static RAM needs much more space, because each cell consists of a flip-flop with four transistors. Furthermore, two additional transis-

bit line. Designing the four transistors in pairs as NMOS and PMOS types in CMOS technology considerably reduces the dissipation of a cell. Cells of the 256-kbit SRAM mentioned earlier are shown in figs 5*c* and *d*.

The 256-kbit SRAM is provided with spare memory cells (future memories will be similarly equipped). If

faults are found in one or more cells, they can be disconnected. This is done by interrupting conductor lines with a focused laser beam. Some of the spare cells then take over the function of the failed cells. This is done by interrupting lines to the gates of depletion-type transistors, so that these transistors then conduct.

A memory cell of a dynamic RAM takes up about a quarter of the space occupied by a cell of a static RAM. However, the control electronics of a static RAM occupies far less space and the stored information is continuously available at all times. Because of their specific advantages and disadvantages, both types of memory have their preferred areas of application. As we mentioned earlier, Philips will devote a substantial part of the effort in the new IC centre to the development of a 1-Mbit SRAM. In terms of packing density a 1-Mbit SRAM is comparable with a 4-Mbit DRAM.

#### Some technical aspects of the buildings

As more and more transistors of ever smaller dimensions are accommodated on a chip, the chance of an error occurring in any transistor will have to diminish correspondingly. Otherwise the probability of a fault-free circuit will become so small that a satisfactory production yield will no longer be possible. It is found that dust is one of the most common causes of faults. One of the principal requirements to be met by the processing rooms in the submicron-technology building (fig. 1) is therefore an extremely low dust content in the air.

Fig. 6 is a diagram showing the connection between the number of bits of a dynamic RAM, the width of the lines in it and the required minimum dust concentration in the air as specified by extrapolation of the American Federal Standard 209B<sup>[7]</sup>. In this standard the highest degree of cleanliness is referred to as class 100. In a class-100 clean room the air must contain no more than 3500 particles of 0.5  $\mu\text{m}$  diameter or larger per  $\text{m}^3$  (100 such particles per cubic foot). The corresponding line in the figure relates to cumulative values for other particle sizes. It is now normal practice to extrapolate standards for classes 10 and 1 from this standard; lines for these classes are also shown in the figure. These degrees of cleanliness will probably be standardized as well. With the initial assumption that

particles whose diameter is 10% of the linewidth will not cause chip rejects, it is further assumed that for manufacture of 64-kbit DRAMs the air must be cleaner than air of class 10. For 256-kbit DRAMs the air cleanliness should be class 1; see fig. 6.

As mentioned earlier, the new 1-Mbit SRAM has a packing density comparable to that of a 4-Mbit DRAM. Further extrapolation of Federal Standard 209B shows that the air in the clean room for fabricating memories of this type must contain no more than 350 particles of 0.1  $\mu\text{m}$  diameter or larger per  $\text{m}^3$  (10 per cubic foot). This is a much more difficult require-

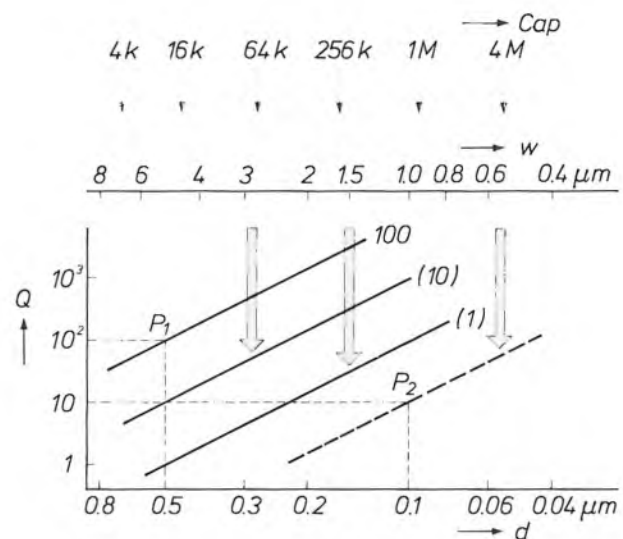


Fig. 6. The connection between the detail of a memory circuit and the required degree of cleanliness of the air<sup>[7]</sup>. Cap number of bits of dynamic RAMs.  $w$  corresponding linewidth.  $d$  diameter of dust particles.  $Q$  number of particles permitted in American Federal Standard 209B, per cubic foot and with diameter  $d$  or larger. The number 100 on the upper line (based on the coordinates of the point  $P_1$ ) gives the class of air cleanliness defined in this standard. The other lines (numbers in brackets) correspond to an extrapolation of this standard. The dashed line gives the degree of cleanliness (based on the coordinates of the point  $P_2$ ) for the cleanest process tunnels in the new technology building. The arrows indicate the connection between linewidth and maximum particle size.

ment than those conventionally used in IC manufacturing centres. It can only be met by installing very large and expensive air-treatment plants and by the personnel following the strictest 'cleanliness discipline'.

Only 7% of the total volume of the building is taken up by the space used for the actual manufacturing. This consists of a number of adjacent 'tunnels' for the various stages of the process. 'Superclean' tunnels, which meet the cleanliness requirement specified above, alternate with tunnels that are relatively less clean. The superclean tunnels are designed for the

<sup>[7]</sup> R. P. Donovan, B. R. Locke, D. S. Ensor and C. M. Osburn, The case for incorporating condensation nuclei counters into a standard for air quality, *Microcontamination* 2, No. 6 (December), 39-44, 1984; K. Takahashi and K. Yagi, Development of clean tunnels for semiconductor manufacturing, *Proc. 6th Int. Symp. on Contamination control*, Tokyo 1982, pp. 165-168.

actual processes. The less-clean tunnels contain equipment requiring regular maintenance. For example, the ion-implantation equipment will be accommodated in a less-clean tunnel that opens into a superclean tunnel. To avoid manipulations with bottles or containers in the superclean tunnels, all liquids and gases are transported along pipelines. Containers for liquids and gases are kept in separate compartments on the outside of the building. Alongside the actual technology

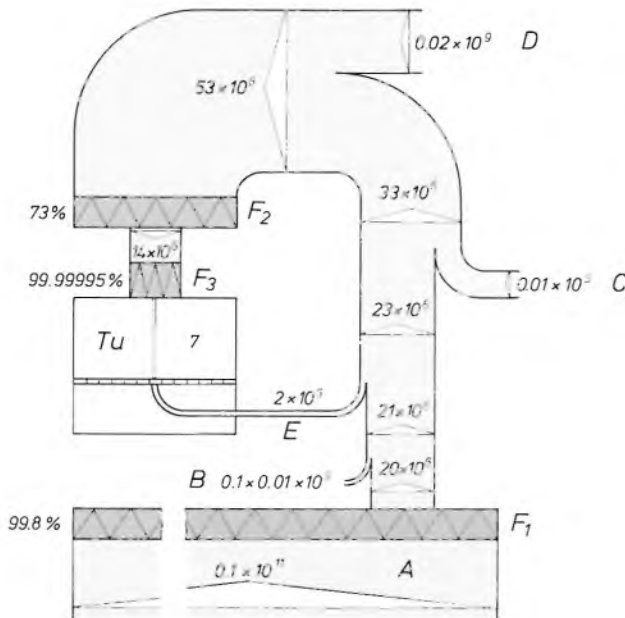


Fig. 7. Sankey flow diagram<sup>[8]</sup> for the dust content of the air flowing through the technology building. *Tu* (superclean) tunnel. The numbers in the 'flow paths' indicate the number of particles larger than  $0.1 \mu\text{m}$  per  $\text{m}^3$  volume; the width of the flow paths is approximately proportional to this number. The filters are indicated by a zig-zag line; the percentages give the degree of filtering for particles of  $0.1 \mu\text{m}$  and larger. *F*<sub>1</sub> outside air filter. *F*<sub>2</sub> prefilter for the superclean process tunnels. *F*<sub>3</sub> final filter for these tunnels. *A* air drawn in from outside. The outside air contains  $10^{11}$  particles per  $\text{m}^3$ . The fresh air amounts to 10% of the circulating air. *B* 1% of leakage air in the outside-air suction line; this leakage air contains  $10^9$  particles per  $\text{m}^3$ . *C* 1% of leakage air in the channels of the circulation system, with the same particle content. *D* 2% of leakage air in the fans of the circulation system, also with the same particle content. *E* exit air from the process rooms; a content of  $2 \times 10^6$  particles per  $\text{m}^3$  is assumed for *E*. This diagram shows that the air in the cleanest process tunnels contains 7 particles of  $0.1 \mu\text{m}$  diameter or more per  $\text{m}^3$ . In calculating the filters a safety factor of 50 was applied to the specification of a maximum of 350 of these particles per  $\text{m}^3$ .

building there are three service buildings for supplying materials used in the production such as decontaminated deionized water and various process gases.

In the technology building each tunnel will have its own 'down-flow' air-circulation system, with a vertical flow from ceiling to floor. There is no possibility of interaction between the different circulation systems. Powerful fans circulate a total of about  $2.2 \times 10^6$  cubic metres of air per hour through the

building, adding 10% of outside air. The Sankey flow diagram in fig. 7 shows the extent to which particles are trapped by the mechanical filters in the superclean tunnels<sup>[8]</sup>. The air entering from outside passes through a filter that traps 99.8% of the particles of diameter  $0.1 \mu\text{m}$  or larger. The air then passes through a 73% prefilter and then, before entering the tunnel, it goes through a 99.99995% filter — clearly a filter of very special design.

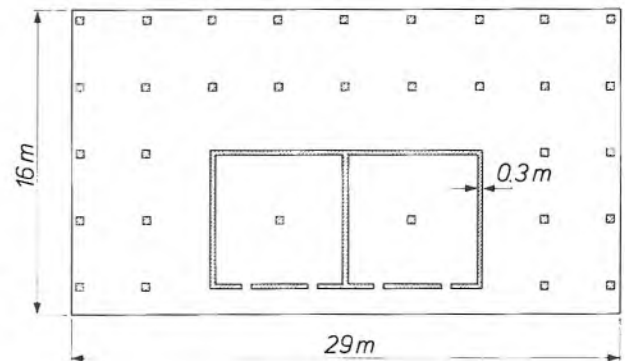


Fig. 8. Horizontal cross-section through the columns and walls that connect the foundation floor and the floor for the wafer steppers. The two floors and the walls form a stiff concrete box construction.

Other important aspects of the design of the technology building are the precautions for suppressing vibration at certain locations. The wafer steppers are the units most sensitive to vibration, so that these precautions relate mainly to the floor on which they stand. These instruments always have their own vibration isolation in the form of weak undamped springs. It can be shown theoretically<sup>[9]</sup> that the spring-mounted instrument should have a low natural frequency, since floor vibrations with a frequency of at least  $\sqrt{2}$  times the natural frequency are attenuated in amplitude. The natural frequency of our wafer steppers on their weak springs is low: 2 to 4 Hz.

The floor and foundations for the wafer steppers are designed to give the whole structure the highest possible natural frequency, in any case higher than  $4\sqrt{2}$  Hz. In addition the combined mass of floor and foundations must be high, so that the impacts of collisions with moving objects will only produce vibrations of low amplitude. A large mass in combination with a high natural frequency results in a high stiffness. In the design of low-vibration buildings it is generally only the stiffness in the vertical direction that is kept

[8] This diagram is based on calculations made by Meissner & Wurst GmbH, Stuttgart, the firm that supplied the air-conditioning equipment.

[9] J. P. den Hartog, Mechanical vibrations, 4th edition, McGraw-Hill, New York 1956.

high. Since impact can also operate in the horizontal direction, the floors for the repeater projectors also have a high stiffness in the horizontal direction.

Calculations have been made for two models of the combined construction of concrete piles, foundation floor and the actual floor for the wafer steppers. In one model both floors are connected by columns, in the other by walls *and* columns, giving a sort of box construction. The calculations on the box-construction model showed that this design had the highest natural frequency in the horizontal direction. *Fig. 8* shows a horizontal cross-section through the concrete construction that has been used. The upper floor is 45 cm thick and supports the wafer steppers. The meas-

ured natural frequency in the horizontal direction is 55 Hz — much higher than the natural frequency of the repeater projectors.

**Summary.** The pilot production of 256-kbit static RAMs will start in about a year at the new centre for submicron technology. Use will be made of CMOS technology and photolithography with wafer steppers. In certain parts of the technology building the dust content of the air will be extremely low and the floors will be extremely insensitive to vibration. The low dust content will be achieved by using separate air-circulation systems for each 'process tunnel' with filters that trap 99.99995% of particles down to a diameter of 0.1  $\mu\text{m}$ . The vibration insensitivity of the floors that support the wafer steppers will be obtained by using a concrete box construction with high vertical and horizontal stiffness.

## Dual-energy X-ray diagnostics

J. J. H. Coumans

---

*In about 1960 the well-known Dutch radiologist B. G. Ziedses des Plantes Sr succeeded in 'subtracting' radiographs produced by hard and soft X-rays. He had described the principle of the subtraction method many years before, in 1934, in his thesis 'Planigraphy and subtraction'. By using hard and soft X-rays he could substantially increase the contrast due to heavy elements such as calcium. However, the method did not become widely used until digital technology and computers were available for rapid image processing. A difficulty with dual-energy imaging in computed tomography until now has been the occurrence of artefacts caused by movement of the object. At Philips it has now been found that these artefacts can be avoided by supplying the X-ray tube with alternate high-voltage and low-voltage pulses during tomography with a Philips CT scanner. The contrast between tissue structures can be varied by carefully processing high-energy and low-energy images. Tissues can also be analysed quantitatively by assigning values for the electron density and atomic number to the individual picture elements (pixels).*

---

### Introduction

The different grey levels in an X-ray image correspond to different attenuations of the X-ray beam in tissue structures. The attenuation is due to the removal of X-ray quanta from the beam by photoelectric absorption, Compton scattering and Rayleigh scattering. In photoelectric absorption X-ray quanta are absorbed by energy transitions of bound electrons. In Compton scattering X-ray quanta collide non-elastically with free electrons; this process is associated with energy loss and hence with an increase in wavelength. In Rayleigh scattering X-ray quanta collide elastically with free electrons, so that there is no change in wavelength. In X-ray diagnostics the most important effects are photoelectric absorption and Compton scattering. In the rest of this article it will therefore be assumed that the slight attenuation due to Rayleigh scattering is included in the photoelectric absorption, so that we shall attribute two physical effects here instead of three to X-ray attenuation.

The contributions of photoelectric absorption and Compton scattering to the total X-ray attenuation are both dependent on the energy of the X-radiation and

on the properties of the tissue. For the same tissue, hard X-radiation — i.e. radiation with a high energy and hence a short wavelength — is more scattered than absorbed; the opposite is the case with soft X-radiation. For the same energy, soft tissue, consisting of light atoms such as oxygen, carbon and hydrogen, gives a great deal of scattering and little absorption of the X-rays. Bone tissue, containing heavy atoms such as calcium, gives a great deal of absorption and little scattering.

This is illustrated in *fig. 1*. In *fig. 1a* the X-ray attenuation coefficient  $\mu$  of polymethyl methacrylate and aluminium is plotted as a function of the X-ray energy. In X-ray attenuation, polymethyl methacrylate is comparable with soft tissue and aluminium is comparable with bone. *Fig. 1b* shows the relative contribution of photoelectric absorption in the total X-ray attenuation for the same materials. The curves for most biological materials lie in the regions bounded by the curves in the two figures.

The X-ray attenuation coefficient can thus be divided into a contribution due to Compton scattering and a contribution due to photoelectric absorption. Each of these contributions is the product of a material-dependent factor and an energy-dependent fac-

---

*Dr Ir J. J. H. Coumans, formerly with Philips GmbH Forschungslaboratorium Hamburg, Hamburg, West Germany, is now with the Medical Systems Division, Philips NPB, Best.*



tor. The energy-dependent factors differ for Compton scattering and photoelectric absorption but they are known: they are functions in which the microscopic collision cross-sections occur. We see that the material-dependent factors in the total X-ray attenuation coefficient are 'weighted' by the energy-dependent factors, so that changing the energy also changes the attenuation coefficient. This means that the contrast in an X-ray image can be altered by changing the energy. Later in this article it will be shown that the material-dependent factors that correspond to a particular ray path in the object can be calculated from *two* X-ray exposures at different energies. This is done by 'splitting off' the — known — energy-dependent factors in the total attenuation coefficient. In this calculation the material-dependent factors for Compton scattering and photoelectric absorption are the two unknowns in two equations, which in principle can therefore be solved.

It was already known in the twenties that the contrast between materials could be increased or reduced

by varying the energy of the X-rays<sup>[1]</sup>. The ideal would be to work with monoenergetic X-radiation, i.e. radiation of one wavelength, or 'colour'<sup>[2]</sup>. The problem is that the X-radiation from the usual source, an X-ray tube, includes radiation at different wavelengths. The spectrum of the radiation from an X-ray tube is a continuous (Bremsstrahlung) spectrum with a minimum wavelength  $\lambda_m$  given by

$$\lambda_m = hc/eV_m,$$

where  $h$  is Planck's constant,  $c$  the velocity of light,  $e$  the electronic charge and  $V_m$  the voltage on the X-ray tube. Superimposed on this continuous spectrum are peaks due to the characteristic radiation from the anode material. It is possible to obtain monoenergetic X-radiation by filtering, e.g. with a crystal monochromator. However, filtering considerably reduces the intensity of the radiation, making exposure times much too long for medical use. Monoenergetic X-radiation of sufficient intensity can be obtained with a synchrotron and a monochromator<sup>[3]</sup>, but a synchrotron is large and expensive. The non-availability of practical monoenergetic X-ray sources means that it is necessary to resort to polyenergetic X-radiation for dual-energy X-ray diagnostics.

Ziedses des Plantes was able to give bone tissue extra contrast by photographically 'subtracting' one radiograph from another: one was made with hard X-radiation and the other with soft X-radiation<sup>[4]</sup>. In his subtraction method he combined these radiographs by using two film cassettes one above the other, separated by a copper plate that acted as a radiation filter. The photographic subtraction technique is cumbersome, however, and is rarely used now. In modern computed tomography different detectors with unequal spectral sensitivities are sometimes used for this<sup>[5]</sup>. The difficulty then is that twice as many detectors, with the associated electronics, are required; this makes the method expensive. Two successive scans can also be made with the X-ray tube at different voltages<sup>[6]</sup>, but this more than doubles the scan time and therefore increases the risk of artefacts due to movement of the object.

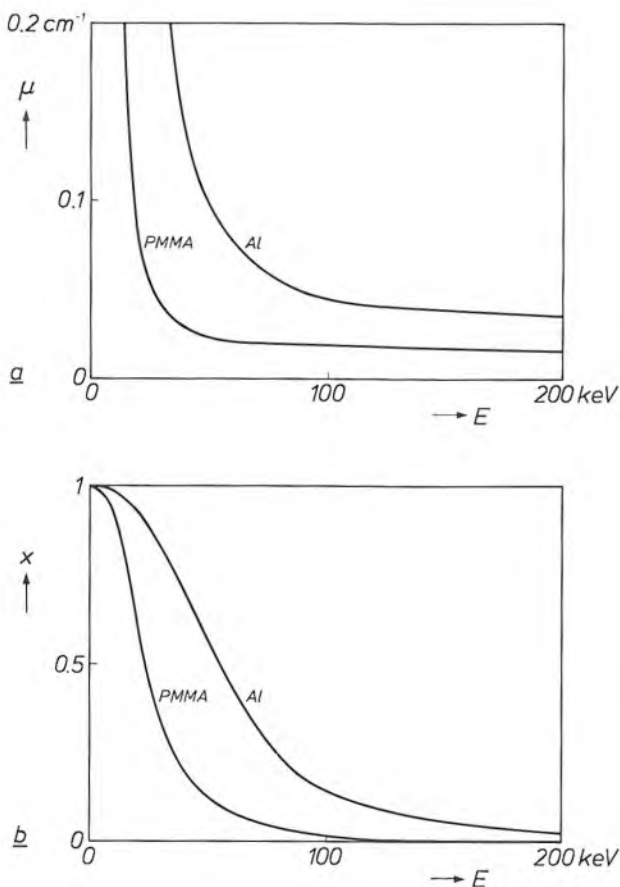


Fig. 1. a) The X-ray attenuation coefficient  $\mu$  as a function of the energy  $E$  of the X-radiation for polymethyl methacrylate (PMMA) and aluminium (Al). ( $E = hc/\lambda$ , where  $\lambda$  is the X-ray wavelength,  $c$  the velocity of light and  $h$  Planck's constant.) b) The ratio  $x$  of the photoelectric absorption to the total X-ray attenuation as a function of X-ray energy for both materials.

- [1] R. Glocker and W. Frohnmayer, Über die röntgenspektroskopische Bestimmung des Gewichtsanteiles eines Elementes in Gemengen und Verbindungen, *Ann. Phys.* 76, 369-395, 1925.
- [2] W. J. Oosterkamp, Monochromatic X-rays for medical fluoroscopy and radiography?, *Medicamundi* 7, 68-77, 1961.
- [3] B. Vinocur, High-tech physics advance noninvasive angiography, *Diagnostic Imaging*, February 1985, pp. 109-110.
- [4] B. G. Ziedses des Plantes, *Subtraktion*, Thieme, Stuttgart 1961.
- [5] R. A. Brooks and G. Di Chiro, Split-detector computed tomography: a preliminary report, *Radiology* 126, 255-257, 1978.
- [6] A. Macovski, R. E. Alvarez, J. L.-H. Chan, J. P. Stonestrom and L. M. Zatz, Energy dependent reconstruction in X-ray computerized tomography, *Comput. Biol. & Med.* 6, 325-336, 1976.

To overcome these disadvantages we have modified a computer tomograph (a Philips Tomoscan 300 CT scanner) [7], see *fig. 2*, so that scans can be made at different X-ray energies without the occurrence of movement artefacts [8]. (The operation of a CT scanner will be dealt with at the end of the article.) The improvement was made by modifying the high-voltage generator to apply, every 14 ms, a high-voltage pulse followed by a low-voltage pulse. The pulse pairs are generated at a frequency equal to half that of the voltage pulses normally used for the CT scanner. Far less modification of the CT scanner is required than if different detectors were used; the modification is also suitable for the later types of CT scanner, the Tomoscan 310 and 350.

In modern dual-energy X-ray diagnostics computational methods are used to derive the attenuation coefficients for the individual pixels from the ratio of measured X-ray intensities with an object in the beam and without. The material-dependent factors corresponding to the photoelectric absorption and the Compton scattering can then be identified from these coefficients. These factors can then be converted into quantities such as the atomic number and the electron density for each pixel, so that in principle a quantitative analysis of tissue is now possible. It will be clear that these methods of calculation can be effectively combined with the digital image-reconstruction methods used in computed tomography.

We have developed a new method in which the X-ray images are recalculated to produce monoenergetic images for a wide energy range. After the actual X-ray CT scan the radiologist can select the notional X-ray energy that gives the greatest possible contrast between the tissues of interest. Images can then be studied at different X-ray energies without having to subject the patient to repeated exposures.

As the polyenergetic X-radiation travels through the object the mean wavelength is reduced owing to the energy-dependent attenuation of the rays. This hardening of the X-ray beams makes a special calibration technique necessary. The CT scanner is therefore regularly calibrated with objects in which aluminium simulates bone tissue and polymethyl methacrylate simulates soft tissue.

In the next section the way in which the X-ray attenuation coefficient can be split into separate contributions due to photoelectric absorption and Compton scattering will be explained. The representation of a material as a vector in a coordinate system will then be discussed. This will be followed by an account of the calibration method and the modifications to the Tomoscan 300. In the final section the applications of dual-energy X-ray diagnostics in CT scanning (com-



Fig. 2. The Philips CT scanner Tomoscan 300, which is outwardly similar to the later types Tomoscan 310 and 350. Only the scanner and patient table are shown here; the complete equipment is shown in *fig. 5a*.

puted tomography), CR scanning (computed radiography) and DVI (digital vascular imaging) will be discussed.

## Theory

### Splitting the X-ray attenuation coefficient

As we have just noted the X-ray attenuation coefficient  $\mu$  (in  $\text{cm}^{-1}$ ), which is a function of the energy of the X-ray quanta, can be split into separate contributions, one due to the Compton scattering and the other due to the photoelectric absorption. Each contribution is the product of a material-dependent factor and an energy-dependent factor. We thus obtain the function:

$$\mu(E) = a_c f_c(E) + a_p f_p(E), \quad (1)$$

where the subscripts c and p relate to Compton scattering and photoelectric absorption, and  $E$  represents the energy of the X-ray quanta.

It is found from equation (1) and *fig. 1b* that the energy of the X-radiation can be selected in such a way that either the photoelectric absorption or the attenuation due to Compton scattering predominates. The contrast between two tissues in an X-ray image can therefore be altered by varying the factors  $f_c(E)$  and  $f_p(E)$  in eq. (1). Since in principle these factors are known, it is sufficient to make two X-ray exposures at different energies. The unknown material-dependent factors  $a_c$  and  $a_p$  can then be found by solving two simultaneous equations.

An element can be characterized by its atomic number  $Z$  and electron density  $\rho$  (in  $\text{cm}^{-3}$ ). A biological material can be assigned an effective atomic number

$Z_{\text{eff}}$  and an effective electron density  $\rho_{\text{eff}}$ . Both these quantities then give the same material-dependent factors for a biological material as those for an element with atomic number  $Z = Z_{\text{eff}}$  and electron density  $\rho = \rho_{\text{eff}}$ .

The electron density is the product of the atomic number and the atomic density  $N$ , the number of atoms per unit volume:  $\rho = NZ$ . It can be shown that the electron density is proportional to the factor  $a_c$  in equation (1) and that the atomic number is proportional to  $(a_p/a_c)^{0.3}$ . The two material-dependent energy-independent factors  $a_c$  and  $a_p$  can therefore be used to analyse biological tissue quantitatively.

It can be shown that the electron density is proportional to  $a_c$  and the atomic number is proportional to  $(a_p/a_c)^{0.3}$  as follows. For a given element the term  $a_c f_c(E)$  in (1) can also be written as  $N\sigma_c$ , where  $\sigma_c$  is the microscopic collision cross-section (in  $\text{cm}^2$ ) for Compton scattering. This collision cross-section can be calculated for a given element and a given X-ray energy  $E$  from equation [9]

$$\sigma_c = 2\pi r_0^2 Z f_{\text{KN}} \left( \frac{E}{mc^2} \right).$$

In this expression  $Z$  represents the atomic number,  $r_0 = 2.818 \times 10^{-13}$  cm is the classical radius of the electron,  $f_{\text{KN}}$  is the Klein-Nishina function, and  $mc^2 = 510.975$  keV is the ground-state energy of the electron. We can now derive expressions for the factors  $a_c$  and  $f_c(E)$  in (1):

$$a_c = 2\pi r_0^2 NZ \quad (2)$$

and

$$f_c = f_{\text{KN}} \left( \frac{E}{mc^2} \right). \quad (3)$$

The term  $a_p f_p(E)$  in (1) can be written in a similar way as  $N\sigma_p$ , where  $\sigma_p$  is the microscopic collision cross-section for photoelectric absorption. This collision cross-section can be calculated from the expression

$$\sigma_p = C_p Z^n E^{-m},$$

where  $C_p$  is a constant (it is not dimensionless), and  $n$  and  $m$  represent material-dependent exponents [10]. For oxygen  $C_p = 21 \times 10^{-24}$ ,  $n = 4.6$  and  $m = 3.2$ . (For most biological materials a good approximation for  $m$  is 3.0.) We now have the following expressions for the factors  $a_p$  and  $f_p(E)$  in (1):

$$a_p = N C_p Z^n \quad (4)$$

and

$$f_p(E) = E^{-m}. \quad (5)$$

An expression for the effective electron density of a biological material can be derived from (2):

$$\rho_{\text{eff}} = k_1 a_c,$$

where  $k_1$  is a constant. Dividing equation (2) by equation (4) gives an expression for the effective atomic number:

$$Z_{\text{eff}} = k_2 \left( \frac{a_p}{a_c} \right)^l,$$

where  $k_2$  is a constant and the exponent  $l$  is equal to  $1/(n-1) \approx 0.3$ .

For any given material the quantities  $\mu(E)$ ,  $f_c(E)$  and  $f_p(E)$  in equation (1) are known:  $\mu(E)$  is published in handbooks and  $f_c(E)$  and  $f_p(E)$  are known functions of the X-ray energy. It is therefore possible to calculate the material-dependent factors  $a_c$  and  $a_p$  by taking the minimum of the sum of the squares of the relative deviations

$$\varepsilon = \frac{\mu(E) - a_c f_c(E) - a_p f_p(E)}{\mu(E)} \quad (6)$$

for a number of different energy values. In this way we have calculated the factors  $a_c$  and  $a_p$  for the materials aluminium, polymethyl methacrylate and water in the energy range from 30 to 100 keV. Fig. 3 gives the deviation  $\varepsilon$  for these materials as a function of energy. From 30 to 150 keV the deviation is less than 0.5%. This shows that the model corresponding to equation (1) gives a good approximation to reality. In principle this only applies to materials whose atomic number is less than 50. In addition, the materials in the range of energies quoted should not have a K absorption edge (a sudden change in the absorption coefficient due to an energy transition of a K electron). Biological materials satisfy these conditions.

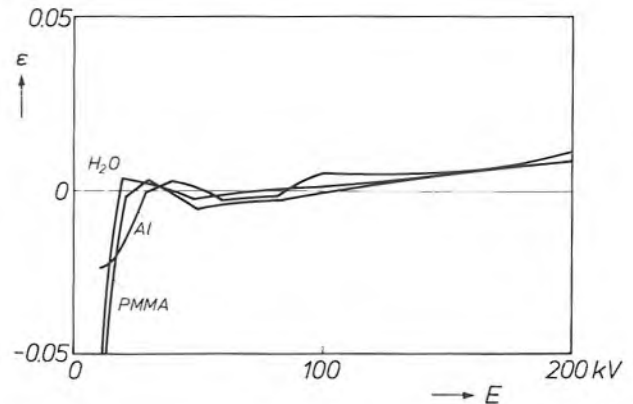


Fig. 3. The relative deviation  $\varepsilon$  (eq. 6) as a function of X-ray energy for polymethyl methacrylate (PMMA), water ( $\text{H}_2\text{O}$ ) and aluminium (Al). The quantity  $\varepsilon$  is the deviation of the model that splits the X-ray attenuation due to Compton scattering and to combined photoelectric absorption and Rayleigh scattering into an energy-dependent factor and a material-dependent factor.

[7] F. W. Zonneveld, Computed tomography, Philips Medical Systems Division, Best 1983.

[8] F. W. Zonneveld, A new method for in vivo energy-selective CT imaging, Proc. 15th Int. Congr. of Radiology, Vol. Technics and Physics, Brussels 1981, pp. 280-289; W. R. Brody, D. M. Cassel, F. G. Sommer, L. A. Lehmann, A. Macovski, R. E. Alvarez, N. J. Pelc, S. J. Riederer and A. L. Hall, Dual-energy projection radiography: initial clinical experience, Am. J. Roentgenol. 137, 201-205, 1981; J. J. H. Coumans, Doppel-Energie Computer-Tomographie und -Radiographie, Thesis, Braunschweig 1983.

[9] O. Klein and Y. Nishina, Über die Streuung von Strahlung durch freie Elektronen nach der neuen relativistischen Quantendynamik von Dirac, Z. Phys. 52, 853-868, 1929.

[10] E. C. McCullough, Photon attenuation in computed tomography, Med. Phys. 2, 307-320, 1975.

*Characterization of a material by a vector*

For simplicity we shall assume here that our X-radiation is monoenergetic. As the radiation passes through the object the intensity  $I_i$  in front of the object falls to the intensity  $I_o$  behind the object. The relation between the two is given by

$$I_o = I_i e^{-M}, \tag{7}$$

where the attenuation exponent  $M$  is given by

$$M = \int_{s_1}^{s_0} \mu ds. \tag{8}$$

Here the material-dependent, and hence in general position-dependent, attenuation coefficient  $\mu$  given by eq. (1) is integrated with respect to the coordinate of position  $s$  between the limits  $s_1$  and  $s_0$  for the incidence and emergence of the radiation. If the signals from an X-ray detector with and without an object in the beam are compared the natural logarithm of the ratio of the signals is  $-M$  (eq. 7). The quantity  $T = -M$  is called the logarithmic decrement. A large number of values for  $T$ , for different paths for the X-radiation through the object, must finally produce a reconstruction of a particular part of the object.

With the aid of (1) we can write equation (8) as:

$$M = A_c f_c(E) + A_p f_p(E), \tag{9}$$

where the material-dependent factors  $A_c$  and  $A_p$  are given by:

$$A_c = \int_{s_1}^{s_0} a_c ds, \tag{10}$$

$$A_p = \int_{s_1}^{s_0} a_p ds. \tag{11}$$

If the X-radiation passes through one kind of material, these factors are not only characteristic of that material but are also proportional to its thickness.

For a given thickness  $d_m$  we can characterize a material  $m$  — or a combination of a number of materials — by a vector  $m$  in a rectangular coordinate system in which normalized factors  $A'_{c,m}$  and  $A'_{p,m}$  are plotted along the two axes; see fig. 4a. The normalization consists in comparing the factors  $a_{c,m}$  and  $a_{p,m}$  for the material with the factors  $a_{c,H_2O}$  and  $a_{p,H_2O}$  for water. The components of the vector are then given by:

$$m = (A'_{c,m}, A'_{p,m}) = \left( \frac{a_{c,m}}{a_{c,H_2O}} d_m, \frac{a_{p,m}}{a_{p,H_2O}} d_m \right). \tag{12}$$

If the X-rays pass through an object consisting entirely of water with a layer thickness  $d_{H_2O}$ , the attenuation exponent given by (9) can be written for water as:

$$M_{H_2O} = a_{c,H_2O} d_{H_2O} f_c(E) + a_{p,H_2O} d_{H_2O} f_p(E). \tag{13}$$

With variable thickness  $d_{H_2O}$ , different values of  $M_{H_2O}$

in a  $(d_{H_2O} r_{c,E}, d_{H_2O} r_{p,E})$ -plane that we make coincident with the  $(A'_{c,m}, A'_{p,m})$ -plane correspond to vectors whose end-points lie on a straight line with the directional vector

$$r = (r_{c,E}, r_{p,E}) = \{a_{c,H_2O} f_c(E), a_{p,H_2O} f_p(E)\}. \tag{14}$$

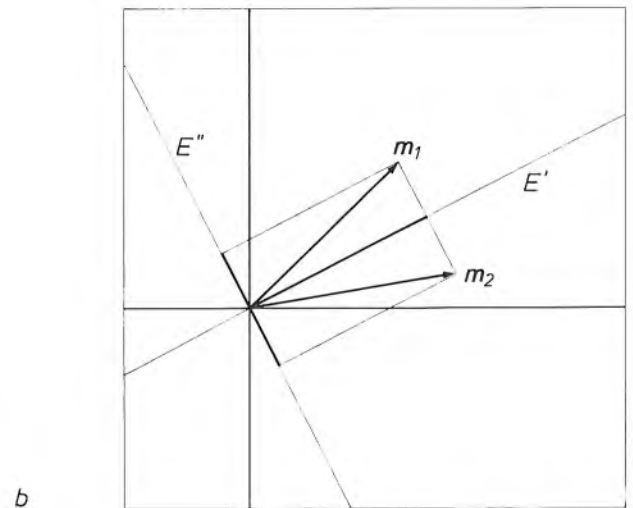
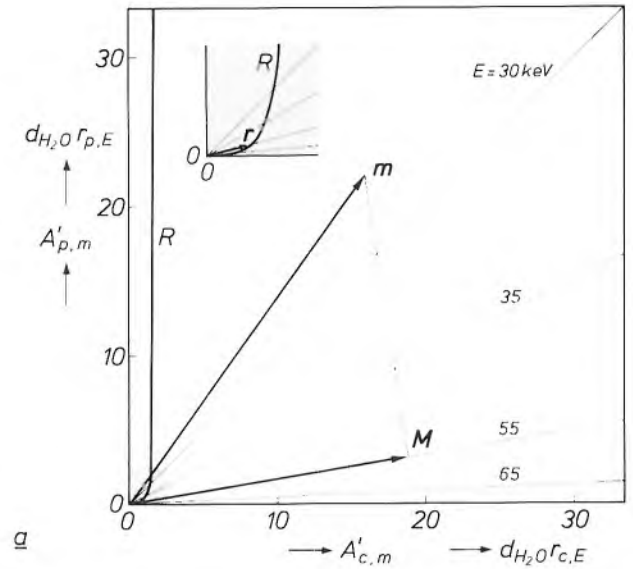


Fig. 4. a) Characterization of a material by a vector  $m$  with components  $A'_{c,m}$  and  $A'_{p,m}$  as given by equation (12). The components  $A'_{c,m}$  and  $A'_{p,m}$  are the energy-independent contributions to the attenuation exponent due to Compton scattering, and due to photoelectric absorption. The contributions are dependent on material and thickness, and are normalized with respect to water.  $R$  curve traced out by the end-points of vectors  $r$  with components  $r_{c,E}$  and  $r_{p,E}$  as given by equation (14). (See also the enlarged detail.) These vectors determine the direction of lines through the origin for the vectorial energy-dependent attenuation exponent of water with layer thickness  $d_{H_2O}$  as given by equation (13). Each line corresponds to a constant value of the X-ray energy  $E$ . The vectorial energy- and material-dependent attenuation exponent  $M$ , which is determined by the choice of a notional X-ray energy after the exposure, is found by projecting the vector  $m$  on to a line for the attenuation exponent of water at this X-ray energy. b) For two adjacent picture elements (pixels) with material vectors  $m_1$  and  $m_2$  the X-ray energy  $E'$  gives no contrast and  $E''$  gives maximum contrast. The line for  $E'$  is perpendicular to the line that connects the end-points of the vectors; the line for  $E''$  is perpendicular to the line for  $E'$ .

When  $E$  tends to infinity,  $r$  tends to take up the direction of the horizontal axis and becomes infinitely small (Compton scattering only); when  $E$  tends to zero,  $r$  tends to take up the direction of the vertical axis and becomes infinitely large (photoelectric absorption only). The end-points of the vectors  $r$  lie on a curve,  $R$  in fig. 4a. The figure also shows a number of lines for the attenuation exponent of water at constant energy; their direction follows from that of the directional vector given by (14).

The energy-dependent and material-dependent attenuation exponent  $M$  given by (9) can be displayed as a vector in the combined  $(d_{H_2O}r_{c,E}, d_{H_2O}r_{p,E})$ - and  $(A'_{c,m}, A'_{p,m})$ -plane. This vector is shown as  $M$  in fig. 4a. The length of the vector  $M$  is equal to the scalar product of the vectors  $m$  and  $r$  given by (12) and (14):

$$|M| = m \cdot r = a_{c,m}d_m f_c(E) + a_{p,m}d_m f_p(E).$$

The attenuation exponent for a given radiant energy (notional or not) can thus be found by projecting the material vector  $m$  given by (12) on to the line of the attenuation exponent of water for this energy.

Fig. 4b shows how certain contrasts can be selectively enhanced or removed by choosing an appropriate X-ray energy. The vectors  $m_1$  and  $m_2$  relate to two materials of a particular thickness. If we choose an energy  $E'$ , corresponding to a line perpendicular to the line that connects the end-points of  $m_1$  and  $m_2$ , the attenuation exponents are equal and so therefore are the logarithmic decrements. The reconstructed pixels then show no contrast. (For the same magnitude of  $m_1$  and  $m_2$ , as in fig. 4b, the line for  $E'$  corresponds to the bisector of the angle between the two vectors.) If we choose an energy  $E''$ , corresponding to a line perpendicular to that of  $E'$ , the contrast between the reconstructed pixels is at a maximum.

It is possible in principle to choose an arbitrary notional energy for the X-radiation after an actual exposure by determining the factors  $A_c$  and  $A_p$  from two different monoenergetic measurements of the logarithmic decrement. From this the normalized factors  $A'_{c,m}$  and  $A'_{p,m}$  can be obtained, giving the direction and magnitude of the vector  $m$ . The vector  $M$  is obtained from the projection of  $m$  on to the line relating to the desired energy. As noted above, monoenergetic radiation sources are not available for routine X-ray diagnostics. As we shall now see, this problem can be overcome by means of calibration.

#### The calibration method

It was pointed out earlier that the change in the shape of the X-ray spectrum, as the radiation penetrates deeper into the material, complicates the choice of calibration method. The mean wavelength of the

spectrum is gradually reduced because soft radiation is attenuated more than hard radiation.

This hardening of the X-radiation can be described quantitatively as the change in the effective energy  $E_{eff}$ . The effective energy of polyenergetic X-radiation is defined as the energy of monoenergetic radiation which, in travelling a given distance in water, yields the same logarithmic decrement as the polyenergetic radiation does in travelling the same distance.

The calibration that has generally been used in computed tomography until now gives coefficients  $c_1$ ,  $c_2$  and  $c_3$  of a third-degree equation for the product of material thickness  $d_m$  and attenuation coefficient  $\mu$ , with the measured logarithmic decrement  $T$  as independent variable:

$$\mu d_m = c_1 T + c_2 T^2 + c_3 T^3.$$

This calibration method, however, takes no account of the increase in the effective energy and hence of the change in the factors  $f_c(E)$  and  $f_p(E)$  in (1). The result of the calibration therefore contains a systematic error.

The calibration method that we use is not based on the attenuation coefficient, which is energy-dependent, but on the factors  $A_c$  and  $A_p$ , which are independent of energy. In this method we use objects made of layers of aluminium and polymethyl methacrylate — materials that are comparable with bone and soft tissue in terms of X-ray attenuation, as noted earlier. Using published tabulated data<sup>[11]</sup> we can calculate the factors  $A_p$  and  $A_c$  for the various combinations of layer thicknesses  $d_t$  and  $d_b$  in the objects from the relations

$$A_c = a_{c,t}d_t + a_{c,b}d_b,$$

and

$$A_p = a_{p,t}d_t + a_{p,b}d_b.$$

The subscript t relates to simulated soft tissue, and the subscript b to bone.

Two polyenergetic X-ray pencil beams, generated at different tube voltages, are used for measuring the logarithmic decrements  $T_h$  at high effective energy and  $T_l$  at low effective energy for the various calibration objects. From the measured  $T_h$  and  $T_l$  and the calculated  $A_c$  and  $A_p$  the method of least squares can be used to calculate two series of nine coefficients  $c_{1,0}$  to  $c_{3,3}$  and  $p_{1,0}$  to  $p_{3,3}$ , which are defined by the relations

$$A_c = \sum_{j=1}^3 \sum_{k=0}^j c_{j,k} T_l^{j-k} T_h^k,$$

$$A_p = \sum_{j=1}^3 \sum_{k=0}^j p_{j,k} T_l^{j-k} T_h^k.$$

[11] J. H. Hubbell, Photon cross sections, attenuation coefficients and energy absorption coefficients from 10 keV to 100 GeV, National Standard Reference Data Series NSRDS-NBS-29, National Bureau of Standards, Washington, DC, 1969.



With the calibration coefficients calculated in this way logarithmic decrements of real biological materials measured in the same arrangement can be recalculated to give energy-independent factors  $A_c$  and  $A_p$ . These can then be used for reconstructing X-ray images in which the contrast is due to Compton scattering alone or photoelectric absorption alone. When the material-dependent factors are weighted by the energy-dependent factors, as in fig. 4a, images are obtained at any optional value of the effective energy. This notional variation of the X-ray energy can be used, as noted earlier, to enhance or reduce contrasts between tissues. We shall see that the contrast between soft tissue and bone can in fact be eliminated.

## Applications

### Computed tomography

Fig. 5a shows a complete Philips CT scanner. The heart of the equipment is shown in fig. 5b and c: the yoke with the X-ray source and the detector array. The source generates a 'fan' of rays over an angle of  $43.2^\circ$ ; the fan includes the complete object. The X-ray source is a metal/ceramic tube with rotating anode<sup>[12]</sup>. Each of the 288 detectors in the Tomoscan 300 measures the intensity of a pencil beam after it has passed through the object. (The later types of Tomoscan, types 310 and 350, have 576 detectors, twice as many as the Tomoscan 300.) During a scan lasting 4.2 s the yoke rotates through an angle of  $360^\circ$  around the object, and a pulse of radiation is generated every 7 ms, so there are 600 pulses. (An even better signal-to-noise ratio can be obtained if the number of pulses during one rotation is doubled, and hence the radiation dose and the duration of the scan.) The array of detectors is contained in a common enclosure which is filled with the inert gas xenon. The individual detectors are formed by using the electrodes to subdivide the enclosure. This is achieved by mounting the electrodes radially with respect to the focus of the X-ray tube. Two adjacent electrodes form the side walls of the ionization chamber of one detector and also act as a Soller slit diaphragm for suppressing scattered radiation. In normal operation, with a fixed high voltage on the X-ray tube, the Tomoscan 300 obtains  $600 \times 288$  values of the logarithmic decrement; the number in the Tomoscan 310 and 350 is  $600 \times 576$ . These values are derived from the detector signals of scans with and without an object. The system computer uses a reconstruction algorithm to calculate, from the logarithmic decrements, values for the attenuation coefficient for the pixels of the object to be constructed. This gives a matrix of  $256 \times 256$  numbers, which are converted into grey levels for the video pic-

ture that appears on the display screen of the operator's console.

As stated earlier, the object of our investigation was to modify the CT scanner in such a way that the values of the logarithmic decrement could be obtained at two different X-ray source voltages and therefore at two effective energy levels of the X-radiation. This can be done in different ways. Fig. 6a shows for each of the possible procedures the mean time  $\tau$  between detector signals at high and low X-ray energy. If two

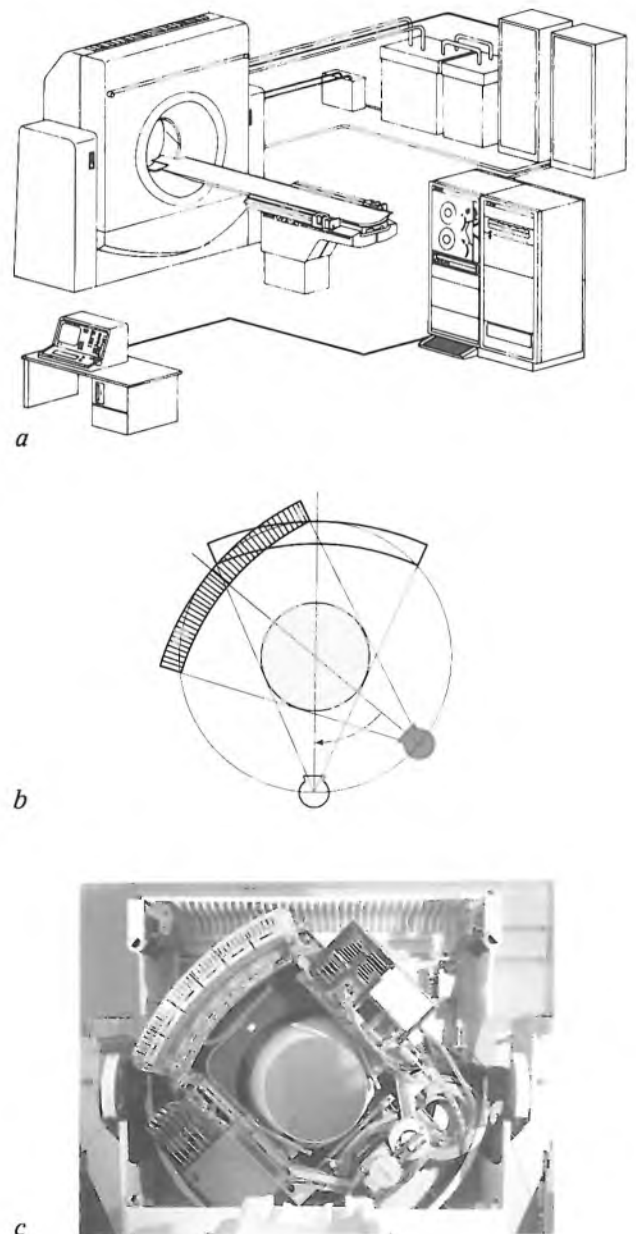


Fig. 5. a) The complete Philips CT scanner. The operating console is shown at the lower left, the power-supply units are on the right at the back, and the system computer at the lower right. b) The heart of the machine: the rotary yoke with the X-ray source and the detector array. The object is shown in light grey. c) Photograph of the yoke of the Tomoscan 300. The X-ray tube is at the lower right.

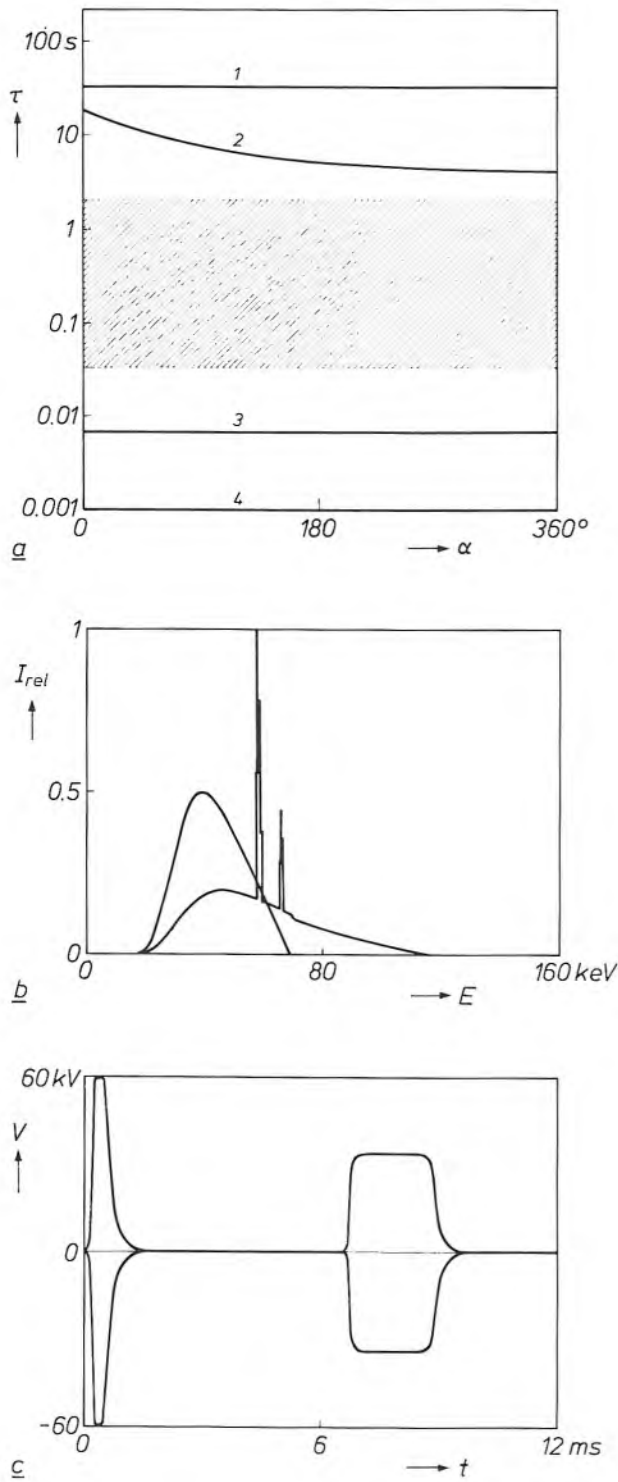


Fig. 6. a) The average time  $\tau$  between detector signals of a CT scanner at high and low X-ray energy as a function of the angle of rotation  $\alpha$  of the yoke; see fig. 5b and c. The possible procedures are: 1 two scans, one with high energy after another with low energy, with the same direction of rotation; 2 as 1, but with opposite directions of rotation; 3 one scan with alternating radiation pulses of high-energy and low-energy radiation; 4 one scan with duplicated radiation detectors of different sensitivity. The characteristic times for movements of the patient or organs in the patient come within the hatched area. b) Radiation spectra, the relative intensity  $I_{rel}$  as a function of X-ray energy  $E$ , corresponding to the alternating radiation pulses in our procedure 3. The tube voltages are 70 and 120 kV. c) Oscillogram of the voltage pulses applied to the X-ray tube.  $V$  voltage.  $t$  time.

successive scans are made at different energies, this time is longer than the characteristic times of movements of the patient (or of organs in the patient). These times correspond to the hatched area in the figure. If dual detectors are used, each with a different sensitivity to certain ranges for the radiant energy, then  $\tau$  is equal to zero. However, operating with dual detectors requires extensive modification of the scanner. We therefore adopted a procedure in which, every 14 ms, an X-ray pulse is generated at 70 kV and a pulse at 120 kV tube voltage. The two radiation spectra are shown in fig. 6b, and the oscillogram of the voltage pulses is given in fig. 6c. The location of line 3 in fig. 6a makes it clear that this procedure involves no risk of movement artefacts.

Fig. 7 shows how the modification of the CT scanner allows the contrast in the X-ray image to be varied. Fig. 7a shows images in which the contrasts are due entirely to Compton scattering or entirely to photoelectric absorption. Fig. 7b shows synthesized monoenergetic images obtained with effective energies of 25 to 125 keV. The object is an AAPM (American Association of Physicists in Medicine) phantom. It consists of a polymethyl-methacrylate container filled with water and surrounded by a concentric ring of polytetrafluorethylene. Inside the container there are cylindrical inserts of different types of plastic. The X-ray attenuations of the materials of the model are very similar to those of bone and tissues in the cranium. The figure shows that certain contrasts in the 25-keV image completely disappear at high energy; on the other hand, other contrasts are enhanced at high energy. The photoelectric image and the low-energy images are 'noisy' because these images are formed from a smaller number of X-ray quanta.

Fig. 8 shows that this method can be used for measuring the bone mineral content of a vertebra, so that calcium loss and the effect of administering certain drugs can be determined. Our method is simpler than bone densitometry, previously the standard method. Dual-energy scanning can eliminate systematic errors in measurements of bone-calcium content, introduced for example by fatty tissue.

### Computed radiography

Computed radiography (CR scanning) is an application of the CT scanner in which the yoke with tube and detector array is kept stationary while the patient table is moved along a straight line at right angles to the detectors. The image obtained in this way with the Philips scanners is called a 'scanogram' [13]. It is pro-

[12] W. Hartl, D. Peter and K. Reiber, A metal/ceramic diagnostic X-ray tube, Philips Tech. Rev. 41, 126-134, 1983/84.

[13] F. W. Zonneveld, The scanogram; technique and applications, Medicamundi 25, 25-28, 1980.

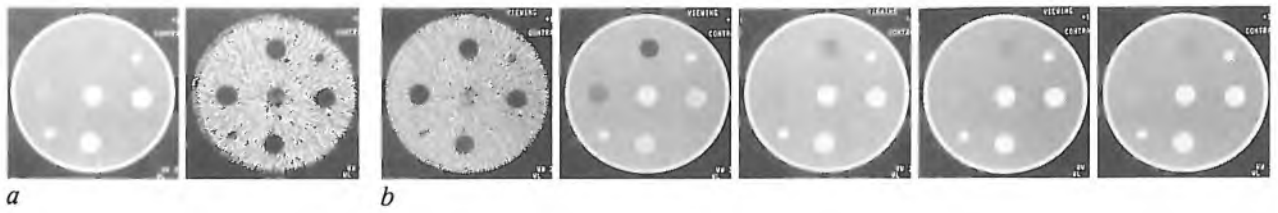


Fig. 7. Varying the contrast in CT images (computed tomography) of the AAPM phantom, which simulates the X-ray attenuation in the cranium. *a*) X-ray images with contrasts due entirely to Compton scattering (left) and entirely to photoelectric absorption (right). *b*) Synthesized monoenergetic X-ray images at 25, 50, 75, 100 and 125 keV.

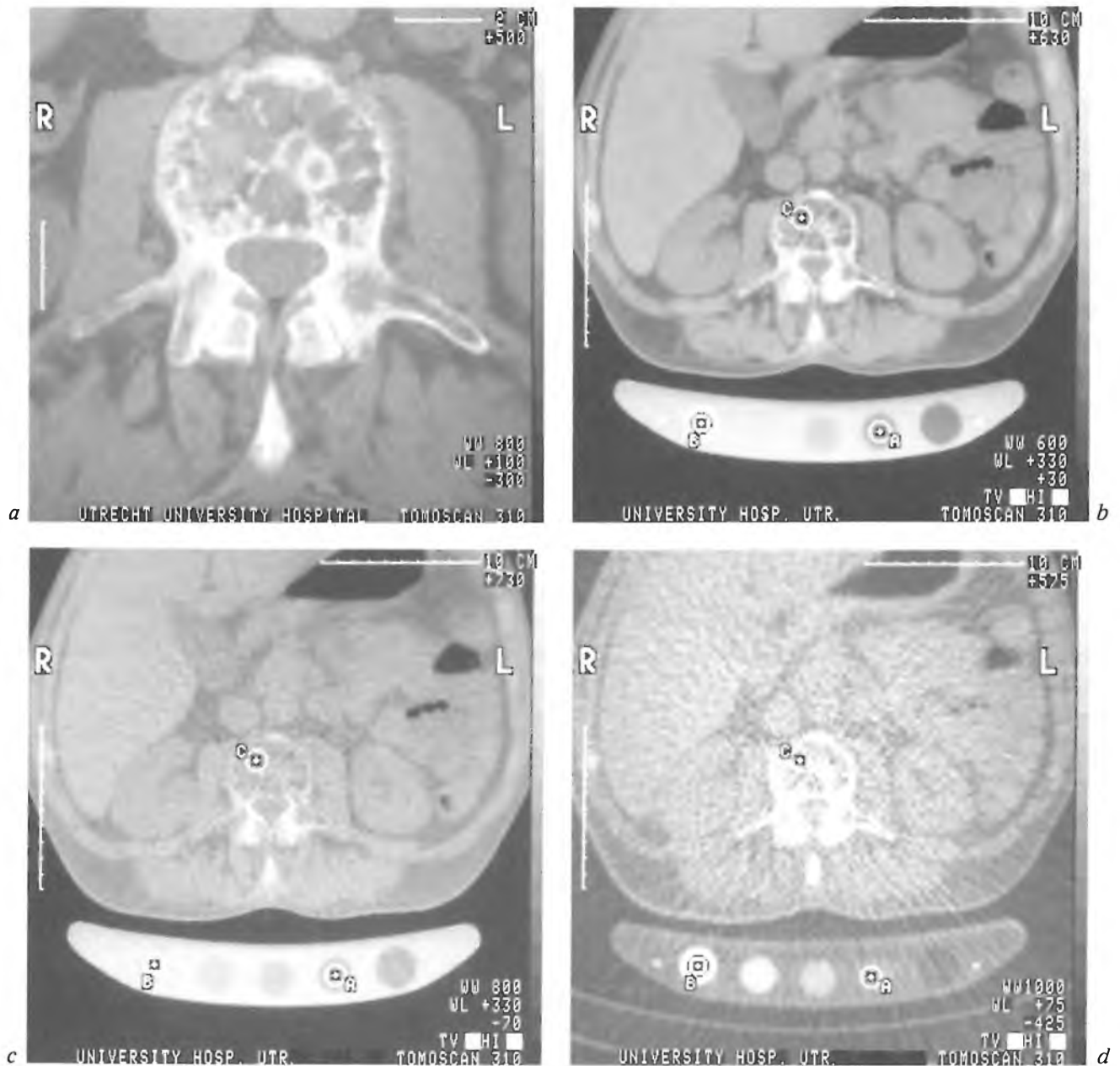


Fig. 8. Measurement of the mineral content of the bone in a vertebra (L3, the third lumbar vertebra from the top) with the modified Philips CT scanner. *a*) CT scan of the vertebra alone, to determine the position where the bone mineral content should be measured. *b*) Synthesized monoenergetic X-ray image at 75 keV. *C*) Position where the bone mineral content is measured. *A*) water channel in a calibration phantom in the patient table. *B*) channel containing a  $K_2HPO_4$  solution at a concentration of  $200 \text{ g/dm}^3$ , which has an attenuation comparable to that of bone mineral. Because of the

high fat content of the vertebra, calculations based on this exposure indicate an erroneous negative bone mineral content. *c*) X-ray image with contrasts due entirely to Compton scattering. *d*) as (*c*), but for photoelectric absorption. From these images the material-dependent factors due to Compton scattering and photoelectric absorption can be calculated for the pixels *A*, *B* and *C*. These factors give a positive bone mineral content for the point *C* in the vertebra. The measured bone mineral content gives an impression of the calcium loss, in this case for a patient suffering from Kahler's disease.

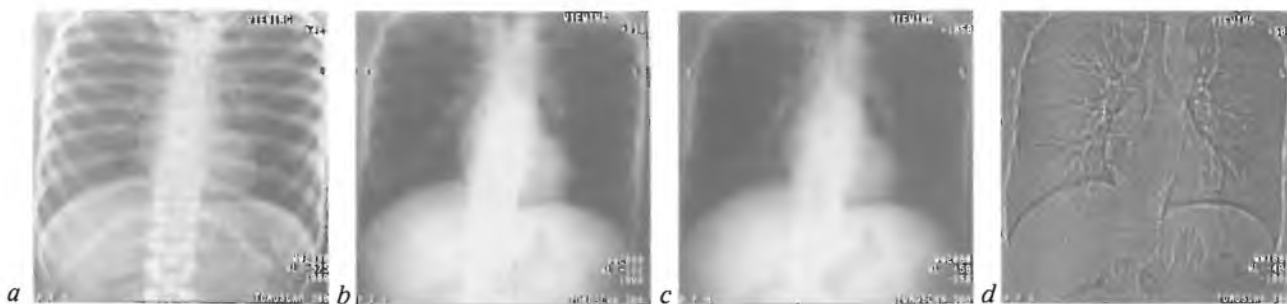


Fig. 9. Synthesized monoenergetic images of a CR (computed radiography) thorax scan at a) 10 keV, b) 50 keV and c) 120 keV, also made with the modified Philips CT scanner. In the image obtained at 120 keV the contrast between bone and surrounding tissue is almost zero, so that the lungs can be observed without the ribs. d) Example of a digital image-processing technique, edge enhancement, applied to the thorax exposure at 120 keV. This improves the visibility of the blood vessels.

duced in the following way. During the movement of the patient an X-ray pulse is generated every time the patient is displaced by a distance equal to the detector pitch. The logarithmic decrements of the detector signals with and without an object are processed to obtain an image that is comparable with that of a conventional radiograph. In this method, however, the digital values obtained for each pixel are very suitable for a variety of image-processing techniques. The scanogram, which was originally introduced just for positioning the patient correctly for CT scanning, has thus become a new medical aid with its own diagnostic potential. The principle of dual-energy image processing can also be applied here, by alternately applying high-voltage and low-voltage pulses to the X-ray tube.

Fig. 9 shows how the contrast of bone and tissue can be reduced almost to zero by changing the effective energy. The images are synthesized radiographs of the thorax, and were obtained at effective energies of 10, 50 and 120 keV by varying the contributions from Compton scattering and photoelectric absorption (9a, b and c). At high energy there is hardly any contrast between the ribs and the surrounding tissue, so that the image shows lung tissue alone.

The image of the lungs can be further improved by employing another digital image-processing technique, known as edge enhancement or 'unsharp masking'. This is one of the methods of manipulating the spatial frequencies in the image, called spatial filtering<sup>[14]</sup>; it is one of the standard image-processing techniques offered by the Philips CT scanners. An 'unsharp mask' is generated from the original image by replacing the grey level for each pixel by the mean value of the grey levels of say the  $5 \times 5$  pixels with the original pixel at their centre. The difference between the original and the unsharp mask is then added to the original with a weighting factor. The higher spatial frequencies in the image are then enhanced, as can be seen in fig. 9d,

where details such as the branching of the blood-vessels in the lungs are clearly visible.

#### DVI

The combination of X-ray images obtained at two energy levels has also been found useful in diagnostic systems in which video signals are processed digitally<sup>[15]</sup>. Philips equipment for digital vascular imaging (DVI) is an example of such a system. In DVI, which is also known as DSA (Digital Subtraction Angiography), the Ziedses des Plantes subtraction method is applied to video signals of X-ray images with a contrast medium and without. Fig. 10a shows a photograph of X-ray equipment to which DVI equipment has been added; fig. 10b is a block diagram of a DVI system. Together with an X-ray stand, a complete system consists of a rotary-anode X-ray tube, an X-ray image intensifier, a TV camera tube that supplies the video signals, a high-voltage generator, electronics for the signal conversions and for processing and storing digital signals, and a magnetic disc memory (a Winchester disc).

The procedure in DVI diagnostics is as follows. First of all a radiograph is made, and after logarithmic amplification and analog-to-digital conversion, it is stored as a mask in the memory *RAM1*. Next a contrast medium is injected into a vein and exposures are then made at a maximum of 3 per second. The successive radiographs are temporarily stored in the memory *RAM2*. The memories *RAM1* and *RAM2* cannot contain more than the digital information from one image, so the previous image with the contrast medium in *RAM2* is always erased and replaced by a new image. Immediately after an exposure has

<sup>[14]</sup> A. Hoyer and M. Schlindwein, Digital image enhancement, Philips Tech. Rev. 38, 298-309, 1978/79.

<sup>[15]</sup> C. A. Mistretta *et al.*, Digital vascular imaging, Medicamundi 26, 1-10, 1981; L. A. J. Verhoeven, Digital subtraction angiography, Thesis, Delft 1985.



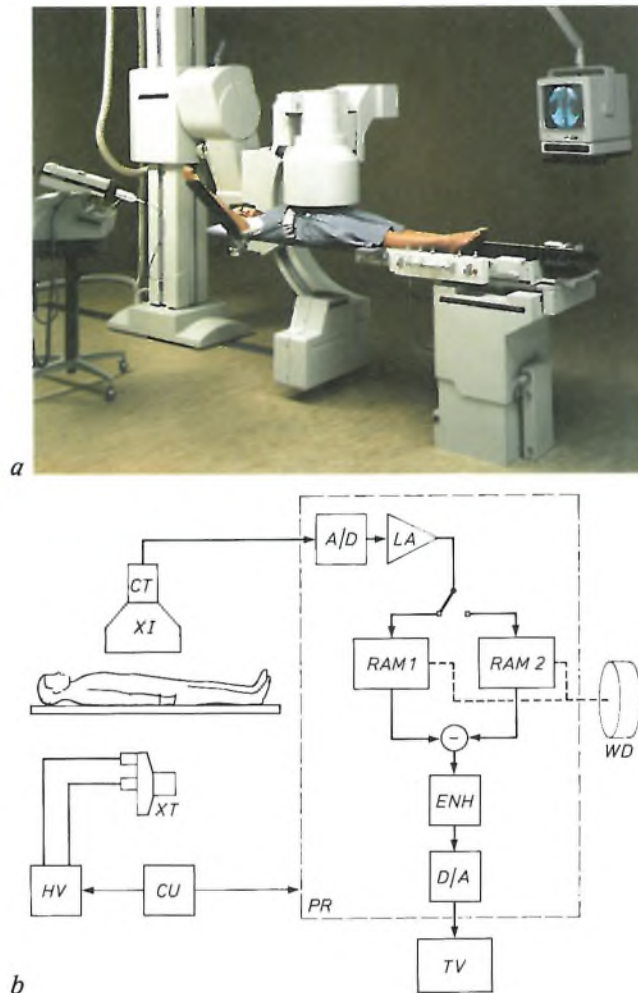


**Fig. 10.** *a)* Photograph of Philips X-ray diagnostic equipment with an image intensifier and a TV camera tube, with the addition of digital vascular imaging (DVI) equipment. *b)* Block diagram of a DVI system. *CT* camera tube. *XI* image intensifier. *PR* signal-processing equipment. *A/D* analog-to-digital converter. *LA* logarithmic amplifier. *RAM1* and *RAM2* semiconductor memories, each for one image; the contents of memory *RAM1* can be subtracted from the contents of *RAM2*. *ENH* digital signal enhancement. *D/A* digital-to-analog converter. *TV* display screen on operating console. *HV* high-voltage generator. *XT* rotating-anode X-ray tube. *CU* control electronics. *WD* Winchester disc.

been made with contrast medium, the image stored in *RAM1* is subtracted from the new image in *RAM2*. The static anatomical background is suppressed in the resultant subtraction. The radiologist can observe the successive results of subtractions on the TV monitor and can therefore estimate the flow of the contrast medium in the vascular system. All the images are stored on the Winchester disc, so that they can be reproduced later.

DVI has been of great value in the diagnosis of vascular disorders. However, when this technique is used, movement artefacts have to be taken into account. One kind of movement artefact, due to bowel gas, can lead to a false diagnosis of vascular stenosis. But when the dual-energy technique is used the radiologist can prevent such errors, by selecting a notional X-ray energy at which the contrast between gas and water is virtually zero (see fig. 4). The X-ray images with contrast medium and without must then each be derived from two images made at different energies spaced by about 0.1 s.

Another possibility worth looking at more closely is the use of DVI equipment in the same way as a CT scanner is used for computed radiography. This can be done because the closed-circuit television of the DVI system applies the same kind of digital information. The addition of the dual-energy technique then opens up new uses for DVI equipment, e.g. in the diagnosis of lesions in the abdomen, thorax and cranium. The calibration method described earlier cannot however be used. One reason for this is that scattered radiation is more of a problem with an X-ray image intensifier. This application of DVI therefore only gives qualitative information and not quantitative information for tissue analysis.

Finally, *fig. 11a* and *b* shows how the dual-energy technique can be used to reduce the contrast between

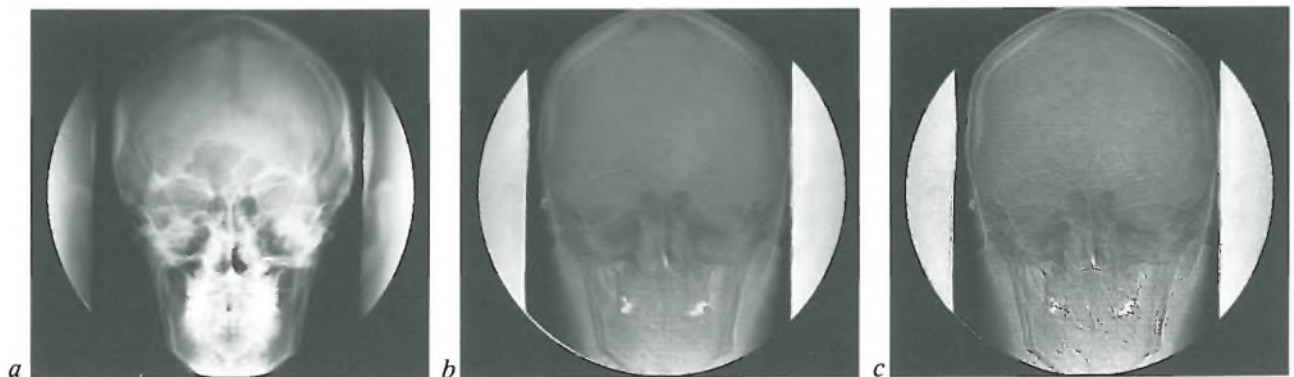


**Fig. 11.** *a)* Cranial image made with DVI equipment at a tube voltage of 70 kV. *b)* Weighted combination of exposures at 70 kV and 120 kV of the same cranium. The images show that by choosing the appropriate energy-dependent weighting factors the contrast between brain tissue and surrounding bone structures can be reduced to zero, so that the paranasal sinuses can be observed more clearly. *c)* The same exposure, but with edge enhancement. Details of the paranasal sinuses are now clearer still.

brain tissue and surrounding bone structures in a cranial exposure made with DVI equipment. As a result, details in the paranasal sinuses can be studied more closely, especially when the unsharp-masking technique is used at the same time (see fig. 11c).

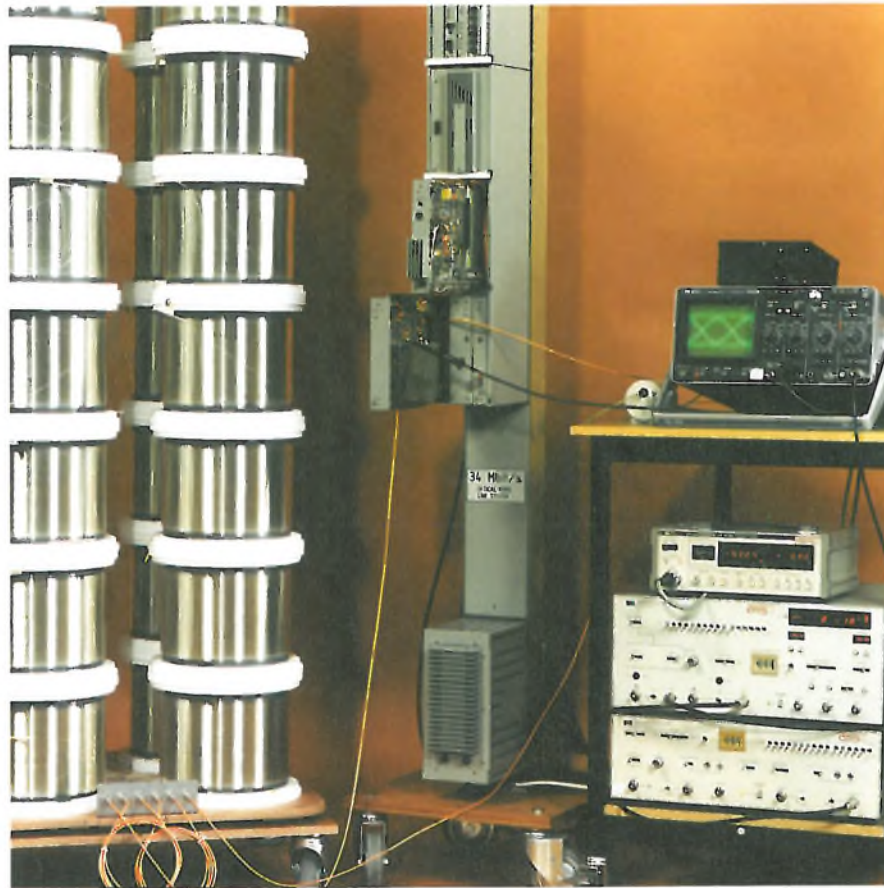
**Summary.** The X-ray attenuation coefficient of biological materials can be split into separate contributions due to Compton scattering and photoelectric absorption. The contributions are each the product of a known energy-dependent factor and an unknown material-dependent factor. If two X-ray exposures are made at different energies the material-dependent factors due to Compton scattering and to photoelectric absorption can be determined. This enables X-ray images entirely due to Compton scattering or to photoelectric absorption to be calculated. These images can be weighted by the energy-dependent factors and combined to give monoenergetic X-ray images. The contrasts between tissues can then be varied by

significant contributions to the investigation described in this article were made by J. M. Kosanetsky (Philips Forschungslaboratorium Hamburg) and F. W. Zonneveld (Medical Systems Division, Philips NPB, Best).

varying the notional X-ray energy. A calibration procedure is necessary because the polyenergetic X-radiation becomes harder in the object. This procedure provides calibration coefficients for the material-dependent factors. A Philips CT scanner has been modified to supply alternate high-voltage and low-voltage pulses to the X-ray tube. The electron density and the atomic number can be derived from the material-dependent factors for each pixel. The electron densities and the atomic numbers of tissues can be used for quantitative analysis. The dual-energy technique can also be used in conjunction with Philips DVI (Digital Vascular Imaging) equipment.

---

## Optical transmission in the 1.55- $\mu\text{m}$ window



The photograph shows test equipment for measurements on the propagation of optical signals in a single-mode optical fibre 123 km in length (the stacked coils on the left). This fibre, a product of the Philips Glass-Fibre Works in Eindhoven, has an extremely effective transmission window in the near infrared ( $\lambda = 1.55 \mu\text{m}$ ). This means that the attenuation of the signals may be no more than 0.25 dB per kilometre of cable, making optical communication possible over distances up to about 120 km without regeneration. The quality of the signal transmission can be assessed from an 'eye pattern', shown here on the oscilloscope screen (on the right). The eye pattern is formed by periodically displaying the pulses of the output signal one over the other. The 'eye' should be wide open, sharply outlined and should not oscillate (no 'winking'). In the case illustrated here the transmission quality is so good that the mean detection error in a signal consisting of a billion ( $10^9$ ) bits is only two bits. This bit error rate (BER) is measured with a data gen-

erator, the white panel at the lower right, and the error detector just above it (it is reading a measured value of  $2 \times 10^{-9}$ ). The small white panel is a digital power meter, for determining the detected power. The meter reading is  $-50.04$  dB with respect to a reference level of 1 mW; this reading corresponds to a detected power of 10 nW. The grey column at the centre contains the system modules with the laser transmitter (above) and the radiation detector (below), with the supporting electronics. In the laser transmitter there is a special diode laser, designed at Philips Research Laboratories. The transmission rate of this communication system, developed by AT&T and Philips Telecommunications<sup>[1]</sup>, is 34 million bits per second. The system is particularly attractive for island regions with many submarine cables, since there will often be no need for expensive repeaters.

<sup>[1]</sup> A. Wismeijer, Long distance single-mode fibre transmission, Philips Telecommun. Rev. 43, 43-49, 1985.

## Scientific publications

These publications are contributed by staff of laboratories and plants that form part of or cooperate with enterprises of the Philips group of companies, particularly by staff of the research laboratories mentioned below. The publications are listed alphabetically by journal title.

Philips GmbH Forschungslaboratorium Aachen, Weißhausstraße, 5100 Aachen, Germany	A
Philips Research Laboratory, Brussels, 2 avenue Van Becelaere, 1170 Brussels, Belgium	B
Philips Natuurkundig Laboratorium, Postbus 80 000, 5600 JA Eindhoven, The Netherlands	E
Philips GmbH Forschungslaboratorium Hamburg, Vogt-Kölln-Straße 30, 2000 Hamburg 54, Germany	H
Laboratoires d'Electronique et de Physique Appliquée, 3 avenue Descartes, 94450 Limeil-Brévannes, France	L
Philips Laboratories, N.A.P.C., 345 Scarborough Road, Briarcliff Manor, N.Y. 10510, U.S.A.	N
Philips Research Laboratories, Cross Oak Lane, Redhill, Surrey RH1 5HA, England	R
Philips Research Laboratories, Sunnyvale P.O. Box 9052, Sunnyvale, CA 94086, U.S.A.	S

O. Chantelou, M. le Quéau & I. Rak- hodai ( <i>La Radiotechnique, Suresnes</i> ) L	Réduction de la diaphotie en PAL et en SECAM	Acta Electron. 26	149-161	1984
D. W. Parker & L. J. van de Polder R, E	Display standards for extended definition component television systems	Acta Electron. 26	163-167	1984
S. L. Tan & R. N. Jackson E, R	Flexible coding and decoding for extended television	Acta Electron. 26	169-173	1984
J.-P. Arragon L	L'embrouillage du signal vidéo fréquence; application à la norme MAC	Acta Electron. 26	183-198	1984
M. le Quéau L	Méthodes numériques de démodulation de fréquence appliquées aux signaux de télévision	Acta Electron. 26	199-207	1984
M. Haghiri, J.-P. Kernin, J.-M. Kirichdjian, J.-J. Lhuillier & C. Rémus L	Réduction de débit d'images de télévision	Acta Electron. 26	209-239	1984
A. J. Fox R	Acoustooptic figure of merit for single crystal germanium at 10.6- $\mu$ m wavelength	Appl. Opt. 24	2040-2041	1985
P. H. Joosten, P. Heller, H. J. P. Nabben, H. A. M. van Hal, T. J. A. Popma & J. Haisma E	Optical thin layers of MgF <sub>2</sub> produced by decomposition of organic magnesium-fluoro compounds	Appl. Opt. 24	2674-2678	1985
J. Haisma, J. H. T. Pasma, J. M. M. Pasmans & P. van der Werf E	Wide-spectrum tint-free reflection reduction of viewing screens	Appl. Opt. 24	2679-2686	1985
J. Khurgin & W. K. Zwicker N	High efficiency nanosecond miniature solid-state laser	Appl. Opt. 24	3565-3569	1985
P. H. Woerlee, G. A. M. Hurkx, W. J. M. J. Josquin & J. F. C. M. Verhoeven E	Novel method of producing ultrasmall platinum silicide gate electrodes	Appl. Phys. Lett. 47	700-702	1985
K. H. Nicholas & R. A. Ford R	Ghost proximity correction in an electron image projector	Appl. Phys. Lett. 47	1227-1228	1985
J. Hasker & N. C. J. van Hijningen E	Cathode and scaling properties related to the shape of current-voltage characteristics	Appl. Surf. Sci. 24	318-329	1985
J. Hasker & H. J. H. Stoffelen E	'Alternative' Auger analysis reveals important properties of M-type and scandate cathodes	Appl. Surf. Sci. 24	330-339	1985
P. M. van Dooren & M. Verhaegen ( <i>Katholieke Univ. Leuven, Heverlee</i> ) B	On the use of unitary state-space transformations	Contemp. Math. 47	447-463	1985
P. Piret B	Word correction by means of convolutional codes	Discrete Math. 56	239-243	1985

- |   |      |   |  |           |      |
|---|------|---|--|-----------|------|
| N. D. Young & M. J. Hight   | R    | Automated Hall effect profiler for electrical characterisation of semiconductors  | Electron. Lett. 21   | 1044-1046 | 1985 |
| A. F. Dadds   | R    | Miranda — a mobile ESM laboratory   | IEE Proc. F 132  | 280-282   | 1985 |
| P. D. White, M. K. Gurcan & R. J. G. MacNamee   | R    | 900 MHz digital cordless telephone  | IEE Proc. F 132  | 425-432   | 1985 |
| C. A. Fisher, J. M. Shannon, D. H. Paxman & J. A. G. Slatter  | R    | The performance of high-voltage field relieved Schottky barrier diodes  | IEE Proc. I 132  | 257-260   | 1985 |
| J. B. H. Peek   | E    | Communications aspects of the Compact Disc digital audio system   | IEEE Commun. Mag. 23 (No. 2)   | 7-15      | 1985 |
| D. Lenstra ( <i>Delft Univ. Technol.</i> ), B. H. Verbeek & A. J. den Boef  | E    | Coherence collapse in single-mode semiconductor lasers due to optical feedback  | IEEE J. QE-21  | 674-679   | 1985 |
| P. I. Kuindersma, A. Valster & W. Baks  | E    | 1.3 $\mu\text{m}$ buried heterojunction laser diodes under high electrical stress: leakage currents and aging behavior          | IEEE J. QE-21  | 726-736   | 1985 |
| R. Cuppens, C. D. Hartgring, J. F. Verwey, H. L. Peek, F. A. H. Vollebregt, E. G. M. Devens & I. A. Sens  | E    | An EEPROM for microprocessors and custom logic  | IEEE J. SC-20  | 603-608   | 1985 |
| J. B. Hughes, N. C. Bird & R. S. Soin   | R    | A receiver IC for a 1 + 1 digital subscriber loop   | IEEE J. SC-20  | 671-678   | 1985 |
| F. P. J. M. Welten, A. Delaruelle, F. J. van Wijk, J. L. van Meerbergen, J. Schmid*, K. Rinner* (* <i>Tekade, Nürnberg</i> ), K. J. E. van Eerdewijk & J. H. Wittek ( <i>Valvo, Hamburg</i> ) | E    | A 2- $\mu\text{m}$ CMOS 10-MHz microprogrammable signal processing core with an on-chip multiport memory bank                   | IEEE J. SC-20  | 754-760   | 1985 |
| R. Woudsma & J. M. Noteboom   | E    | The modular design of clock-generator circuits in a CMOS building-block system  | IEEE J. SC-20  | 770-774   | 1985 |
| R. Eising ( <i>Signaal, Hengelo</i> )   |      | Polynomial matrices and feedback  | IEEE Trans. AC-30  | 1022-1025 | 1985 |
| P. Delsarte, Y. V. Genin & Y. G. Kamp   | B    | A generalization of the Levinson algorithm for Hermitian Toeplitz matrices with any rank profile                                | IEEE Trans. ASSP-33  | 964-971   | 1985 |
| M. Davio & C. Ronse   | B    | Insertion networks  | IEEE Trans. C-34   | 565-570   | 1985 |
| V. Belevitch  | B    | Discrete frequency passivity conditions for $n$ -ports  | IEEE Trans. CAS-32   | 404-405   | 1985 |
| B. Dickinson ( <i>Princeton Univ.</i> ), P. Delsarte, Y. Genin & Y. Kamp  | B    | Minimal realizations of pseudo-positive and pseudo-bounded rational matrices  | IEEE Trans. CAS-32   | 603-605   | 1985 |
| A. G. Tangena & G. A. M. Hurkx  | E    | Calculations of mechanical stresses in electrical contact situations  | IEEE Trans. CHMT-8   | 13-20     | 1985 |
| P. A. Gough & J. A. Slatter   | R    | A model for the GTO thyristor during switch-off   | IEEE Trans. ED-31  | 1796-1803 | 1984 |
| S. Makram-Ebeid & P. Minondo  | E, L | The roles of the surface and bulk of the semi-insulating substrate in low-frequency anomalies of GaAs integrated circuits       | IEEE Trans. ED-32  | 632-642   | 1985 |
| P. Piret  | B    | Binary codes for compound channels  | IEEE Trans. IT-31  | 436-440   | 1985 |
| C. Tsironis   | L    | Highly stable dielectric resonator FET oscillators  | IEEE Trans. MTT-33   | 310-314   | 1985 |
| F. A. Staas   | E    | On-line data reduction of the Doppler-difference autocorrelation function   | Int. Proc. Conf. on Laser anemometry — advances and application, Manchester 1985 | 343-350   | 1985 |
| J. E. Knowles   | R    | Magnetic properties of individual acicular particles  | Introduction to magnetic recording, R. M. White (ed.), IEEE Press, New York      | 83-88     | 1985 |
| P. F. Fewster   | R    | Alignment of double-crystal diffractometers   | J. Appl. Crystallogr. 18   | 334-338   | 1985 |
| C. Schiller   | L    | Precise orientation of semiconductor surfaces by the back-reflection Laue technique   | J. Appl. Crystallogr. 18   | 373       | 1985 |
| P. A. Breddels & H. A. van Sprang   | E    | An analytical expression for the optical threshold in highly twisted nematic systems with nonzero tilt angles at the boundaries | J. Appl. Phys. 58  | 2162-2166 | 1985 |



- |  |   |  |                              |               |      |
|--|---|--|------------------------------|---------------|------|
| P. Blood   | R | Measurement of optical absorption in epitaxial semiconductor layers by a photovoltage method   | J. Appl. Phys. 58            | 2288-2295     | 1985 |
| S. Hasegawa (Kanazawa Univ., Kanazawa) & P. C. Zalm  | E | Formation and bonding structure of silicon nitride by 20-keV N <sup>+</sup> ion implantation   | J. Appl. Phys. 58            | 2539-2543     | 1985 |
| A. A. van Gorkum & M. H. L. M. van den Broek   | E | Spot reduction in electron guns using a selective pre-focusing lens  | J. Appl. Phys. 58            | 2902-2908     | 1985 |
| P. M. J. Marée*, R. I. J. Olthof*, J. W. M. Frenken*, J. F. van der Veen* (* FOM, Amsterdam), C. W. T. Bulle-Lieuwma, M. P. A. Vieggers & P. C. Zalm | E | Silicon strained layers grown on GaP(001) by molecular beam epitaxy  | J. Appl. Phys. 58            | 3097-3103     | 1985 |
| J. W. D. Martens & W. F. Godlieb   | E | Magneto-optical properties of 100-keV Ne <sup>+</sup> -implanted epitaxial Y <sub>3</sub> Fe <sub>5</sub> O <sub>12</sub> thin films               | J. Appl. Phys. 58            | 3180-3184     | 1985 |
| A. H. van Ommen & R. A. M. Wolters   | E | Influence of P and As implantation on the formation of MoSi <sub>2</sub>   | J. Appl. Phys. 58            | 4043-4048     | 1985 |
| J. Petruzello, T. F. McGee, M. H. Frommer, V. Rumennik, P. A. Walters & C. J. Chou   | N | Transmission electron microscopy and Auger electron spectroscopy of silicon-on-insulator structures prepared by high-dose implantation of nitrogen | J. Appl. Phys. 58            | 4605-4613     | 1985 |
| K. A. Schouhamer Immink & J. J. M. Braat   | E | Experiments toward an erasable Compact Disc digital audio system   | J. Audio Eng. Soc. 32        | 531-538       | 1984 |
| J. C. Tranchart, B. Latorre, C. Foucher & Y. le Gouge  | L | LPE growth of Hg <sub>1-x</sub> Cd <sub>x</sub> Te on Cd <sub>1-y</sub> Zn <sub>y</sub> Te substrates  | J. Cryst. Growth 72          | 468-473       | 1985 |
| S. Colak, B. J. Fitzpatrick & R. N. Bhargava   | N | Electron beam pumped II-VI lasers  | J. Cryst. Growth 72          | 504-511       | 1985 |
| P. F. Bordui, S. P. Herko & G. Kosticky  | N | Computer-controlled crystal growth of KDP from aqueous solution  | J. Cryst. Growth 72          | 756-758       | 1985 |
| M. W. M. Graef, B. J. H. Leunissen & H. H. C. de Moor (Univ. Nijmegen)   | E | Antimony, arsenic, phosphorus, and boron auto-doping in silicon epitaxy  | J. Electrochem. Soc. 132     | 1942-1954     | 1985 |
| P. Schobinger-Papamantellos (ETH, Zürich) & K. H. J. Buschow   | E | Incommensurate magnetic structure of ErGe studied by neutron diffraction and magnetic measurements   | J. Less-Common Met. 111      | 117-124       | 1985 |
| P. Schobinger-Papamantellos (ETH, Zürich) & K. H. J. Buschow   | E | Ferromagnetism of NdGe and PrGe studied by neutron diffraction and magnetic measurements   | J. Less-Common Met. 111      | 125-138       | 1985 |
| H. M. van Noort & K. H. J. Buschow   | E | On the site preference of 3d atoms in compounds of the R <sub>2</sub> (Co <sub>1-x</sub> Fe <sub>x</sub> ) <sub>14</sub> B type                    | J. Less-Common Met. 113      | L9-L12        | 1985 |
| J. P. Woerdman*, J. Schlejen*, J. Korving*, M. C. van Hemert* (* Univ. Leiden), J. J. de Groot (Philips Lighting Div., Eindhoven) & R. P. M. van Hal | E | Analysis of satellite and undulation structure in the spectrum of Na + Hg continuum emission   | J. Phys. B 18                | 4205-4221     | 1985 |
| H. Zijlstra  | E | Application of permanent magnets in electromechanical power converters; the impact of Nd-Fe-B magnets  | J. Physique 46 (Colloque C6) | C6/3-C6/8     | 1985 |
| S. Sinnema*, J. J. M. Franse* (* Univ. Amsterdam), R. J. Radwanski (Acad. Mining & Metallurgy, Cracow), K. H. J. Buschow & D. B. de Mooij            | E | Magnetic measurements on R <sub>2</sub> Fe <sub>14</sub> B and R <sub>2</sub> Co <sub>14</sub> B compounds in high fields                          | J. Physique 46 (Colloque C6) | C6/301-C6/304 | 1985 |
| M. Brouha, G. W. Turk & A. J. C. van der Borst   | E | Soft magnetic properties of CoFeBSi amorphous ribbon improved by pulse annealing   | J. Physique 46 (Colloque C6) | C6/413-C6/416 | 1985 |
| A. G. Dirks & J. J. van den Broek  | E | Metastable solid solutions in vapor deposited Cu-Cr, Cu-Mo, and Cu-W thin films  | J. Vac. Sci. & Technol. A 3  | 2618-2622     | 1985 |
| G. Duggan  | R | A critical review of heterojunction band offsets   | J. Vac. Sci. & Technol. B 3  | 1224-1230     | 1985 |
| J. Dieleman, F. H. M. Sanders, A. W. Kofschoten, P. C. Zalm, A. E. de Vries* & A. Haring* (* FOM, Amsterdam)   | E | Studies on the mechanism of chemical sputtering of silicon by simultaneous exposure to Cl <sub>2</sub> and low-energy Ar <sup>+</sup> ions         | J. Vac. Sci. & Technol. B 3  | 1384-1392     | 1985 |
| G. W. 't Hooft, M. R. Leys & F. Roozeboom  | E | Low interface recombination velocity in GaAs-(Al,Ga)As double heterostructures grown by metal organic vapour phase epitaxy                         | Jap. J. Appl. Phys. 24       | L761-L763     | 1985 |

A. E. T. Kuiper, F. H. P. M. Habraken ( <i>Univ. Utrecht</i> ) & J. T. Chen <i>E, S</i>	Hydrogenation during thermal nitridation of SiO <sub>2</sub>	Mater. Res. Soc. Symp. Proc. 48	387-394	1985
F. H. P. M. Habraken ( <i>Univ. Utrecht</i> ) & A. E. T. Kuiper <i>E</i>	Growth and composition of LPCVD silicon oxynitride films	Mater. Res. Soc. Symp. Proc. 48	395-401	1985
J. Robertson ( <i>Central Electric. Res. Labs, Leatherhead</i> ) & M. J. Powell <i>R</i>	Defect states in silicon nitride	Mater. Res. Soc. Symp. Proc. 49	215-222	1985
M. H. L. M. van den Broek <i>E</i>	Simulation of 3D electron beams with a fitting technique	Optik 71	27-30	1985
A. A. van Gorkum <i>E</i>	The cup model for the cathode lens in triode electron guns	Optik 71	93-104	1985
C. Ronse <i>B</i>	A simple proof of Rosenfeld's characterization of digital straight line segments	Pattern Recognition Lett. 3	323-326	1985
H. Zijlstra <i>E</i>	Permanent magnet systems for NMR tomography	Philips J. Res. 40	259-288	1985
G. F. M. Beenker, T. A. C. M. Claassen & P. W. C. Hermens <i>E</i>	Binary sequences with a maximally flat amplitude spectrum Erratum	Philips J. Res. 40 Philips J. Res. 40	289-304 399	1985 1985
K. H. J. Buschow <i>E</i>	Rare earth based Invar alloys	Philips J. Res. 40	305-312	1985
K. H. J. Buschow, D. B. de Mooij, T. T. M. Palstra*, G. J. Nieuwenhuys* & J. A. Mydosh* ( <i>* Univ. Leiden</i> ) <i>E</i>	Crystal structure and magnetic properties of several equiatomic ternary U compounds	Philips J. Res. 40	313-322	1985
F. C. van den Heuvel & Q. H. F. Vrehan <i>E</i>	Striations of the convective type and feedback in low-pressure mercury/noble-gas discharges	Phys. Fluids 28	3034-3039	1985
R. Houdré*, C. Hermann*, G. Lampel* ( <i>* Ecole Polytech., Palaiseau</i> ), P. M. Frijlink & A. C. Gossard ( <i>AT&amp;T Bell Labs, Murray Hill, NJ</i> ) <i>L</i>	Photoemission from a superlattice and a single quantum well	Phys. Rev. Lett. 55	734-737	1985
J. M. Woodcock, J. J. Harris & J. M. Shannon <i>R</i>	Monolithic hot electron transistors in GaAs with high current gain	Physica 134B	111-115	1985
R. Woltjer, J. Mooren, J. Wolter ( <i>Eindhoven Univ. Technol.</i> ), J.-P. André & G. Weimann ( <i>Forschungsinst. Deutschen Bundespost, Darmstadt</i> ) <i>E, L</i>	Four-terminal quantum Hall and Shubnikov-De Haas measurements with pulsed electron fields	Physica 134B	352-356	1985
T. Krol & W. J. van Gils <i>E</i>	The input/output architecture of the (4,2) concept fault-tolerant computer	Proc. Ann. Int. Symp. on Fault-tolerant computing (FTCS 15), Ann Arbor, MI, 1985	254-259	1985
R. S. Soin, J. B. Hughes & N. C. Bird <i>R</i>	A novel approach to the time domain simulation of switched capacitor systems	Proc. Eur. Conf. on Circuit theory and design, Prague 1985	713-716	1985
M. Rocchi <i>L</i>	N-Off GaAs digital MESFET IC's	Proc. GaAs IC Seminar, London 1985	7 pp.	1985
P. Dautriche, B. Y. Lao ( <i>Magnavox, Torrance, CA</i> ), C. Villalon, V. Pauker, M. Bostelmann & M. Binet <i>L</i>	GaAs monolithic circuits for TV tuners	Proc. GaAs IC Symp., Monterey, CA, 1985	166-168	1985
L. J. van de Polder, D. W. Parker & J. Roos <i>E, R</i>	Evolution of television receivers from analog to digital	Proc. IEEE 73	599-612	1985
P. K. Bachmann, D. Leers, H. Wehr, F. Weirich, D. Wiechert, J. A. van Steenwijk, D. L. A. Tjaden & E. Wehrhahn ( <i>Philips Kommun. Ind., Nürnberg</i> ) <i>A, E</i>	PCVD DFSM-fibres: performance, limitations, design optimization	Proc. IOOC-ECOC, Venezia 1985	197-200	1985
P. J. Severin & A. P. Severijns <i>E</i>	Passive components for multimode fibre-optic networks	Proc. IOOC-ECOC, Venezia 1985	453-456	1985
G. D. Khoe & A. H. Dieleman <i>E</i>	TTOSS, a subscriber network for direct detection and coherent systems	Proc. IOOC-ECOC, Venezia 1985	479-482	1985
C. M. G. Jochem & J. W. C. van der Light <i>E</i>	High-speed bubble-free coating of optical fibres on a short drawing tower	Proc. IOOC-ECOC, Venezia 1985	515-518	1985

- |  |   |   |   |           |      |
|--|---|---|---|-----------|------|
| D. J. Broer & G. N. Mol  | E | Fast curing, low-modulus coatings for high strength optical fibres  | Proc. IOOC-ECOC, Venezia 1985   | 523-526   | 1985 |
| J. P. André, J. P. Chané, J. L. Gentner, C. Mallet-Mouko, B. G. Martin, G. M. Martin, E. Menu & J. N. Patillon   | L | Low dark current and low capacitance InGaAs PIN photodiode grown by MOVPE   | Proc. IOOC-ECOC, Venezia 1985   | 541-544   | 1985 |
| G. D. Khoe & A. Valster  | E | Coupling of laser diodes and side emitting LEDs to flat dispersion quadruple clad monomode fibres at 1300 and 1530 nm   | Proc. IOOC-ECOC, Venezia 1985   | 641-644   | 1985 |
| C. A. M. de Vries & H. T. Arends   | E | The influence of argon in fluorocarbon RF discharges for dry etching  | Proc. ISPC-7, Eindhoven 1985  | 1019-1024 | 1985 |
| H. Baumgart & F. Phillipp ( <i>Max Planck Inst., Stuttgart</i> )   | N | Low angle grain boundaries in zone-melting grown silicon films  | Proc. Microscopy of Semiconductor Materials Conf., Oxford 1985                      | 89-92     | 1985 |
| M. Lemonier, J. C. Richard, C. Cavailler*, A. Mens* & G. Raze* ( <i>* Centre d'Etudes de Limeil-Valenton, Villeneuve-Saint-Georges</i> )                       | L | Lecture d'images de caméras á balayage de fente picosecondes par D.T.C.   | Proc. SPIE 491  | 706-712   | 1985 |
| B. L. Michielsen   | E | A new approach to electromagnetic shielding   | Proc. Symp. & Tech. Exhibit. on Electromagnetic compatibility, Zürich 1985          | 509-514   | 1985 |
| F. M. Klaassen   | E | Compact MOSFET modelling  | Process & device modeling, W. L. Engl (ed.), Elsevier Science, Amsterdam            | 393-412   | 1986 |
| H. C. de Graaff  | E | Compact bipolar transistor modelling  | Process & device modeling, W. L. Engl (ed.), Elsevier Science, Amsterdam            | 431-432   | 1986 |
| P. M. L. O. Scholte*, M. Tegze*, F. van der Woude* ( <i>* Univ. Groningen</i> ), K. H. J. Buschow & I. Vincze* ( <i>* Central Res. Inst. Phys., Budapest</i> ) | E | Mössbauer spectroscopy on amorphous $Fe_xZr_{100-x}$ ( $20 < x < 90$ ) alloys   | Rapidly quenched metals, S. Steeb & H. Warlimont (eds), Elsevier Science, Amsterdam | 541-544   | 1985 |
| G. Duggan, H. I. Ralph & R. J. Elliot ( <i>Dept Theor. Phys., Oxford</i> )   | R | Interface recombination in p-type GaAs-(AlGa)As quantum well heterostructures   | Solid State Commun. 56  | 17-20     | 1985 |
| F. Berz  | R | The Bethe condition for thermionic emission near an absorbing boundary  | Solid-State Electron. 28  | 1007-1013 | 1985 |
| P. W. J. M. Boumans & J. J. A. M. Vrakking   | E | Spectral interferences in inductively coupled plasma atomic emission spectrometry — I. A theoretical and experimental study of the effect of spectral bandwidth on selectivity, limits of determination, limits of detection and detection power              | Spectrochim. Acta 40B   | 1085-1105 | 1985 |
| P. W. J. M. Boumans & J. J. A. M. Vrakking   | E | Spectral interferences in inductively coupled plasma atomic emission spectrometry — II. An experimental study of the effect of spectral bandwidth on the inaccuracy in net signals originating from wavelength positioning errors in a slew-scan spectrometer | Spectrochim. Acta 40B   | 1107-1125 | 1985 |
| P. W. J. M. Boumans & J. J. A. M. Vrakking   | E | Spectral interferences in inductively coupled plasma atomic emission spectrometry — III. An assessment of OH band interferences using the ratio of the limit of determination and the limit of detection as a rational criterion                              | Spectrochim. Acta 40B   | 1423-1435 | 1985 |
| P. W. J. M. Boumans & J. J. A. M. Vrakking   | E | Detection limits in inductively coupled plasma atomic emission spectrometry: an approach to the breakdown of the ratios of detection limits reported for different equipments   | Spectrochim. Acta 40B   | 1437-1446 | 1985 |
| P. N. T. van Velzen & M. C. Raas   | E | An IETS study of the silylation of plasma aluminium oxide with four trimethylsilylamines and hexamethyldisiloxane   | Surf. Sci. 161  | L605-L613 | 1985 |

J. J. Harris	R	III-V microwave devices	The technology and physics of molecular beam epitaxy, E. H. C. Parker (ed.), Plenum, New York	425-465	1985
A. J. M. Kaizer	E	On the design of broadband electro-dynamical loudspeakers and multiway loudspeaker systems	Thesis, Eindhoven	84 pp.	1986
H. J. G. Draaisma ( <i>Eindhoven Univ. Technol.</i> ), H. M. van Noort & F. J. A. den Broeder	E	Magnetic, microstructural and Mössbauer studies of Cu/Fe composition-modulated thin films	Thin Solid Films 126	117-121	1985
J. W. Smits & F. J. A. den Broeder	E	Magnetic and structural properties of ion-beam-sputtered thin films of $(\text{Co}_{90}\text{Cr}_{10})_{100-x}\text{TM}_x$ where TM denotes vanadium, niobium, molybdenum or tantalum	Thin Solid Films 127	1-8	1985
W. A. P. Claassen ( <i>Philips Elcoma Div., Nijmegen</i> ), W. G. J. N. Valkenburg, W. M. van de Wijgert & M. F. C. Willemsen	E	On the relation between deposition conditions and (mechanical) stress in plasma silicon nitride layers	Thin Solid Films 129	239-247	1985
J. J. van den Broek, A. G. Dirks & P. E. Wierenga	E, S	The composition dependence of internal stress, ultramicrohardness and electrical resistivity of binary alloy films containing silver, aluminium, gold, cobalt, copper, iron or nickel	Thin Solid Films 130	95-101	1985
B. A. J. Jacobs	E	Thin film requirements for optical recording	Vacuum 35	445-446	1985
E. D. Roberts	R	Resists used in plasma processing	Vacuum 35	479-483	1985
G. F. Weston	R	Pumping systems	Vacuum 35	493-497	1985
J. E. Curran & D. J. McCulloch	R	Reactive ion etching of GaAs and related materials for electro-optic and other devices	Vacuum 35	504-506	1985

*Contents of Electronic Components & Applications 7, No. 2, 1986*

- R. Volgers: Astable multivibrators using HCMOS ICs (pp. 66-72)
- J. Exalto: Crystal oscillators using HCMOS ICs (pp. 73-76)
- Automatic placement machine for hybrid-circuit assembly (pp. 77-80)
- M. Collet: MOS-XY, interline and frame-transfer sensors compared (pp. 81-88)
- J. Magill: Controller IC contends with multiple protocols (pp. 89-94)
- A. Jonas & D. Onck: Alloy bonding for power semiconductors (pp. 95-105)
- S. Baliga: VMEbus interface ICs for simpler asynchronous systems (pp. 106-111)
- C. Hamelin: Manually testing the a.c. characteristics of ECL ICs (pp. 112-115)
- A. Dolstra: Indoor unit for satellite-ready tv (pp. 116-118)

*Contents of Electronic Components & Applications 7, No. 3*

- H. Molko: HCMOS low-power ICs that set the standard (pp. 130-143)
- J. Exalto: HCMOS Schmitt-trigger applications (pp. 144-150)
- R. Volgers: Using 74HCT HCMOS to replace LSTTL and drive transmission lines (pp. 151-162)
- J. Exalto & H. Kloen: Protection of HCMOS logic ICs in the automotive environment (pp. 163-169)
- H. Kloen: Modifying LSTTL test programs to test HCMOS logic ICs (pp. 170-178)
- R. Croes: Battery backup of HCMOS logic ICs (pp. 179-186)
- R. Croes & P. Hendriks: Standardizing latch-up immunity tests for HCMOS logic ICs (pp. 187-197)



A. J. A. Nicia: An optical communication system with wavelength-division multiplexing and minimized insertion losses, I. System and coupling efficiency,  
Philips Tech. Rev. 42, No. 8/9, 245-261, June 1986.

A study of an optical communication system for digital or analog signals is described. Wavelength-division multiplexing is used with minimized insertion losses. The design provides for three to four channels in parallel operation in a multimode optical fibre (with a square-law core, radius 25  $\mu\text{m}$ , numerical aperture 0.2,  $\text{MHz} \times \text{km}$  product about 2000) in a second-generation cable for optical telecommunication. The light sources are diode lasers operating at wavelengths of 0.83  $\mu\text{m}$ , 0.87  $\mu\text{m}$ , 1.30  $\mu\text{m}$  and 1.55  $\mu\text{m}$ . The detectors are photodiodes of about 300  $\mu\text{m}$  diameter and a maximum rate of response of 500 MHz. The multiplexing and demultiplexing components are the main subject of part II of the article. Part I deals with the maximization of the total system efficiency. There are four interface zones, with about 6 dB total insertion loss. The first interface (laser to fibre via a ball lens) is analysed using Hermitian-Gaussian modal field distributions. The astigmatism and ellipticity of the lasers, and the cut-off of the higher-order modes (because of the finite radius of the fibre core) are accounted for in the optimized efficiency equations. The optimum strength and the location of the ball lens (between laser and fibre) are derived for a semi-collimator geometry. The behaviour of two-dimensional Gaussian beams in free space and inside the core is also calculated.

C. J. Nonhof and G. J. A. M. Notenboom: Beam manipulation with optical fibres in laser welding,  
Philips Tech. Rev. 42, No. 8/9, 262-264, June 1986.

For welding metal components together in large numbers growing use has been made in recent years of laser spot-welding instead of resistance spot-welding. The most important advantages of laser spot-welding are that there is no distortion, less maintenance of the equipment is necessary and the quality of the weld is better. The capital investment required for each laser is considerable, however. At the Centre for Manufacturing Technology in Eindhoven a method for beam manipulation has therefore been developed in which individual welds at different places can be made with a single laser. This is done by splitting the beam and focusing it on a number of optical fibres (e.g. 5). At the end of each fibre there is a lens that focuses the emitted laser beam on to the workpiece. The flexibility of the fibres provides an arrangement that can easily be adapted to products of a different shape. At present more than 200 laser spot-welders are in use at Philips. About 10 of these welders make use of the method described for beam manipulation with optical fibres.

W. G. Gelling and F. Valster: The new centre for submicron IC technology,  
Philips Tech. Rev. 42, No. 8/9, 266-273, June 1986.

The pilot production of 256-kbit static RAMs will start in about a year at the new centre for submicron technology. Use will be made of CMOS technology and photolithography with wafer steppers. In certain parts of the technology building the dust content of the air will be extremely low and the floors will be extremely insensitive to vibration. The low dust content will be achieved by using separate air-circulation systems for each 'process tunnel' with filters that trap 99.99995% of particles down to a diameter of 0.1  $\mu\text{m}$ . The vibration insensitivity of the floors that support the wafer steppers will be obtained by using a concrete box construction with high vertical and horizontal stiffness.

J. J. H. Coumans: Dual-energy X-ray diagnostics,  
Philips Tech. Rev. 42, No. 8/9, 274-285, June 1986.

The X-ray attenuation coefficient of biological materials can be split into separate contributions due to Compton scattering and photoelectric absorption. The contributions are each the product of a known energy-dependent factor and an unknown material-dependent factor. If two X-ray exposures are made at different energies the material-dependent factors due to Compton scattering and to photoelectric absorption can be determined. This enables X-ray images entirely due to Compton scattering or to photoelectric absorption to be calculated. These images can be weighted by the energy-dependent factors and combined to give monoenergetic X-ray images. The contrasts between tissues can then be varied by varying the notional X-ray energy. A calibration procedure is necessary because the polyenergetic X-radiation becomes harder in the object. This procedure provides calibration coefficients for the material-dependent factors. A Philips CT scanner has been modified to supply alternate high-voltage and low-voltage pulses to the X-ray tube. The electron density and the atomic number can be derived from the material-dependent factors for each pixel; these values can be used for quantitative tissue analysis. The dual-energy technique can also be used in conjunction with Philips DVI (Digital Vascular Imaging) equipment.





## O T H E R P H I L I P S P U B L I C A T I O N S

### **Philips Journal of Research**

A publication in English on the research work carried out in the various Philips laboratories. Published in annual volumes of six issues each of about 100 pages, size 15½ × 23½ cm.

### **Philips Telecommunication Review**

A publication in English, dealing with the technical aspects of radio, television, radar, telephone and telegraph transmission and automatic exchanges. Published in volumes of four issues, about 40 pages per issue, size 20½ × 28½ cm.

### **Electronic Components and Applications**

A publication in English, containing articles dealing with the theory and practice of electronic components and materials. Four issues per year, about 60 pages per issue, size 21 × 29½ cm.

### **Medicamundi**

A publication in English on radiology, nuclear medicine and medical electronics. Three issues per volume, about 60 pages per issue, size 21 × 29½ cm.

---

Forthcoming issues of Philips Technical Review will include articles on:

Silicon cold cathodes

Laser diagnostics for low-pressure mercury discharges

Applications of light guides in process control

PHILAN: Philips Integrated Local Area Network

The accordion imager

Dielectric resonators for microwave oscillators

---

## Contents

	Page
An optical communication system with wavelength-division multiplexing and minimized insertion losses, I. System and coupling efficiency . . . . .	A. J. A. Nicia 245
Beam manipulation with optical fibres in laser welding . . . . .	C. J. Nonhof and G. J. A. M. Notenboom 262
50 years ago . . . . .	265
The new centre for submicron IC technology . . . . .	W. G. Gelling and F. Valster 266
Dual-energy X-ray diagnostics . . . . .	J. J. H. Coumans 274
Optical transmission in the 1.55- $\mu$ m window . . . . .	286
Scientific publications . . . . .	287

---

PHILIPS TECHNICAL REVIEW  
Philips Research Laboratories  
P.O. Box 80 000  
5600 JA Eindhoven  
The Netherlands

Subscription rate per volume fl. 80.00 or U.S. \$ 35.00  
Student's subscription fl. 32.00 or U.S. \$ 14.00  
Binder fl. 10.00 or U.S. \$ 4.00

Payment only after invoicing, please.

Printed in the Netherlands



**PHILIPS**